# SYNERGISTIC AND ACCELERATED TESTING EFFECTS ON SPACE THERMAL-CONTROL MATERIALS

By

JAY D. PINSON

Bachelor of Science
Mechanical Engineering
Ohio University
Athens, Ohio
1950

Master of Science
Mechanical Engineering
Oklahoma State University
Stillwater, Oklahoma
1965

Submitted to the faculty of the Graduate College of
the Oklahoma State University
in partial fulfillment of the requirements
for the degree of
DOCTOR OF PHILOSOPHY
May, 1966

SYNERGISTIC AND ACCELERATED TESTING EFFECTS ON

SPACE THERMAL-CONTROL MATERIALS

Thesis Approved:

J. A. Wiebelt

Thesis Adviser

Glen W. Zumwalt

Allen M. Rowen

Ladislaus J Fila

Herbert Scholz

J. K. Boggs

Dean of the Graduate College

## ACKNOWLEDGMENTS

The author wishes to extend his sincere appreciation and gratitude to the following individuals and organizations:

Dr. J. A. Wiebelt, who served as committee chairman and thesis adviser, for his encouragement, assistance and guidance throughout the study.

Dr. G. W. Zumwalt, Professor L. J. Fila, Dr. A. M. Rowe, and Professor H. Scholz, who served as committee members, for their guidance and counsel.

Arnold Engineering Development Center, USAF, for financial support of the research program.

AVCO/Tulsa for use of their equipment in conducting the major portion of the experiments.

Mr. Paul Miller for his day-to-day encouragement and friendship.

Mrs. Betty Stewart for valuable assistance in preparation of the manuscript.

My wife, Ellie and children, Deborah, Barbara and Jay II for their sacrifice during the years of graduate study.

TABLE OF CONTENTS

LIST OF TABLES

## LIST OF FIGURES

# CHAPTER I

## INTRODUCTION

Space age technology and its applications have brought to light many new problems in the selection of materials for systems which are designed for operation in the complex space environment. Requirements associated with advancements in the space effort have resulted in the development of surface materials which, when exposed to the harsh environment of space, have desirable thermal-control properties and some degree of resistance to degradation. These coatings are required to survive and function efficiently for periods of long exposure to conditions involving high vacuum, intense ultraviolet radiation, penetrating radiation, micrometeorites and variable extreme temperatures.

The purpose of this study was to investigate experimentally the effects of various types of radiation on thermal-control materials and to obtain a better understanding of the environmental synergistic effects. Materials with a specified ratio of $\alpha_s$ (solar absorptance) to $\varepsilon$ (infrared emittance) were tested at various temperatures under a simulated environment of particle radiation, ultraviolet radiation, and low density. Synergistic and accelerated effects produced on the materials during the testing were investigated. Analysis of the experimental program resulted in conclusions regarding the degree and characteristics of simulation required for more realistic testing of thermal-control materials.

Tests on thermal-control materials, until recently, have been conducted under a low-density and ultraviolet radiation environment at room temperature. Although the existence of particle radiation (electrons, protons, etc.) is generally acknowledged to exist in space, this parameter was ignored in the material testing phase. For close earth-orbital and limited vehicle missions, the ultraviolet radiation of the solar spectrum can be assumed to be the primary cause of thermal-control material degradation. If mission trajectories include higher earth orbital conditions or interplanetary flights for prolonged periods, then other parameters such as particle radiation, will induce material degradation.

## CHAPTER II

## SPACE VEHICLE THERMAL-CONTROL SYSTEM

The purpose of this chapter is to describe the phenomena of thermal energy exchange of a space vehicle with its environment in order to establish the importance of the optical properties as related to the thermal-control materials. A detailed theoretical analysis on the subject is not intended.

A thermal-control system at the vehicle's surface is necessary for maintaining the temperature of the vehicle subsystems within their operational limits. The thermal-control system must remain stable and operate unattended in the space environment for long periods of exposure. The low-density environment affords only the heat transfer mechanism of radiation (no convection) to exchange thermal energy between the vehicle and its surroundings. For this reason, the temperatures of the subsystems are mainly controlled by the over-all ability of the thermal-control surfaces to emit, absorb, reflect, and/or transmit thermal energy.

The environmental parameters of space of greatest interest to the designer of a thermal-control system are solar radiation, planet radiation and planet reflected radiation (albedo radiation). The heat sink of space performs thermally as a blackbody at an effective temperature only a few degrees above absolute zero (approximately $4^{\circ}$ K). Thus,

the radiation to the vehicle from this background can be neglected. The thermal energy exchange of a vehicle and a space environment is shown in Figure 1. Discussion of the space environment is presented in Chapter III.

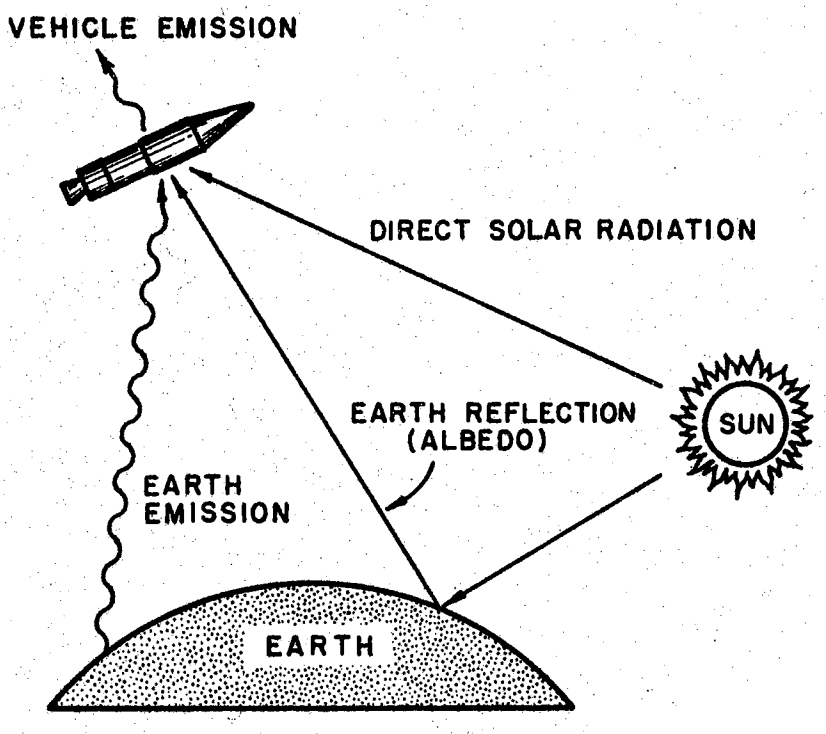


Figure 1. The Thermal Energy Exchange Between a Vehicle and the Space Environment

The heat balance equation for the thermal energy exchange is

$$\sigma\epsilon T^4 = \alpha_s F_s Q_s + \alpha_a F_a Q_a + \alpha_p F_p Q_p + Q_v \qquad (2\text{-}1)$$

$\sigma$ = Stefar-Boltzmann constant.

$\epsilon$ = Infrared emittance; the ratio of the energy emitted by the vehicle's outer surface to that which would be emitted by an ideal blackbody at the same temperature.

$T$ = Absolute temperature of the vehicle.

$\alpha_s$ = Solar absorptance; the fraction of incident solar energy absorbed by the vehicle surface.

$F_s$ = Vehicle configuration factor for direct solar radiation.

$Q_s$ = Solar radiation constant.

$\alpha_a$ = Albedo absorptance.

$F_a$ = Vehicle configuration factor for albedo radiation.

$Q_a$ = Planet albedo radiation constant.

$\alpha_p$ = Planet absorptance.

$F_p$ = Vehicle configuration factor for planet radiation.

$Q_p$ = Planet radiation constant.

$Q_v$ = Vehicle internal energy dissipation.

If one assumes that the spectrum of the albedo (solar radiation reflected from the planet) is approximately that of the sun and the absorptance of the vehicle surface coating for planetary emission is approximately equal to the infrared emittance of the vehicle's surface coating (1)[1], then the heat balance is represented as

$$\sigma \epsilon T^4 = \alpha_s F_s Q_s + \alpha_s F_a Q_a + \epsilon F_p Q_p + Q_v . \qquad (2\text{-}2)$$

---

[1]Numbers in parentheses indicate references in the bibliography.

Dividing equation (2-2) by $\varepsilon$

$$\sigma T^4 = \alpha_{s/\varepsilon} F_s Q_s + \alpha_{s/\varepsilon} F_a Q_a + F_p Q_p + Q_{v/\varepsilon} . \qquad (2\text{-}3)$$

For most missions the vehicle internal energy dissipation and planet radiation is very small compared to the solar and albedo radiation. With this assumption, equation (2-3) can be reduced to

$$\sigma T^4 = \alpha_{s/\varepsilon} (F_s Q_s + F_a Q_a) . \qquad (2\text{-}4)$$

From equation (2-4), it is noted that the temperature of the vehicle is proportional to $(\alpha_{s/\varepsilon})^{\frac{1}{4}}$, since for any given vehicle configuration and orbit the incident solar energy is constant.

Although a complete analysis of the thermal load on a space vehicle is much more difficult that that depicted by equation (2-1), the importance of optical properties as related to the thermal-control coatings is well established. The thermal-control designer must have a full knowledge, not only of the initial $\alpha_{s/\varepsilon}$ values of the thermal coatings, but also the change in $\alpha_{s/\varepsilon}$ values that will be brought about by degradation of the material when exposed to the space environment. A more detailed mathematical development and an exact analytical approach for different vehicle configurations, under various launch and orbital conditions, is presented by Hass, et al. (1), Heller (2), and Camack and Edwards (3).

The present state-of-art of the thermal design of space systems requires a determination of the degree of degradation of these materials in a simulated environment. Testing of thermal-control materials, in most cases, has been accomplished in a simulated environment with little regard to the synergistic and accelerated testing effects.

The objective of this research was to experimentally investigate the effects of low density, temperature, proton radiation and electromagnetic radiation on thermal-control materials. Materials with a specified ratio of $\alpha_s$ (solar absorptance) to $\epsilon$ (infrared emittance) were selected for evaluation. Results of the investigation are presented in Chapter IX.

# CHAPTER III

# RADIATION ENVIRONMENT OF SPACE

## Solar Radiation

The bulk of energy in the solar spectrum lies between the wavelength limits 0.3$\mu$ to 4.0$\mu$ (1$\mu$ = $10^{-4}$ cm = $10^{4}$ Å), with approximately 1 per cent of the energy lying beyond each of these limits. The distribution of energy in the solar radiation incident on the earth's upper atmosphere is shown in Figure 2, and the values of spectral irradiance are given in Table I (4). These values apply when the earth is at a mean distance from the sun. The solar constant is equal to the area under the curve in Figure 2 and has the value 0.140 W/cm$^2$. The solar spectrum can be arranged on a scale of frequency, or energy content as shown in Figure 3.

Spectral irradiance values for wavelengths shorter than 0.2$\mu$ are well approximated by a 4500° K blackbody source. These values, based principally on such a source, are shown in Table I. In addition to this continuum radiation there are a number of emission lines which contribute a small amount of energy when compared to the continuum at wavelengths longer than 1400 Å, but at the same time contribute the major portion of the solar radiation at wavelengths shorter than 1400 Å. A list of the stronger lines which have been observed and their intensities are given in Table II (5). The solar spectrum below 1000 Å is shown in

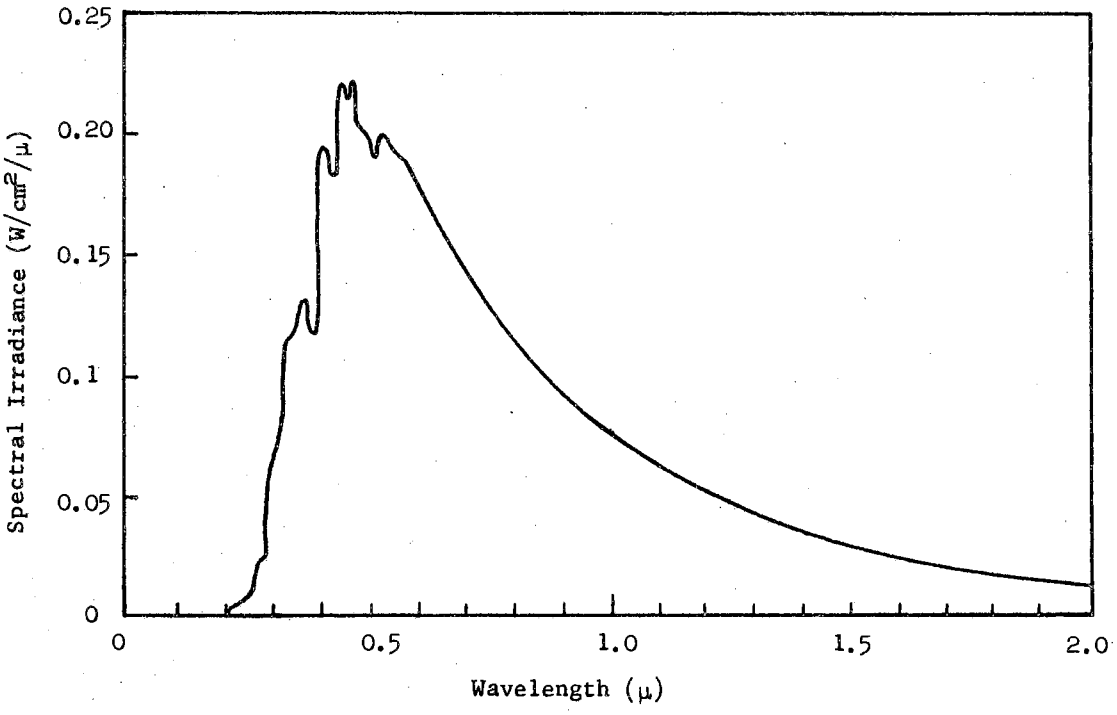


Figure 2. Solar Spectral Irradiance Outside the Earth's Atmosphere at the Earth's Mean Distance from the Sun (Ref. 4)

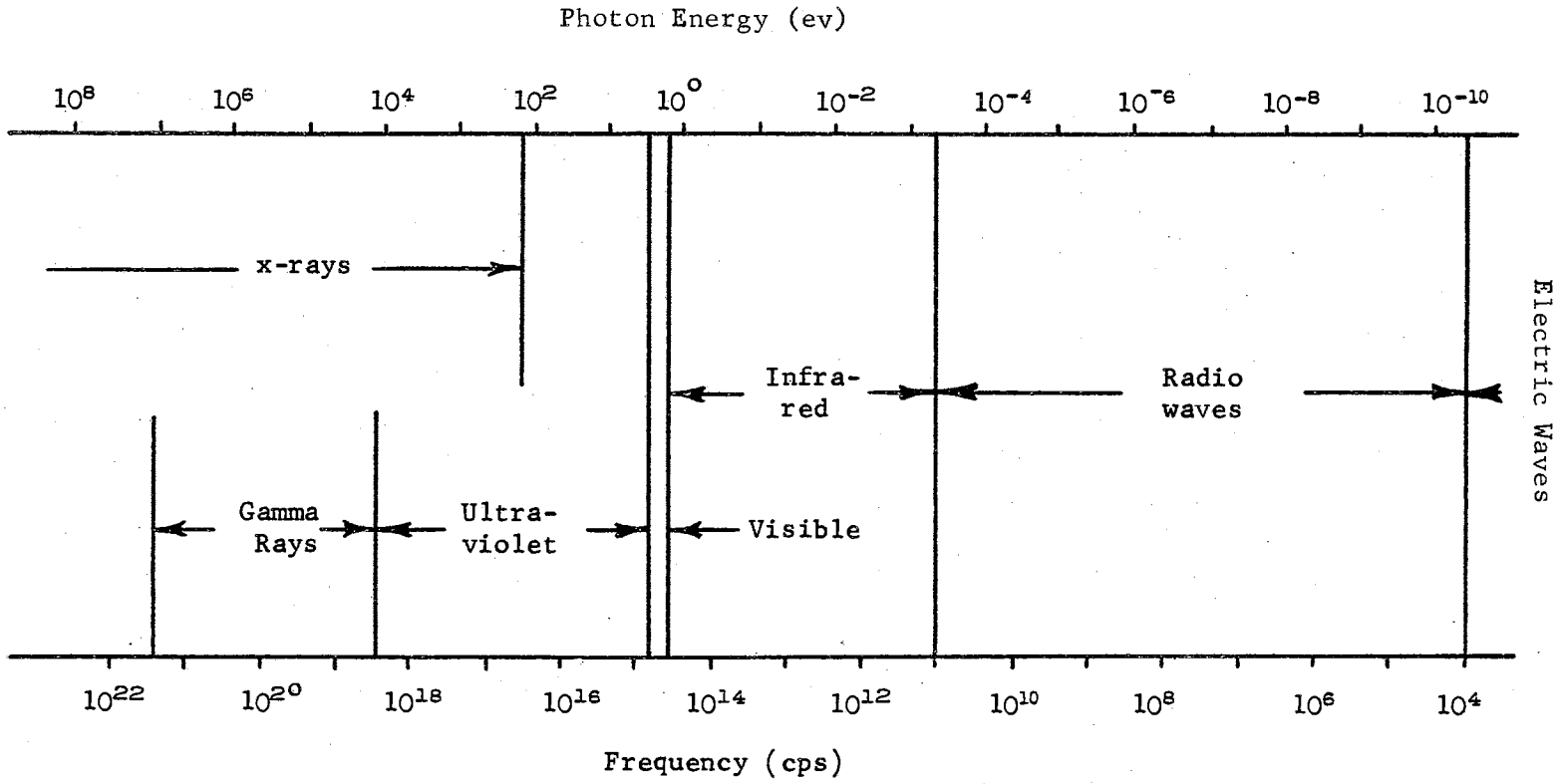


Figure 3. The Electromagnetic Spectrum on Log Frequency (energy) Scale

# TABLE I

## SOLAR SPECTRAL IRRADIANCE DATA (Ref. 4)

| $\lambda$ ($\mu$) | $H_\lambda$ (W/cm$^2$/$\mu$) | $P_\lambda$ (%) | $\lambda$ ($\mu$) | $H_\lambda$ (W/cm$^2$/$\mu$) | $P_\lambda$ (%) | $\lambda$ ($\mu$) | $H_\lambda$ (W/cm$^2$/$\mu$) | $P_\lambda$ (%) |
|---|---|---|---|---|---|---|---|---|
| 0.14 | $2 \times 10^{-6}$ | $9 \times 10^{-4}$ | 0.42 | 0.102 | 11.7 | 0.74 | 0.130 | 52.7 |
| 0.15 | $7 \times 10^{-6}$ | $9 \times 10^{-4}$ | 0.425 | 0.189 | 12.4 | 0.75 | 0.127 | 53.7 |
| 0.16 | $1.8 \times 10^{-6}$ | $1.0 \times 10^{-3}$ | 0.43 | 0.178 | 13.0 | 0.80 | 0.1127 | 57.9 |
| 0.17 | $4.1 \times 10^{-5}$ | $1.2 \times 10^{-3}$ | 0.435 | 0.182 | 13.7 | 0.85 | 0.1003 | 61.7 |
| 0.18 | $9.1 \times 10^{-5}$ | $1.7 \times 10^{-3}$ | 0.44 | 0.203 | 14.4 | 0.90 | 0.895 | 65.1 |
| 0.19 | $1.7 \times 10^{-4}$ | $2.5 \times 10^{-3}$ | 0.445 | 0.215 | 15.1 | 0.95 | 0.0803 | 68.1 |
| 0.20 | $3 \times 10^{-4}$ | $3.4 \times 10^{-3}$ | 0.45 | 0.220 | 15.9 | 1.0 | 0.0725 | 70.9 |
| 0.205 | $5 \times 10^{-4}$ | $5 \times 10^{-3}$ | 0.455 | 0.219 | 16.7 | 1.1 | 0.0606 | 75.7 |
| 0.21 | $1.0 \times 10^{-3}$ | $8 \times 10^{-3}$ | 0.46 | 0.216 | 17.5 | 1.2 | 0.0501 | 79.6 |
| 0.215 | $1.8 \times 10^{-3}$ | $1.1 \times 10^{-2}$ | 0.465 | 0.215 | 18.2 | 1.3 | 0.0406 | 82.9 |
| 0.22 | 0.0030 | 0.02 | 0.47 | 0.217 | 19.0 | 1.4 | 0.0328 | 85.5 |
| 0.225 | 0.0042 | 0.03 | 0.475 | 0.220 | 19.8 | 1.5 | 0.0267 | 87.6 |
| 0.23 | 0.0052 | 0.05 | 0.48 | 0.216 | 20.6 | 1.6 | 0.0220 | 89.4 |
| 0.235 | 0.0054 | 0.07 | 0.485 | 0.203 | 21.3 | 1.7 | 0.0182 | 90.83 |
| 0.24 | 0.0058 | 0.09 | 0.49 | 0.199 | 22.0 | 1.8 | 0.0152 | 92.03 |
| 0.245 | 0.0064 | 0.11 | 0.495 | 0.204 | 22.8 | 1.9 | 0.01274 | 93.02 |
| 0.25 | 0.0064 | 0.13 | 0.50 | 0.198 | 23.5 | 2.0 | 0.01079 | 93.87 |
| 0.255 | 0.010 | 0.16 | 0.505 | 0.197 | 24.2 | 2.1 | 0.00917 | 94.58 |
| 0.26 | 0.013 | 0.20 | 0.51 | 0.196 | 24.9 | 2.2 | 0.00785 | 95.20 |
| 0.265 | 0.020 | 0.27 | 0.515 | 0.189 | 25.6 | 2.3 | 0.00676 | 95.71 |
| 0.27 | 0.025 | 0.34 | 0.52 | 0.187 | 26.3 | 2.4 | 0.00585 | 96.18 |
| 0.275 | 0.022 | 0.43 | 0.525 | 0.192 | 26.9 | 2.5 | 0.00509 | 96.57 |
| 0.28 | 0.024 | 0.51 | 0.53 | 0.195 | 27.6 | 2.6 | 0.00445 | 96.90 |
| 0.285 | 0.034 | 0.62 | 0.535 | 0.197 | 28.3 | 2.7 | 0.00390 | 97.21 |
| 0.29 | 0.052 | 0.77 | 0.54 | 0.198 | 29.0 | 2.8 | 0.00343 | 97.47 |
| 0.295 | 0.063 | 0.98 | 0.545 | 0.198 | 29.8 | 2.9 | 0.00303 | 97.72 |
| 0.30 | 0.061 | 1.23 | 0.55 | 0.195 | 30.5 | 3.0 | 0.00268 | 97.90 |
| 0.305 | 0.067 | 1.43 | 0.555 | 0.192 | 31.2 | 3.1 | 0.00230 | 98.08 |
| 0.31 | 0.076 | 1.69 | 0.56 | 0.190 | 31.8 | 3.2 | 0.00214 | 98.24 |
| 0.315 | 0.082 | 1.97 | 0.565 | 0.189 | 32.5 | 3.3 | 0.00191 | 98.39 |
| 0.32 | 0.085 | 2.26 | 0.57 | 0.187 | 33.2 | 3.4 | 0.00171 | 98.52 |
| 0.325 | 0.102 | 2.60 | 0.575 | 0.187 | 33.9 | 3.5 | 0.00153 | 98.63 |
| 0.33 | 0.115 | 3.02 | 0.58 | 0.187 | 34.5 | 3.6 | 0.00139 | 98.74 |
| 0.335 | 0.111 | 3.40 | 0.585 | 0.185 | 35.2 | 3.7 | 0.00125 | 98.83 |
| 0.34 | 0.111 | 3.80 | 0.59 | 0.184 | 35.9 | 3.8 | 0.00114 | 98.91 |
| 0.345 | 0.117 | 4.21 | 0.595 | 0.183 | 36.5 | 3.9 | 0.00103 | 98.99 |
| 0.35 | 0.118 | 4.63 | 0.60 | 0.181 | 37.2 | 4.0 | 0.00095 | 99.05 |
| 0.355 | 0.116 | 5.04 | 0.61 | 0.177 | 38.4 | 4.1 | 0.00087 | 99.13 |
| 0.36 | 0.116 | 5.47 | 0.62 | 0.174 | 39.7 | 4.2 | 0.00080 | 99.18 |
| 0.365 | 0.129 | 5.89 | 0.63 | 0.170 | 40.9 | 4.3 | 0.00073 | 99.23 |
| 0.37 | 0.133 | 6.36 | 0.64 | 0.166 | 42.1 | 4.4 | 0.00067 | 99.29 |
| 0.375 | 0.132 | 6.84 | 0.65 | 0.162 | 43.3 | 4.5 | 0.00061 | 99.33 |
| 0.38 | 0.123 | 7.29 | 0.66 | 0.159 | 44.5 | 4.6 | 0.00056 | 99.38 |
| 0.385 | 0.115 | 7.72 | 0.67 | 0.155 | 45.6 | 4.7 | 0.00051 | 99.41 |
| 0.39 | 0.112 | 8.13 | 0.68 | 0.151 | 46.7 | 4.8 | 0.00048 | 99.45 |
| 0.395 | 0.120 | 8.54 | 0.69 | 0.148 | 47.8 | 4.9 | 0.00044 | 99.48 |
| 0.40 | 0.154 | 9.03 | 0.70 | 1.144 | 48.8 | 5.0 | 0.00042 | 99.51 |
| 0.405 | 0.188 | 9.65 | 0.71 | 0.141 | 49.8 | 6.0 | 0.00021 | 99.74 |
| 0.41 | 0.194 | 10.3 | 0.72 | 0.137 | 50.8 | 7.0 | 0.00012 | 99.86 |
| 0.415 | 0.192 | 11.0 | 0.73 | 0.134 | 51.8 | 8.0 | 0.00006 | 99.93 |

$\lambda$ = wavelength; $H_\lambda$ = mean zero air mass spectral irradiance; $P_\lambda$ = percentage of the solar constant associated with wavelengths shorter than the tabulated $\lambda$.

TABLE II

SOLAR ULTRAVIOLET SPECTRAL-LINE INTENSITIES (Ref. 5)

| Atom | Wavelength (Å) | Mean Solar Irradiance ($w/cm^2$) x $10^8$ |
|---|---|---|
| Si II | 1817 | 2.0 |
| Si II | 1808 | 0.7 |
| Al II | 1671 | 0.1 |
| Fe II | 1663 | 0.3 |
| Fe II | 1660 | 0.4 |
| C I | 1656-1658 | 1.8 |
| He II | 1640 | 0.1 |
| C I | 1560-1561 | 0.7 |
| C IV | 1550 | 0.4 |
| C IV | 1548 | 0.5 |
| Si II | 1533 | 0.2 |
| Si II | 1527 | 0.2 |
| Si IV | 1403 | 0.1 |
| Si IV | 1394 | 0.2 |
| C II | 1336 | 0.6 |
| C II | 1135 | 0.5 |
| Si II | 1309 | 0.1 |
| O I | 1306 | 0.4 |
| O I | 1305 | 0.3 |
| O I | 1302 | 0.2 |
| Si II | 1265 | 0.2 |
| Si II | 1261 | 0.1 |
| S II | 1260 | 0.1 |
| N V | 1239 | 0.1 |
| H I | 1216 | 60.0 |
| Si III | 1206 | 0.1 |
| C III | 1175-1176 | 0.5 |
| N II | 1086 | 0.3 |
| O VI | 1038 | 0.8 |
| O VI | 1032 | 1.0 |
| H I | 1026 | 2.0 |
| C III | 977 | 2.0 |
| H I[(a)] | <912 | 1.5 |
| Mg X | 625 | 0.2 |
| O IV | 608 | 0.3 |
| He I | 585 | 0.4 |
| He II | 304 | 3.0 |

(a) Lyman continuum

Figure 4. The intensities in the spectral range below 1000 Å must be regarded as tentative. Below 220 Å, the spectrum consists of a rather dense distribution of spectral lines, and it is convenient to consider it as a continuum, rather than a line spectrum.

The solar spectrum below 0.3μ must be obtained from rocket or satellite observations, due to the opaqueness of the earth's atmosphere. Virtually none of the solar radiation in this spectral range reaches the earth's surface.

The visible and infrared (ultraviolet not included) portion of the solar spectrum is well approximated in spectral quality by radiation from a 6000° K blackbody. At wavelengths shorter than 0.2μ the solar spectral irradiance curve is well approximated by radiation from a 4500° K blackbody (6), (7). The total amount of radiation emitted by the sun is the same as that from a 5800° K blackbody.

## Albedo and Earth Radiation

Albedo radiation (reflected solar radiation), for near earth satellites, consists of ultraviolet, visible, and infrared energy, having wavelengths between 0.29μ and 4.0μ. The other component, earth emission, which makes up the thermal radiation exchange between the earth and the satellites, consists of infrared energy, nearly all at wavelengths longer than 4.0μ. For earth radiation, it is of less importance to establish a spectral distribution for use in thermal-control design of space systems because most materials possess a monochromatic absorptance which is practically independent of wavelength in the spectral region of earth radiation. The best estimate for the behavior of earth emission and

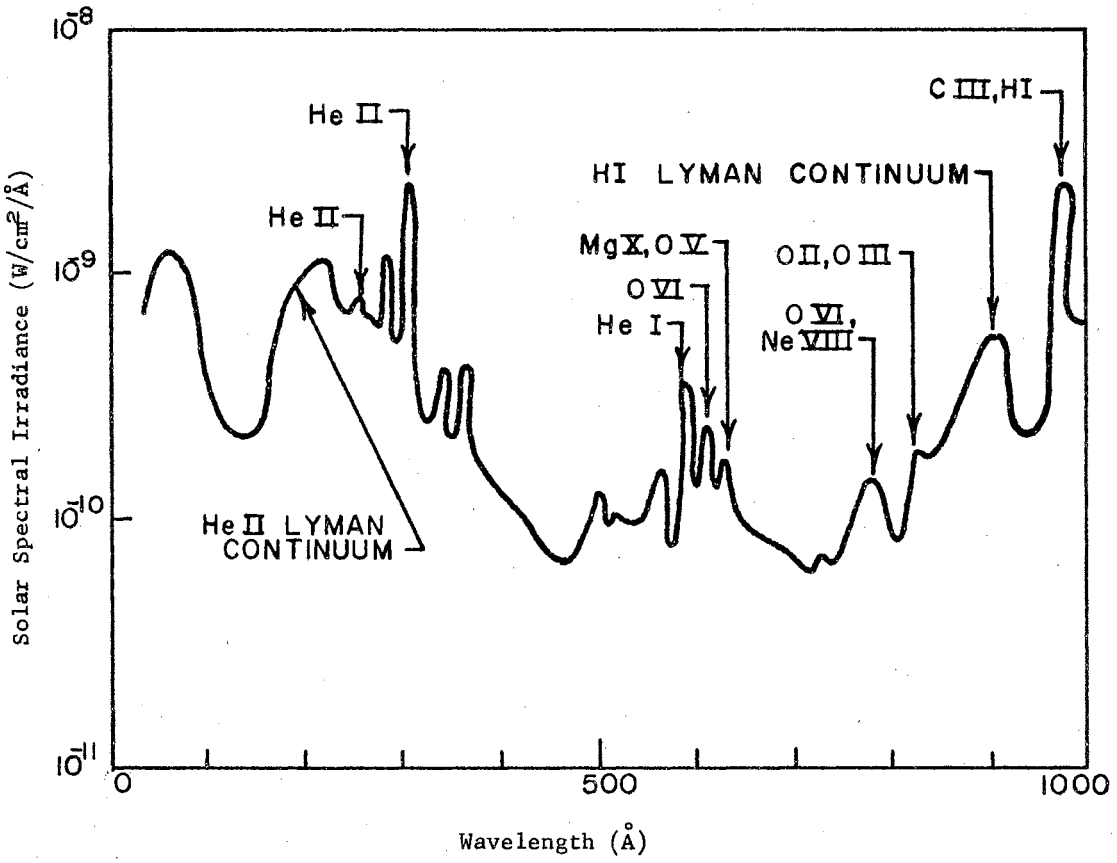


Figure 4. Solar Ultraviolet Spectral Irradiance Above the Earth's Atmosphere. The lines are shown with an effective line width of 10Å (Ref. 7)

albedo radiation as a function of latitude for earth albedo radiation is shown in Figures 5 and 6. The relative spectral distribution of albedo radiations for three sky conditions are listed in Table III and plotted in Figure 7 (8).

## Particle Radiation

In the study of radiation effects on materials, the radiation particles of greatest interest are electrons, protons, and neutrons which possess high penetrating power coupled with the faculty of producing structural changes in matter.

The principle particle radiation environments that a satellite or a space vehicle encounters are:

a. the ionosphere

b. the auroral zone

c. the Van Allen radiation belts

d. the cosmic rays

e. the solar wind

The ionosphere consists (9) of a succession of four distinct ionized layers that blend into one another. The lowest level is the "D" layer, lying between 60 and 85 km. This layer is believed to be formed by photo-dissociation of atmospheric atoms by solar Lyman-$\alpha$ (1216 Å) radiation. It is thickest and most dense at local noon and disappears completely at night. Because the local air density is high, the electron collision frequency is high; therefore, the region is a strong absorber of electromagnetic energy.

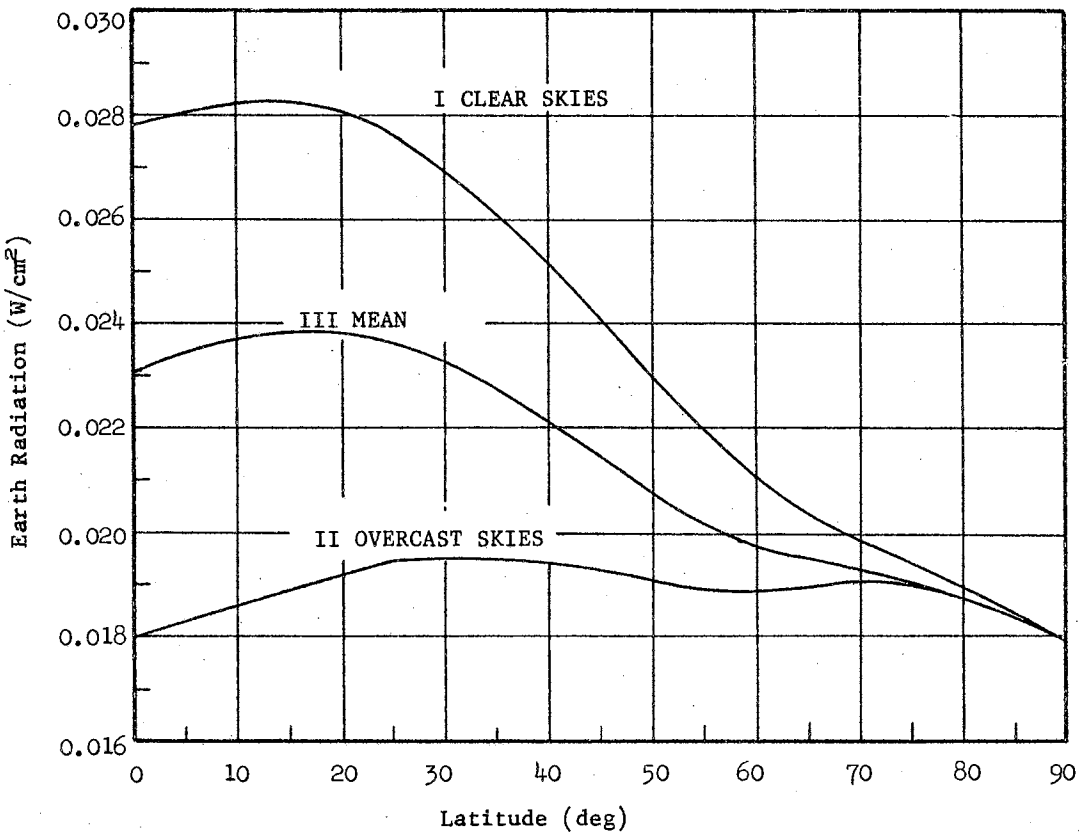


Figure 5. Earth Radiation as a Function of Latitude Under Various Sky Conditions (Ref. 8)

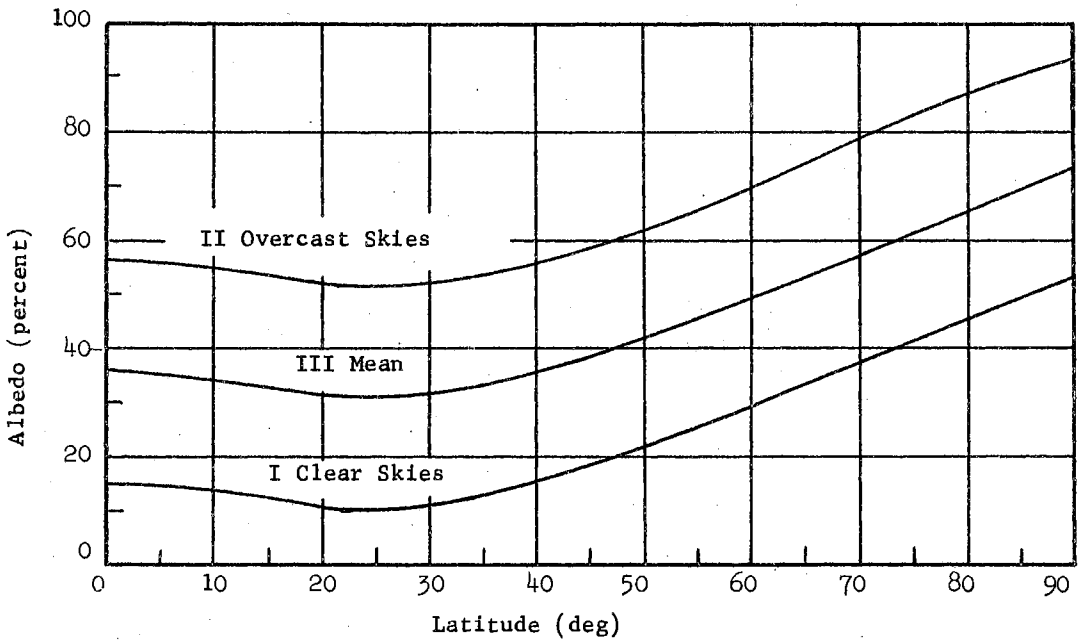


Figure 6. Albedo as a Function of Latitude Under Various Sky Conditions (Ref. 8)

TABLE III

RELATIVE SPECTRAL DISTRIBUTION OF ALBEDO RADIATION

UNDER VARIOUS SKY CONDITIONS (Ref. 8)

| | $R_\lambda^{(a)}$ | | | | $R_\lambda^{(a)}$ | | |
|---|---|---|---|---|---|---|---|
| $\lambda$ ($\mu$) | Clear Skies | Mean | Overcast Skies | $\lambda$ ($\mu$) | Clear Skies | Mean | Overcast Skies |
| 0.29 | 0 | 0 | 0 | 0.53 | 0.378 | 0.668 | 0.807 |
| 0.30 | 0.882 | 0.721 | 0.477 | 0.54 | 0.252 | 0.663 | 0.812 |
| 0.31 | 0.892 | 0.761 | 0.534 | 0.55 | 0.333 | 0.637 | 0.795 |
| 0.32 | 0.848 | 0.749 | 0.553 | 0.56 | 0.312 | 0.615 | 0.770 |
| 0.33 | 1.000 | 0.920 | 0.705 | 0.57 | 0.288 | 0.590 | 0.752 |
| 0.34 | 0.858 | 0.813 | 0.648 | 0.58 | 0.276 | 0.581 | 0.748 |
| 0.35 | 0.815 | 0.802 | 0.661 | 0.59 | 0.262 | 0.563 | 0.734 |
| 0.36 | 0.744 | 0.746 | 0.634 | 0.60 | 0.241 | 0.541 | 0.717 |
| 0.37 | 0.768 | 0.796 | 0.700 | 0.70 | 0.134 | 0.396 | 0.554 |
| 0.38 | 0.671 | 0.714 | 0.632 | 0.80 | 0.084 | 0.293 | 0.425 |
| 0.39 | 0.575 | 0.624 | 0.570 | 0.90 | 0.057 | 0.224 | 0.331 |
| 0.40 | 0.758 | 0.840 | 0.772 | 1.00 | 0.042 | 0.179 | 0.266 |
| 0.41 | 0.781 | 1.000 | 0.950 | 1.10 | 0.028 | 0.149 | 0.219 |
| 0.42 | 0.790 | 0.937 | 0.925 | 1.20 | 0.019 | 0.118 | 0.181 |
| 0.43 | 0.675 | 0.835 | 0.835 | 1.30 | 0.017 | 0.095 | 0.145 |
| 0.44 | 0.708 | 0.908 | 0.934 | 1.40 | 0.015 | 0.076 | 0.115 |
| 0.45 | 0.734 | 0.958 | 1.000 | 1.50 | 0.013 | 0.063 | 0.093 |
| 0.46 | 0.649 | 0.892 | 0.960 | 1.60 | 0.010 | 0.051 | 0.078 |
| 0.47 | 0.713 | 0.864 | 0.954 | 1.70 | 0.008 | 0.042 | 0.063 |
| 0.48 | 0.563 | 0.834 | 0.935 | 1.80 | 0.006 | 0.034 | 0.052 |
| 0.49 | 0.487 | 0.749 | 0.853 | 1.90 | 0.005 | 0.029 | 0.045 |
| 0.50 | 0.452 | 0.727 | 0.840 | 2.00 | 0.005 | 0.025 | 0.037 |
| 0.51 | 0.422 | 0.697 | 0.825 | 4.00 | 0.000 | 0.002 | 0.028 |
| 0.52 | 0.378 | 0.650 | 0.780 | | | | |

(a) $R_\lambda$ = the ratio of the spectral irradiance at wavelength $\lambda$ to the spectral irradiance at the wavelength of maximum intensity

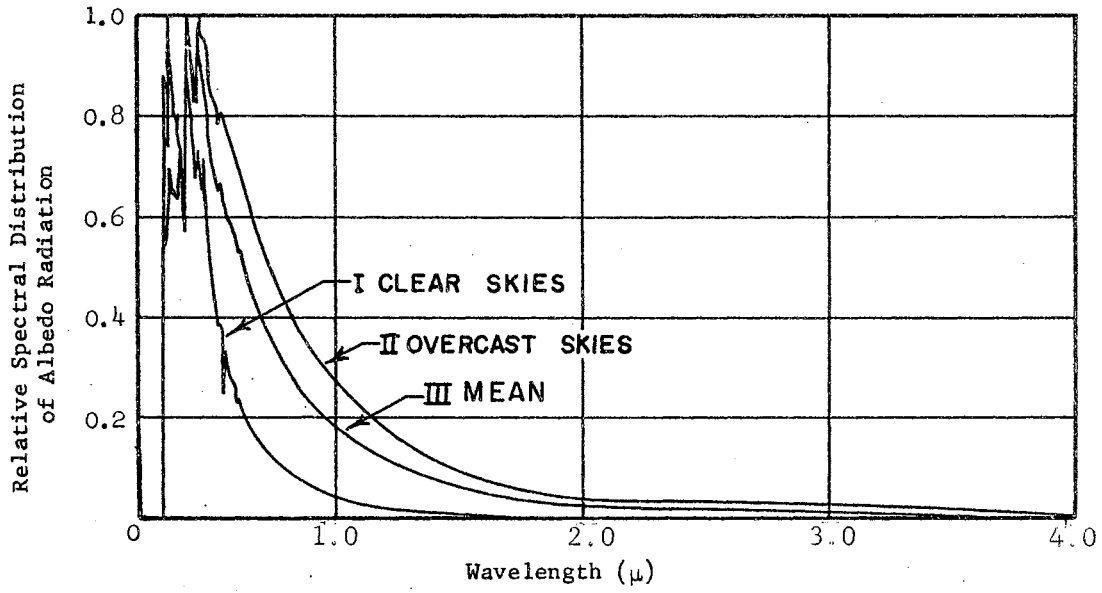


Figure 7. Relative Spectral Distributions of Albedo Radiation Under Various Sky Conditions (Ref. 8)

The next highest layer is the "E" layer, lying between 85 and 140 km. Photo-ionization is believed to be the cause of the formation of this layer and is initiated by solar x-ray radiation, and the densest electron concentration occurs at local noon. Occasionally a very thin, intense layer, a few kilometers thick (called the sporadic "E" layer) forms within the main "E" layer and results in abnormal ratio propagation.

The upper two layers are the "F" 1 and "F" 2 layers. Radiation emitted by the $He_{II}$ ion at 304 Å is believed to be the cause of the formation of these layers. The layers are very distinct in the daytime but amalgamate during the night. Both regions possess the highest electron concentration in the ionosphere--about 2.5 to 4.0 x $10^5$ electrons $cm^{-3}$--at local noon. The altitude of peak density is about 300 km. Above this the electron concentration falls off very slowly as the altitude increases.

The auroral radiation fluxes are found more frequently between 65 and 70 degrees north and south magnetic latitudes (10). The loci of the auroral radiation zones may be visualized as crown-like configurations sitting over the polar caps. They are regions of intermittent luminosity, which is produced by the collision of charged particles with the earth atmospheric atoms. As a result of the collisions, the electrons in the outer shells of the gas atoms have their energy levels raised. Subsequently electronic relaxation produces the visible glow. These luminous displays generally occur between 100 to 120 km altitude, but occasional bursts have been measured at altitudes of 700 to 1200 km.

Electron fluxes measured during auroral storms are quite high ($10^{11}$ electrons $cm^{-2} \cdot sec^{-1}$). The energy range is about 10 to 100 kev.

Auroral proton fluxes are much lower than the auroral electron fluxes. The flux is about $10^5$ protons $cm^{-2}$ - $sec^{-1}$, with energies ranging up to approximately 650 kev.

The Van Allen radiation belts are composed of an "inner" and "outer" belt. Radiation detectors carried on Explorer 12 indicated that the inner and outer belts overlap noticeably and that the outer belt occasionally possesses two zones of maximum intensity (11). However, since previous measurements are strongly indicative of different origins for the particles in each major zone, the concept of two distinct zones will be maintained. Figure 8 illustrates a typical cross-section of the radiation zones.

The most notable feature of the inner belt is its stability. The intensity of this belt remains almost constant, even during periods of intense solar activity. This is probably due to the effective shielding provided this zone by the outer zone. The inner belt is composed mostly of penetrating protons ($E < 500$ Mev) and low-energy electrons ($E < 1$ Mev).

The outer belt is composed of much less energetic protons and high-energy electrons. The zone is extremely variable in both depth and intensity. Explorer 12 data indicate that intensity varies by a factor of ten (12). Figures 9, 10, and 11 present a reasonable estimate of the proton and electron energy fluxes associated with the Van Allen radiation belts.

Cosmic rays are normally classified as primary and solar. Primary cosmic rays may originate from galactic or extra galactic origin and are very high-energy particles (from 0.5 Bev to 20 Bev normally but they occasionally reach as high as $10^{10}$ Bev)(13). Table IV gives the

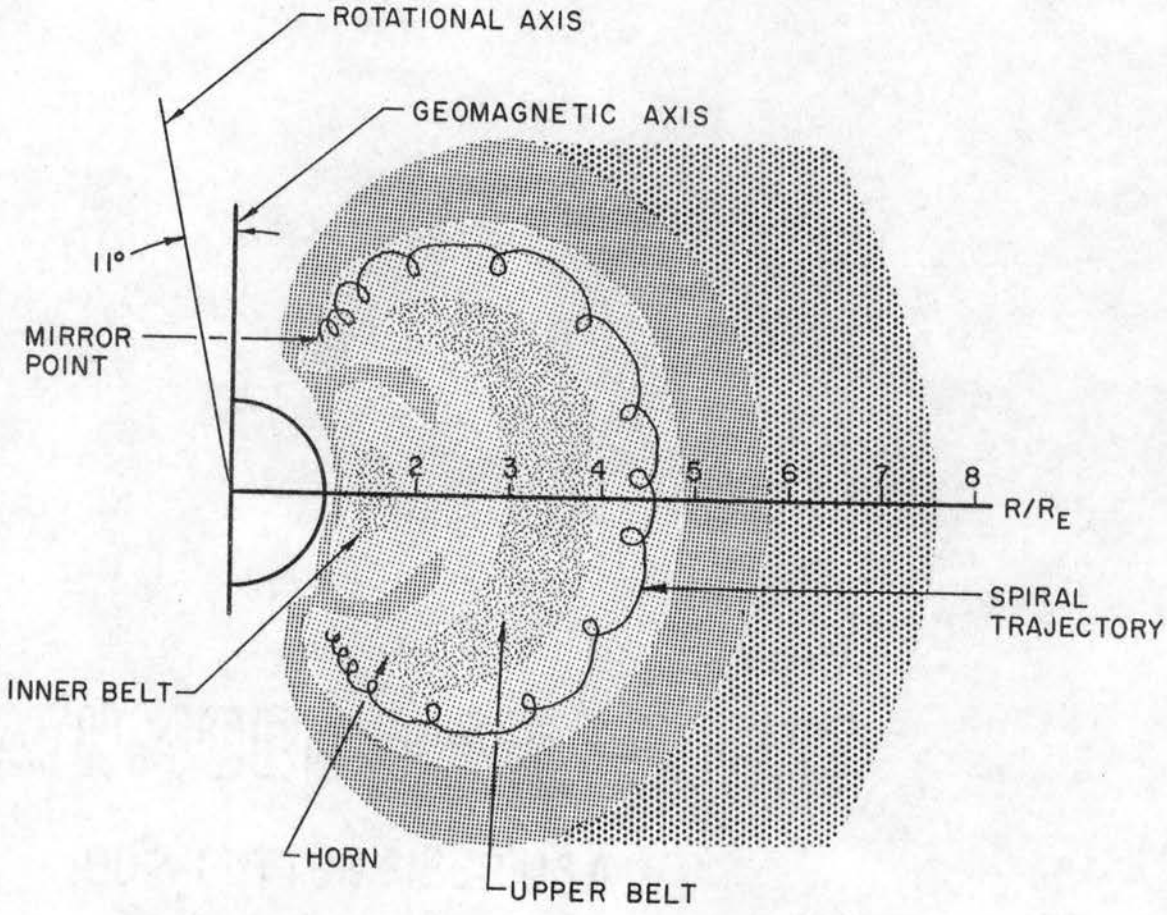


Figure 8. Van Allen Belt Structure

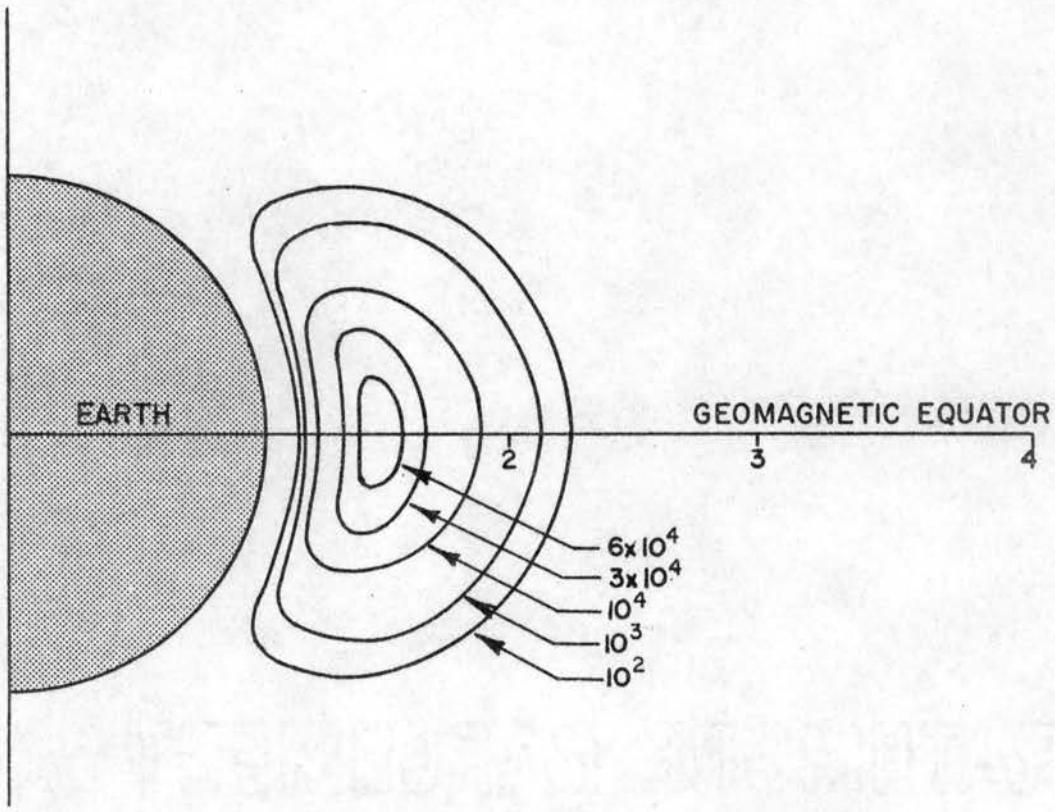


Figure 9. Contours of Constant Flux (protons/cm$^2$-sec) of Van Allen Protons Having Energies Greater Than 30 Mev; Radial Distance is in Earth Radii $R_E$ ($R_E$ = 3440 nm) (Ref. 10)

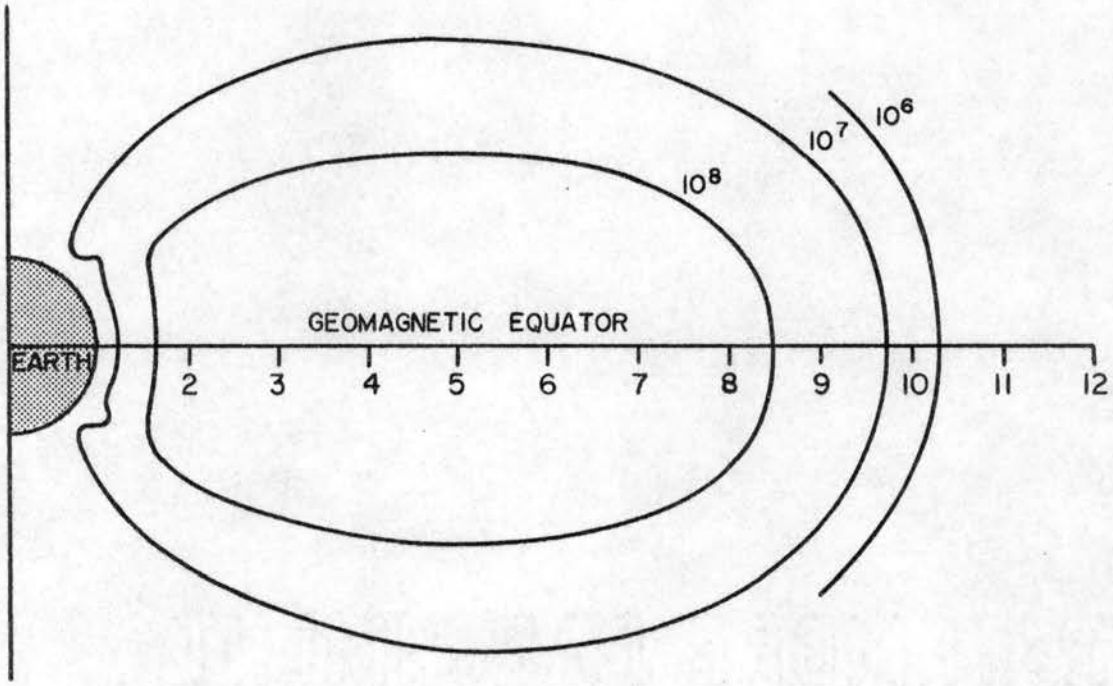


Figure 10. Contours of Constant Flux (electrons/cm$^2$-sec) of Van Allen Electrons Having Energies Greater Than 40 kev (Ref. 10); Radial Distance in Earth Radii

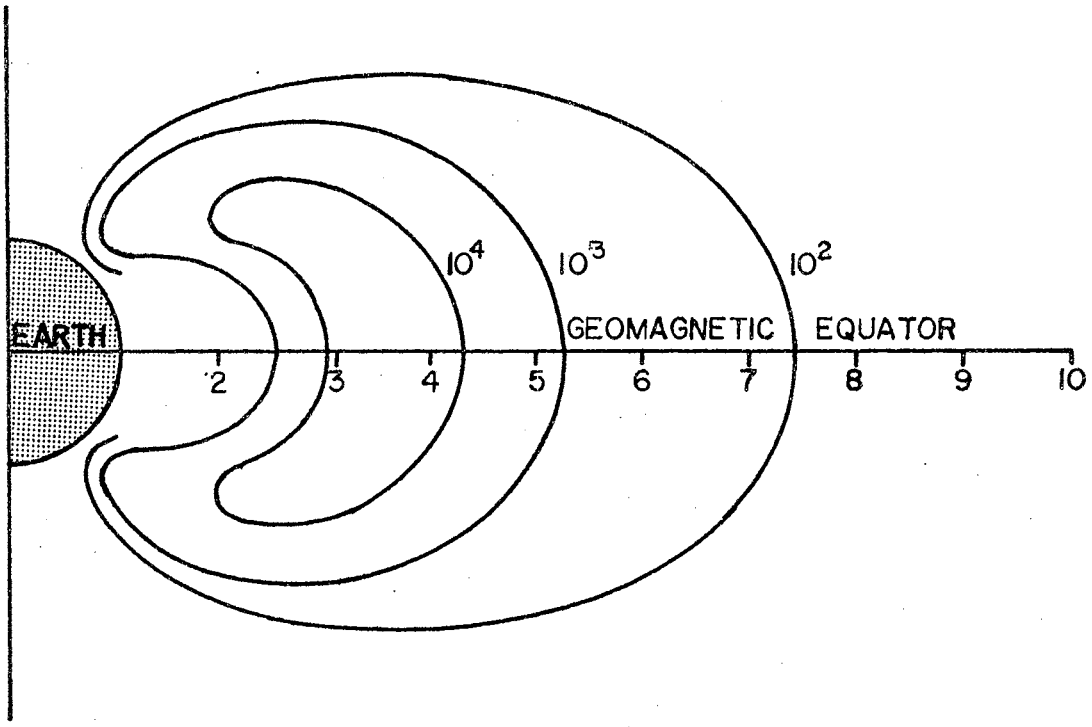


Figure 11. Contours of Constant Flux (electrons/$cm^2$-sec) of Van Allen Electrons Having Energies Greater Than 1.6 Mev (Ref. 10); Radial Distance in Earth Radii

TABLE IV

COMPOSITION OF GALACTIC COSMIC PARTICLES (Ref. 13)

| Particles | Flux (R=4.5 Bev)*** | Percent |
|---|---|---|
| Protons | ~ .77/cm$^2$ sec | ~ 84% |
| Alpha Particles | ~ .11/cm$^2$ sec | ~ 14% |
| Carbon, Nitrogen, Oxygen** | ~.009/cm$^2$ sec | ~ 1% |
| Z > 10 | ~.002/cm$^2$ sec | ~0.25% |
| Gamma Radiation & Electrons** | | |

*May be a false indication from measurements made in atmosphere.

**Some space experiments have indicated that lower flares of gamma rays and high energy electrons may actually exist in the galactic spectrum.

***Rigidity, R, is the ratio of the particle's momentum to its charge R=Pc/Ze, where P is the momentum (in units of Bev/c), c is the velocity of light, Z is the atomic number, e is the unit charge, and the resulting R is in billion electron volts.

generalized composition of galactic cosmic radiation. The composition of the particles can be described as about 90 per cent protons (hydrogen nuclei), 10 per cent alpha particles (helium ions), plus small fractions of heavier ions having atomic numbers up to around 30 (10). High-energy gamma rays and electrons are virtually absent from cosmic rays fluxes. Table V gives the estimated flux of very high-energy galactic cosmic rays impinging each day from all directions on a spherical spaceship of 2 meters in radius. About 10 million cosmic rays of energy $\gtrsim 10^{12}$ ev would be expected to impinge on the spacecraft daily (17).

TABLE V

ESTIMATED FLUX OF VERY HIGH-ENERGY COSMIC RAYS ON A SMALL SPHERICAL SPACESHIP (Ref. 17)

| Cosmic-Ray Energy (ev) | Flux in Space (particles/$cm^2$ sec ster) | Flux on Sphere (particles/day) (radius $\cong$ 2 meter) |
|---|---|---|
| $\gtrsim 10^{12}$ | $10^{-4}$ | $10^{7}$ |
| $\gtrsim 10^{13}$ | $10^{-6}$ | $10^{5}$ |
| $\gtrsim 10^{14}$ | $10^{-8}$ | $10^{3}$ |
| $\gtrsim 10^{15}$ | $10^{-10}$ | $10^{1}$ |
| $\gtrsim 10^{16}$ | $10^{-11}$ | $10^{0}$ |
| $\gtrsim 10^{17}$ | $10^{-13}$ | $10^{-2}$ |

At times the surface of the sun becomes turbulent and ejects clouds of charged particles and streams of radio, visual, x-ray and gamma ray radiation in the surrounding space. These eruptions are known as flares and the charged particles are known as solar cosmic radiation. Protons

are by far the most abundant nuclei in these events. The total proton flux in free space resulting from these events varies over wide limits; namely, from a few protons/$cm^2$-sec to as much as $10^4$ protons/$cm^2$-sec (18). Figure 12 shows a cross plot of flux versus energy for a typical solar flare (19).

A large number of very low-energy particles are continuously given off by the sun in addition to the cosmic rays produced by solar flares. This stream of particles is called the solar winds. The most complete measurements made so far are those by Mariner II (10). Beyond the earth's gravitational field (outside the magnetosphere) was found a flux of $3 \times 10^7$ to $100 \times 10^7$ particles $cm^{-2}$ $sec^{-1}$ with energy varying between 200 to 800 ev.

The radiation belt of high-energy electrons, created by the high-altitude nuclear explosion (Starfish) over Johnston Island on July 9, 1962, and augmented by later Russian tests, is of vital importance when considering space radiation effects (10). The contours of constant electron flux is shown in Figure 13. The decay time of this artificial belt is so slow that it is appropriate to assume no further decay for missions in the near future.

The over-all particulate energy flux relationship for the space environment is depicted in Figure 14. This figure gives a pictorial view of the combined particle environment (20). One can see that the solar wind environment becomes a major constituent when the total energy of the regions are considered.

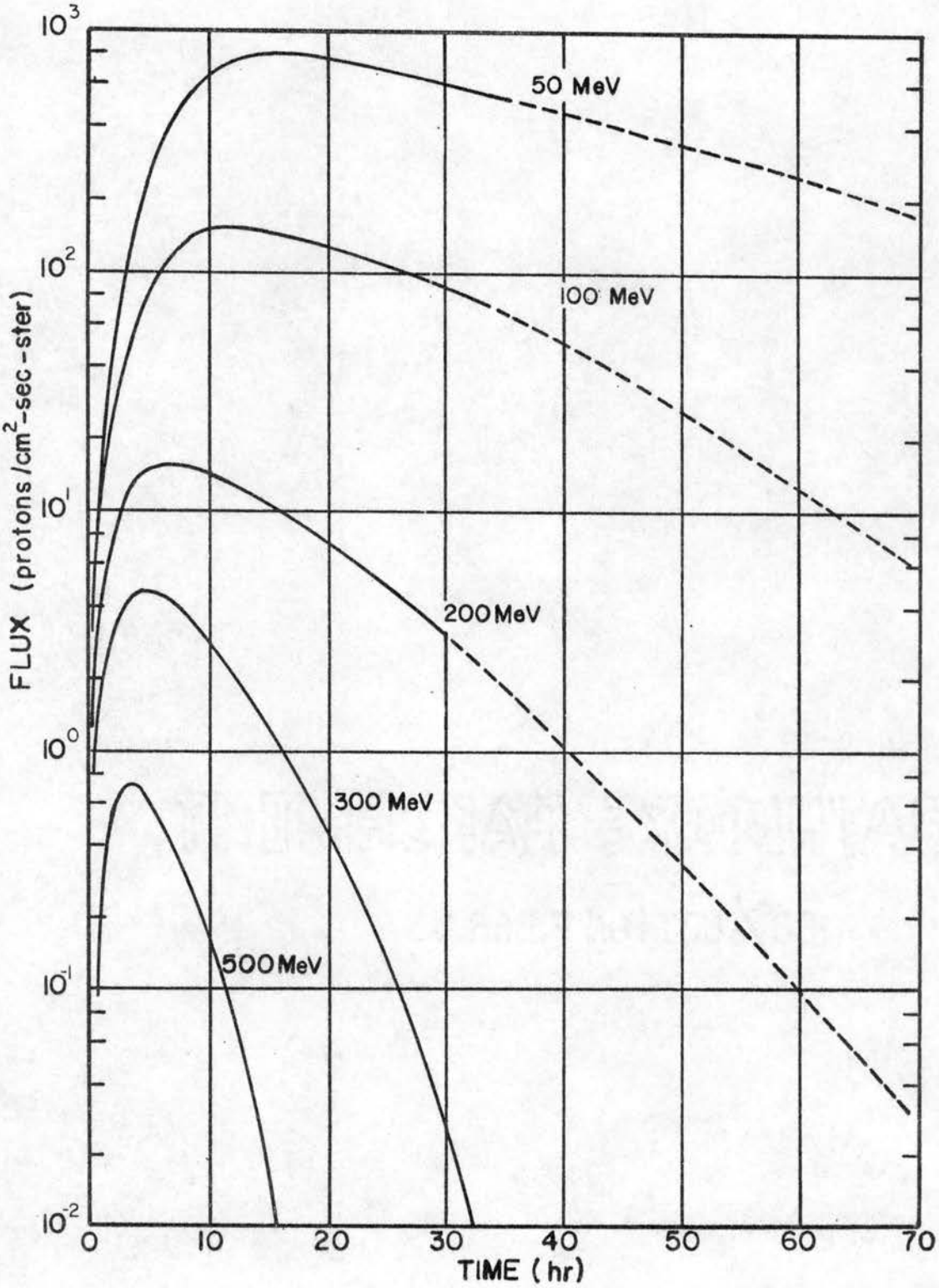


Figure 12. Time Behavior of Proton Flux for Bailey's Typical Solar Flare (Ref. 10)

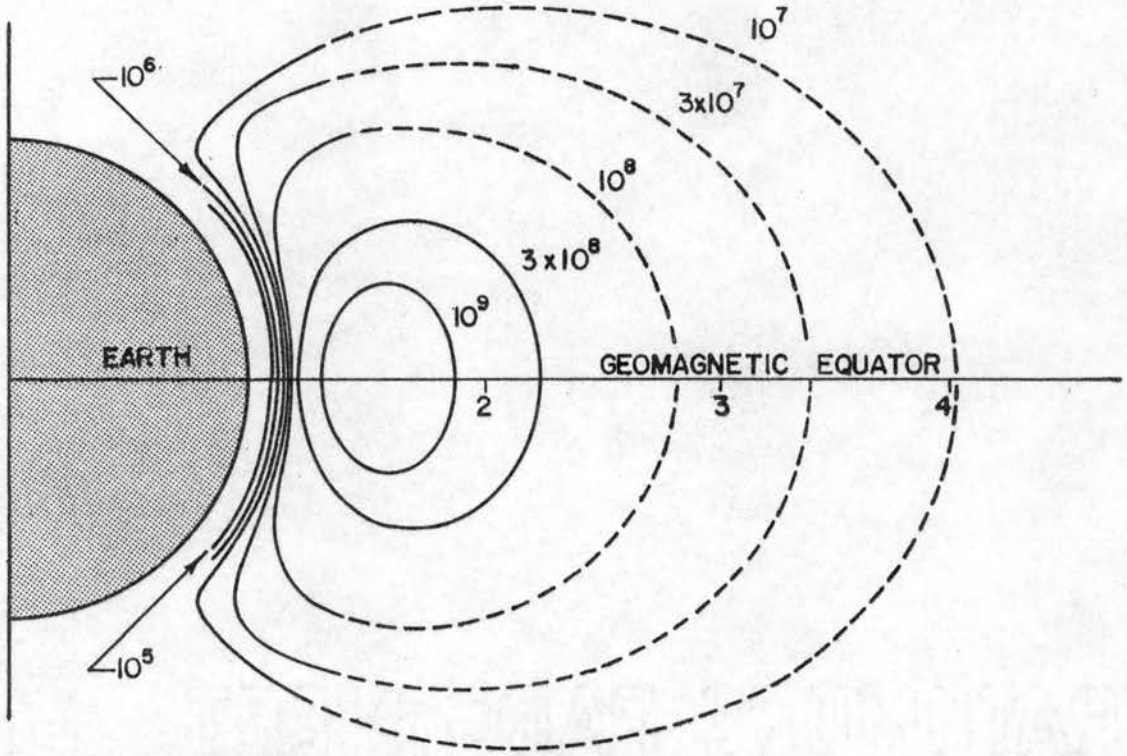


Figure 13. Contours of Constant Flux (electrons/$cm^2$-sec) of Artificial (Starfish) Electrons of all Energies; Dashed Lines Indicate Extrapolations (Ref. 10); Radial Distance in Earth Radii

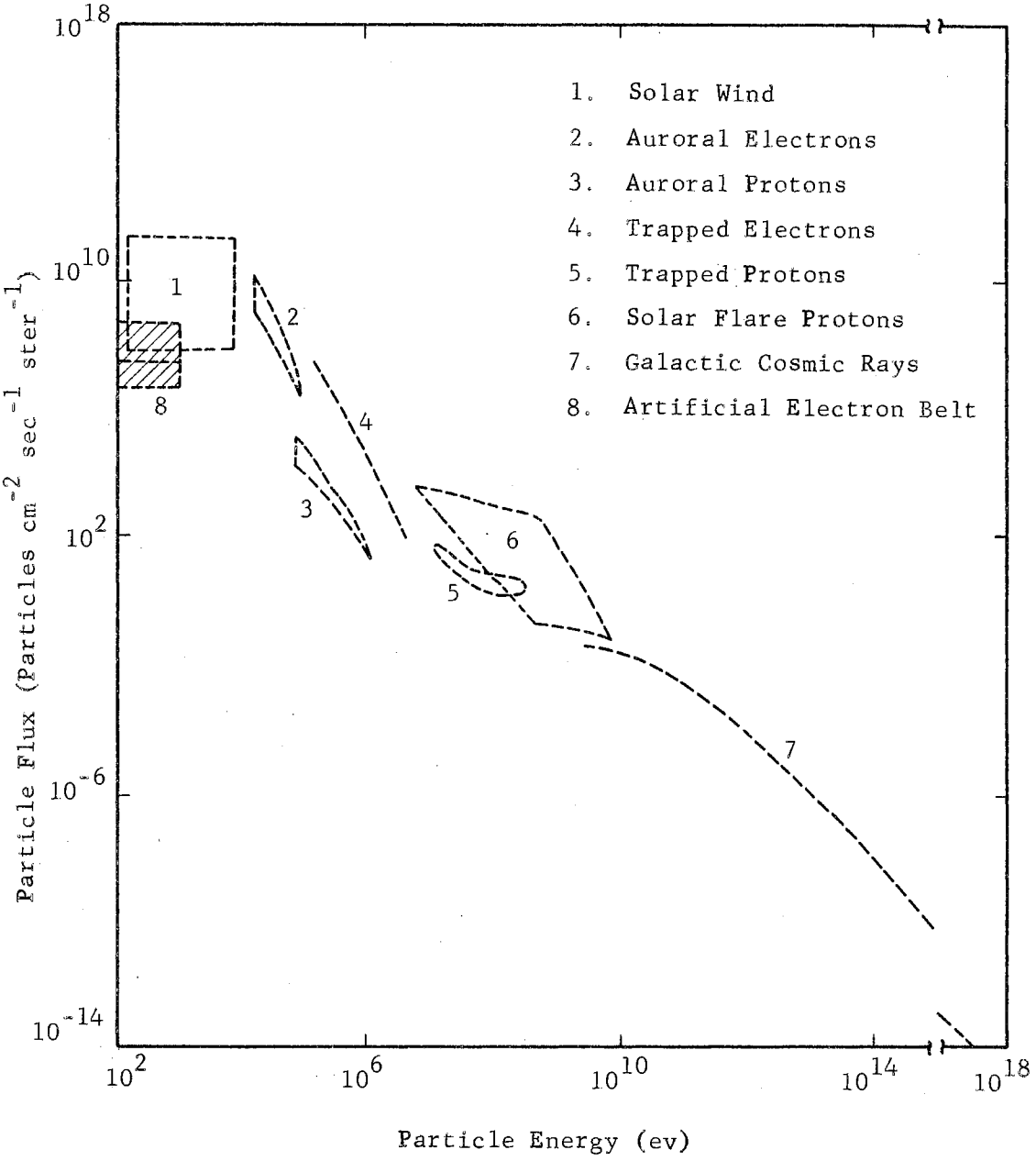


Figure 14. Over-all Spectra of Particles in Space

# CHAPTER IV

## MECHANISMS OF MATERIAL DAMAGE BY RADIATION

The principal penetrating radiation of interest is comprised of: (1) protons; (2) electrons; and (3) photons.

The first two are corpuscular (possess a measurable rest mass); whereas, the last one is electromagnetic (possesses zero rest mass). Hydrogen, whose nuclei is the proton, is by far the most abundant element in the universe. The electron is a negatively charged particle with a mass of $9.109 \times 10^{-28}$ gram which is about 1/1836 that of the proton.

The mechanism by which electromagnetic radiation interacts with materials is a complex function of the energy of the radiation and the atomic number of the material (21). At low energies, the photon can cause ejection of only weakly bound electrons surrounding an atom. As the photon energy increases it can cause ejection of more strongly bound electrons. The electromagnetic radiations arranged on a scale of wavelength, frequency, and energy content are shown in Figure 3. Material damage due to photon interaction is the result of three types; the photo-electric effect, the Compton process, and pair production.

In the photo-electric process a photon is completely absorbed in a collision with an electron and the electron is ejected from the atom. This can happen whenever the energy of the photon is greater than the

binding energy of the electron. The difference between the electron binding energy and the photon energy is carried away by the electron (22). Thus, the kinetic energy of the electron is given by

$$E = h\nu - \emptyset$$

where $h\nu$ is the photon energy and $\emptyset$ is the binding energy of the electron.

The Compton process is the result of an elastic collision between a photon and an electron in which part of the photon energy is transferred to the electron and the photon is scattered with reduced energy. For low incident photon energies, the scattered photon has nearly the same energy as the primary photon; and, as the energy is increased, the fraction removed by the scattered photon decreases and the electron receives an increasing share of the available energy.

If a photon has an energy greater than twice the equivalent energy of the rest mass of an electron, then the pair-production process can occur. Since the energy of a rest mass electron is $m_0c^2$ = .511 Mev, the minimum energy for a pair production is 1.02 Mev. In the pair production process the photon interacts with a nucleus and disappears with the production of two particles, a positive and a negative electron. The photon energy above the minimum 1.02 Mev appears primarily as kinetic energy of the pair of particles.

The energy region over which the three primary processes predominate is shown in Figure 15 (23). It can be seen in the region of interest, from a few tenths Mev to several Mev, that the Compton effect clearly predominates as the energy-transfer mechanism.

Both the ultraviolet and the soft x-ray components of the solar spectrum possess sufficient energy per quantum to induce rupture of

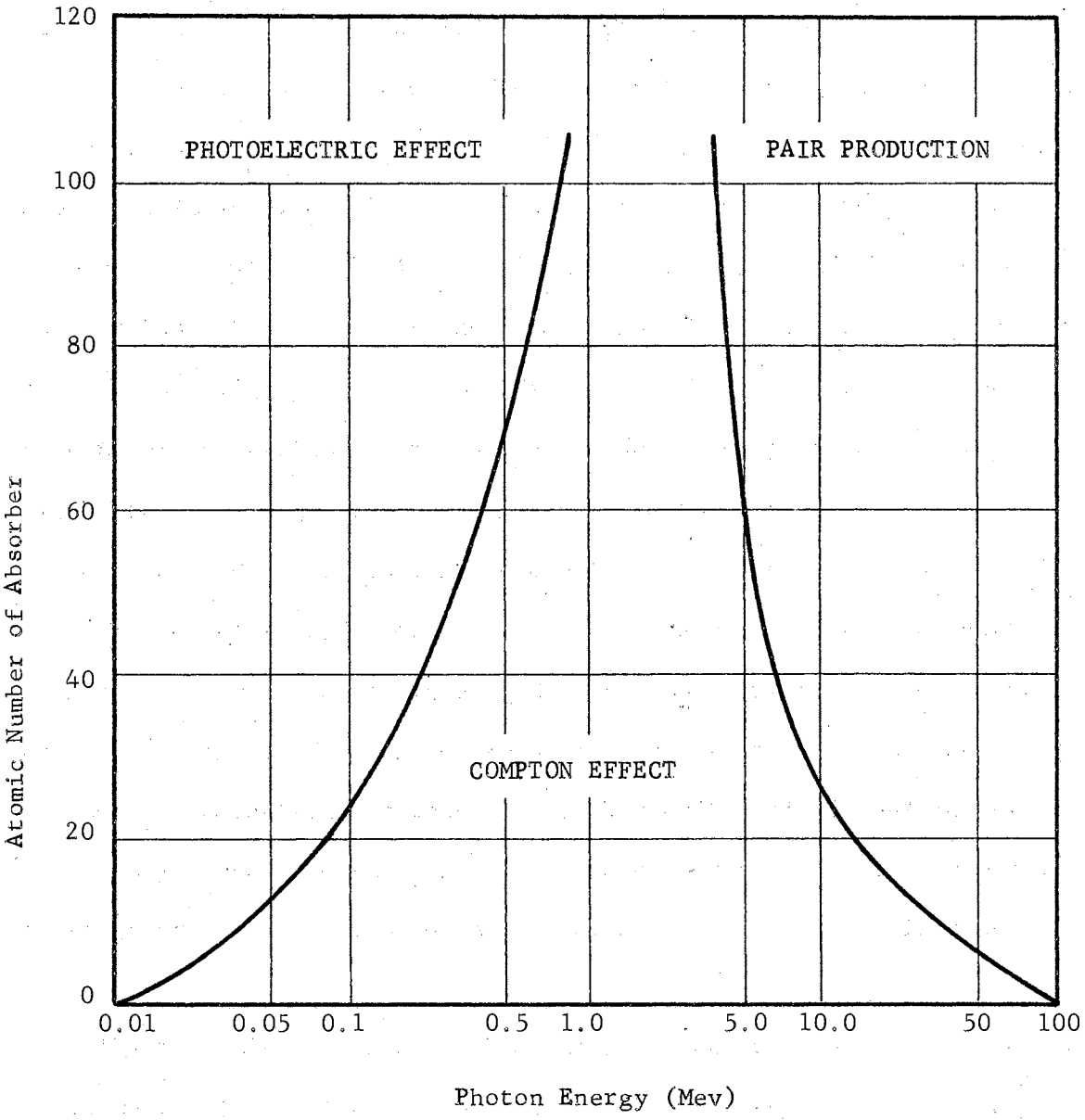


Figure 15. Energy Region Over Which the Three Processes Predominate as a Function of Atomic Number and Photon Energy

many chemical bonds which initiates chemical reactions. For example, $10^5$ cal/mole represents the order of magnitude of the activation energy or free energy change associated with many reactions. This value corresponds to approximately $10^5/6.02 \times 10^{23} = 1.6 \times 10^{-19}$ cal/molecule or about 4 ev/molecule. Since a photon energy of 4 ev corresponds to wavelength of about 3000 Å, irradiation by that part of the spectrum shorter than 3000 Å will produce reactions. The relatively high energy per quantum, high absorption coefficient of materials, and the intensity of ultraviolet radiation in space can, therefore, produce a profound effect on certain materials. Organic polymers, because of the dependence of their bulk physical properties on molecular weight and the integrity of their skeleton of carbon to carbon bonds or other covalent linkages, are more susceptible to degradation than metals, ceramics, and inorganic compounds which are held together primarily by the stronger coulombic interactions between atoms. The effect of ultraviolet radiation on structural metals is negligible except for a static change that is produced by the removal of electrons by the photo-electric effect (22).

The predominant types of chemical reactions taking place in polymeric materials exposed to exciting or ionizing radiation are cross linking and chain scission. Both processes are induced by free radical formation and interaction and result in structural changes within or between the adjacent polymer chains. Chain scission causes weight loss and induced porosity of the material. Cross linking may be actually beneficial depending on the material, but in general, excessive cross linking of elastomers is harmful because of the loss of flexibility.

In the case of rigid plastics, cross linking produces cracking and crazing which results from internal stress formation (23).

Infrared and visible radiation does not possess sufficient energy per quantum to break chemical bonds in ordinary reactions. The principal effect of this radiation is to increase thermal agitation (vibration and translation of atoms and molecules). However, many reactions initiated by the higher energy ultraviolet photons will proceed at a greater rate because of higher temperature (23).

Particle radiation damage depends on the intensity, type and energy of the irradiating particles and the material exposed. In a study of radiation effects on materials, the radiation particles of greatest interest are electrons, protons, and neutrons which possess high penetrating power. Low-energy particles, because of their shorter penetration range, distribute the ionization over a smaller volume of material and therefore cause more intense radiation damage near the surface than an equal flux of high-energy particles (23).

Penetrating radiation will generally affect materials by changing their chemical, electrical, or mechanical properties through one or more of the following mechanisms:

a. ionization,

b. dislocation of the crystalline structure, lattice displacements, by electron or ion collision,

c. contamination by absorption of the bombarding particles,

d. nuclear-reaction transmutations in the absorbing material.

Typical threshold dosages of radiation to initiate damage are shown in Figure 16 (24).

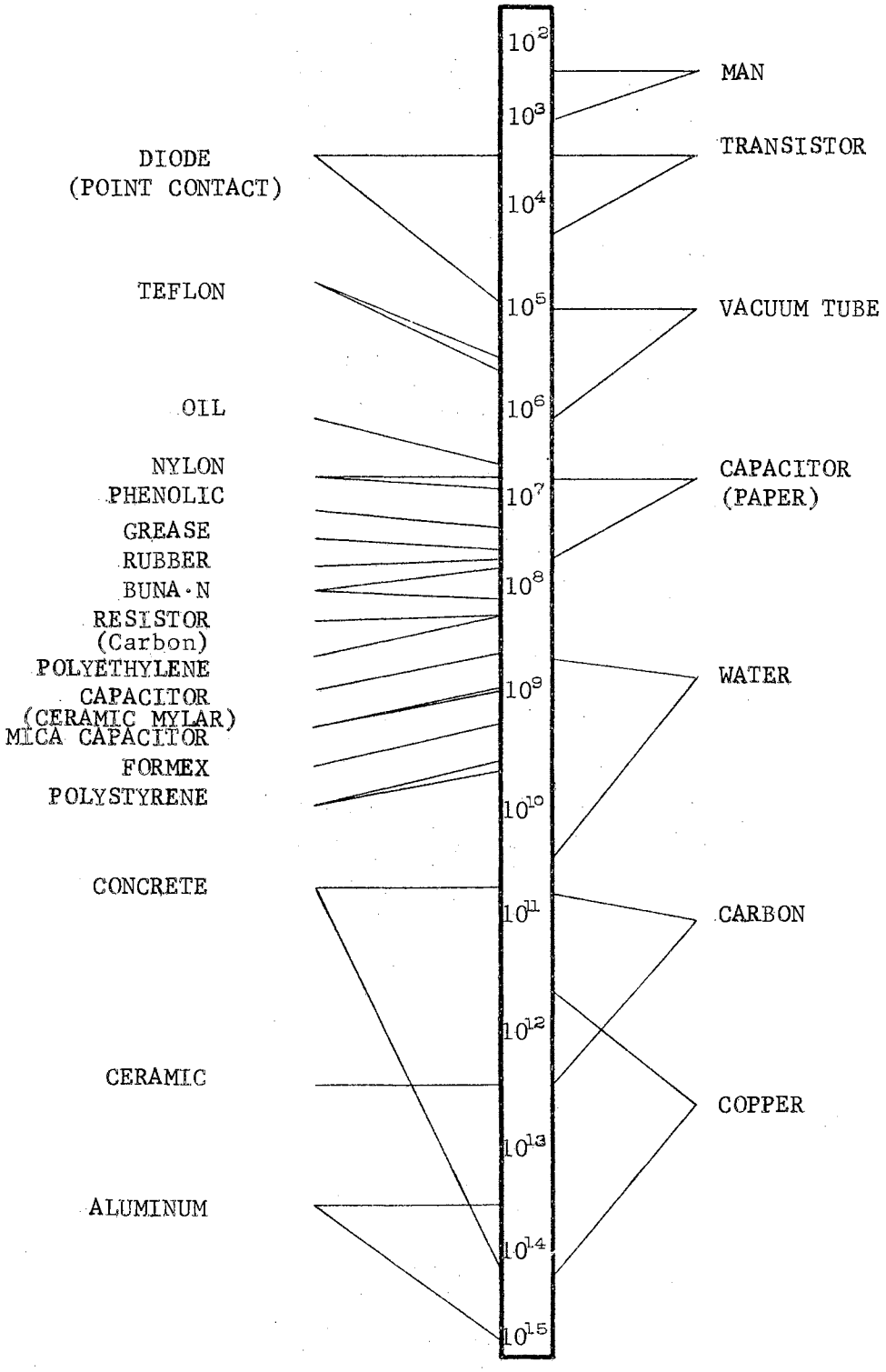


Figure 16. Radiation Threshold Dosages to Initiate Damage Threshold Scale in Rads; One Rad = 100 ergs/gm. (Ref. 24)

The chemical and physical effects produced when radiation interacts with matter are a direct consequence of the radiation energy absorption. These radiation-produced effects may be permanent or transient; that is, the effects may disappear after bombardment ceases. Permanent effects are most likely caused by competing rates of damage and repair which are dependent on the dose rate. Transient effects are predominantly electric in nature and affect the performance of the material while being bombarded. An annealing process, a function of temperature, removes transient effects and returns the material to its original condition before exposure. Changes which anneal out at room temperatures in a time interval of minutes or hours are called relaxation effects.

# CHAPTER V

## LITERATURE SURVEY

### Radiation Effects on Thermal Coatings

The over-all thermal-control system, as discussed in Chapter II, is designed for the purpose of maintaining the proper temperature limits of the system while operating in a space environment. Additives such as pigments, plasticizers, and other coating ingredients, as well as the type of surface on which the coating is applied, influence the radiation stability of the coating. The parameters that determine radiation reflectance include the ratio of indices of refraction of pigment and vehicle, pigment-vehicle ratio, and pigment particle size (25). Coatings which are highly pigmented are generally more resistant to radiation than similar class coatings containing lesser amounts of pigments. The resistance of organic coatings to radiation can be predicted to some degree from data available on polymers and plastics. However, because of the complicating factors introduced by pigments, plasticizers, and other coating ingredients, exact predictions of a coating's resistance to radiation can be obtained only by experimental testing. Detailed discussion of the problems involved in deriving quantitative data regarding the space environment damage on materials is presented in Chapter VI.

The environmental testing of thermal-control coatings is complicated by such variables as coating thickness and sample temperature during the testing, both of which may significantly influence the degree of change in the solar absorptance during exposure to radiation. The influence of sample temperature is particularly significant in accelerated testing where the higher intensities can produce an increase in temperature unless specifically compensated by effective cooling. Figure 17 shows the influence of ultraviolet on spectral absorptance of Alodine 401 for sample temperatures at 25° C and 70° C (26). This same reference presents results on the ultraviolet stability of other thermal-control coatings as well as the effects of gamma radiation on solar absorptance of several selected white paint-type coatings. Results of the investigation show that the gamma radiation, used to simulate the effects of electron and proton radiation, generally change the solar absorptance less than ultraviolet radiation when compared on the basis of equivalent time exposures in space. Comparative effect of ultraviolet and vacuum exposure on five selected coatings is shown in Figure 18. The titanium dioxide-silicone, zinc oxide and alodine 401 shows a remarkable resistance to ultraviolet radiation after an equivalent 300 sun hours when compared to titanium dioxide-epoxy and antimony oxide-potassium silicate. The important thing to note in this figure is the amount of damage experienced by the semiconductor pigment, $TiO_2$ with two different vehicles: epoxy and silicone. However, not knowing the pigment to vehicle ratio for the two coatings, it cannot be postulated that the degradation difference was due entirely to the vehicle.

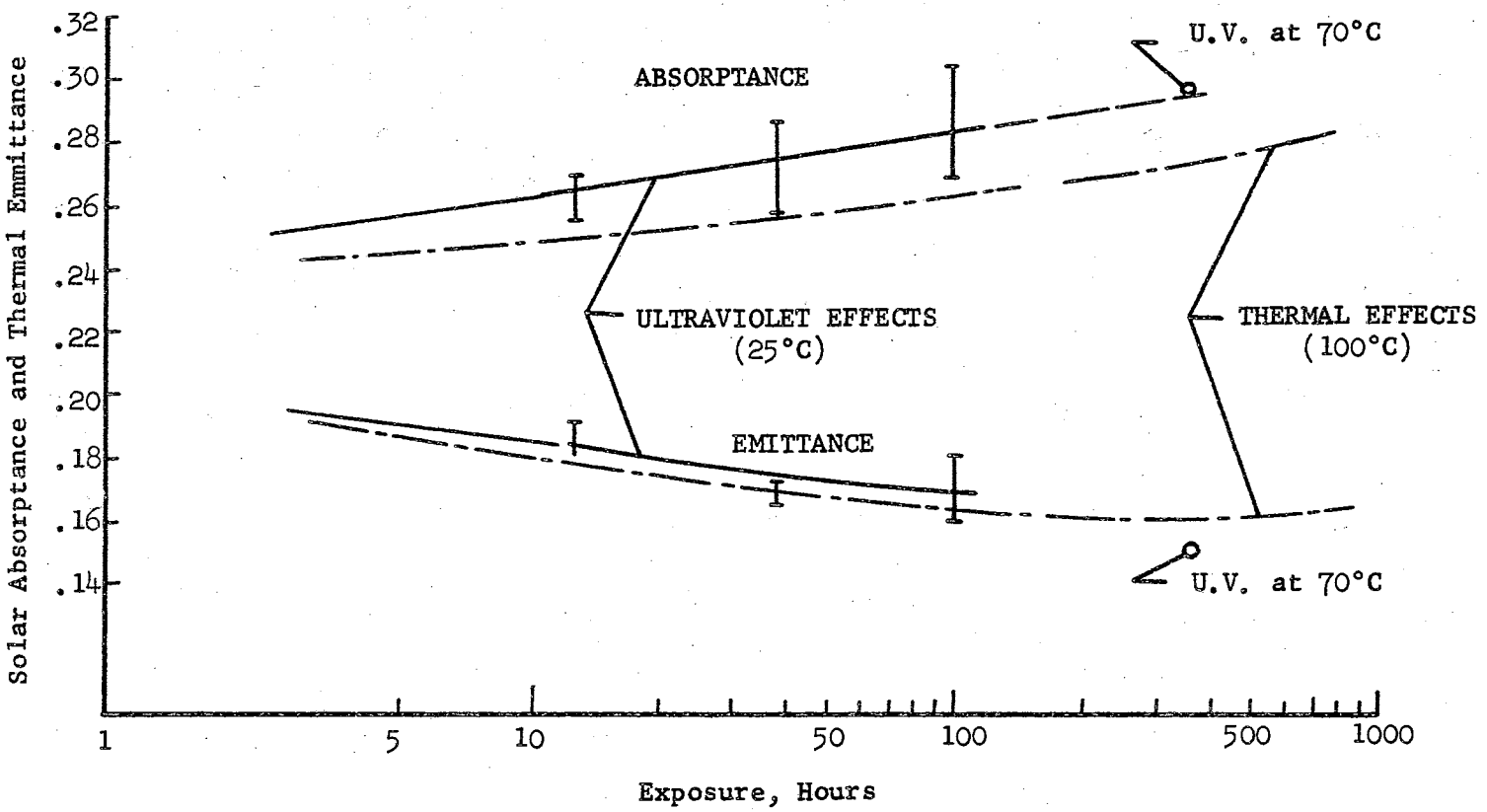


Figure 17. Thermal and Ultraviolet Effects on Solar Absorptance and Thermal Emittance of Alodine 401 (Ref. 26)

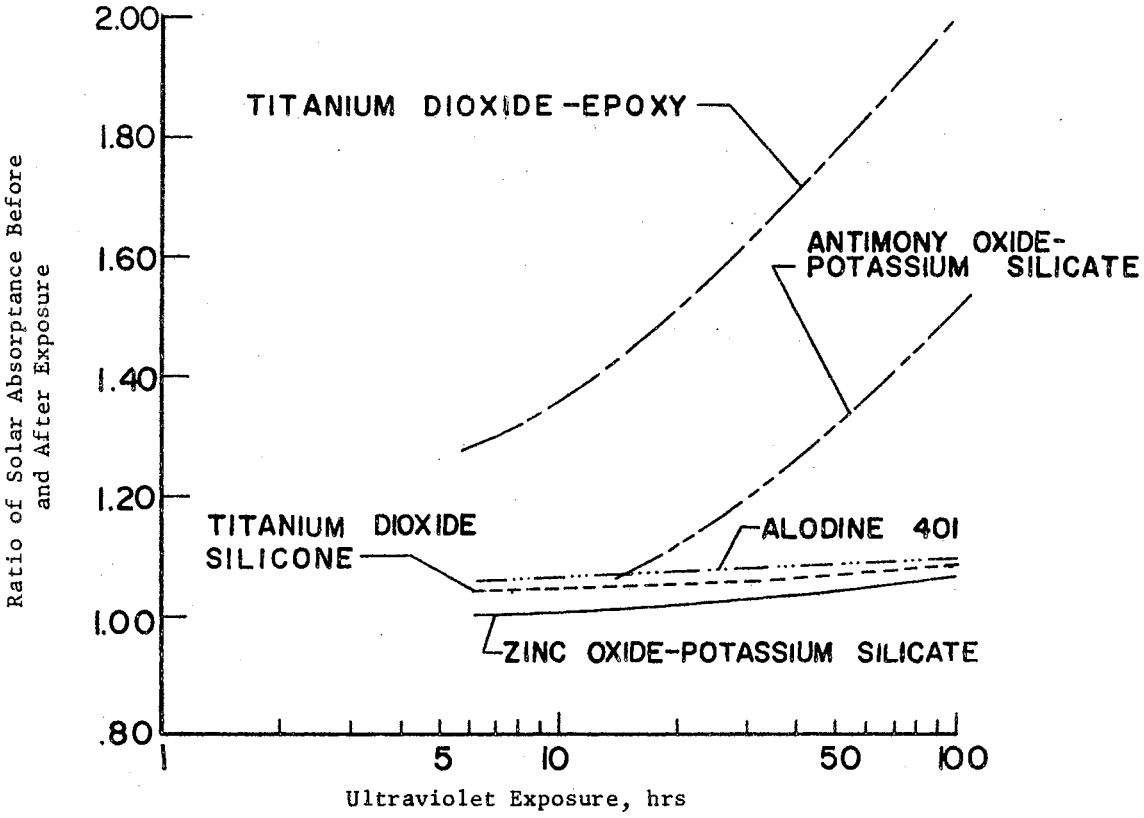


Figure 18. Comparative Effect of Ultraviolet and Vacuum Exposure on Five Selected Coatings; Average Solar Intensity-3 Solar Constants and Average Pressure $1 \times 10^{-6}$ torr (Ref. 26).

An extensive investigation has been undertaken by Zerlaut and Kaye (27) for the purpose of developing stable thermal-control coatings with the lowest possible ratio of solar absorptance to infrared emittance. The investigators conclude that zinc titanate-potassium is relatively stable with regard to vacuum-ultraviolet irradiation. A similar investigation is being undertaken by Zerlaut et al, (28), (29), (30), to develop stable white thermal-control coatings. Various inorganic pigments and organic and inorganic vehicles have been tested under vacuum-ultraviolet irradiation. To reduce the complexity of the problems involved, pigments and paint vehicles were exposed individually to ultraviolet radiation in vacuum. Results of these preliminary tests were used for subsequent choice of potentially stable paint formulations. Good stability and low degradation was exhibited by zinc oxide type pigments. The references contain an abundance of information and data associated with the ultraviolet radiation characteristics of the coatings and problems related to the development of stable coatings.

Reference 31 is a technology survey which reviews major NASA research in the field of inorganic protective coatings for thermal-protection and lubrication purposes. The report was prepared by the Denver Research Institute from data supplied by NASA research facilities. It is a well written comprehensive review of inorganic coatings.

Miller and Campbell (32) conducted a series of tests with low energy protons on several thermal-control paints. The samples were irradiated at four specific energies between 50 and 400 kev. The amount of degradation, which was calculated as a decrease in spectral

reflectance in the 0.4 to 0.433 micron region for each material, was found to be nearly linear with absorbed energy. The data indicated that equal numbers of higher energy protons would produce a greater change in solar absorption than protons of lower energy. In the range of fluxes investigated ($1 \times 10^{10}$ to $1 \times 10^{12}$ protons/cm$^2$-sec), the damage was found to be nearly independent of flux effects. Figure 19 shows the effect of proton irradiation on changes in reflectance of zinc oxide-methyl silicone paint, for proton energy of 200 kev and a flux of $2.0 \times 10^{11}$ p/cm$^2$-sec.

Gillette et al (33) study the effects of protons and alpha particles on thermal and solar concentrator coatings. The particle energies used in the tests were 1 to 9 kev and 2.5 Mev protons, and 2 to 16 kev and 5.0 Mev alpha particles. Hydrogen and helium were used to produce protons and alpha particles, respectively. The test samples included: (1) barrier-layer anodic-coated aluminum, (2) vapor-deposited aluminum on an aluminum substrate, (3) chemcially brightened aluminum, (4) zinc oxide/LTV-62 paint, and (5) zinc oxide/potassium silicate paint. Results of the study showed that the solar reflectance or absorptance of the barrier-layer anodic-coated aluminum reflective surfaces is not expected to change for solar charged-particle irradiation. The solar absorptances of the zinc oxide/potassium silicate (Z-93) and zinc oxide/LTV-602 (S-13) spacecraft coatings will increase substantially due to charged-particle irradiation.

After irradiation with kev-energy protons, vapor-deposited aluminum surfaces became almost completely covered with small blisters (about 0.2 micron in diameter) and large blisters (0.6 to 3 microns in

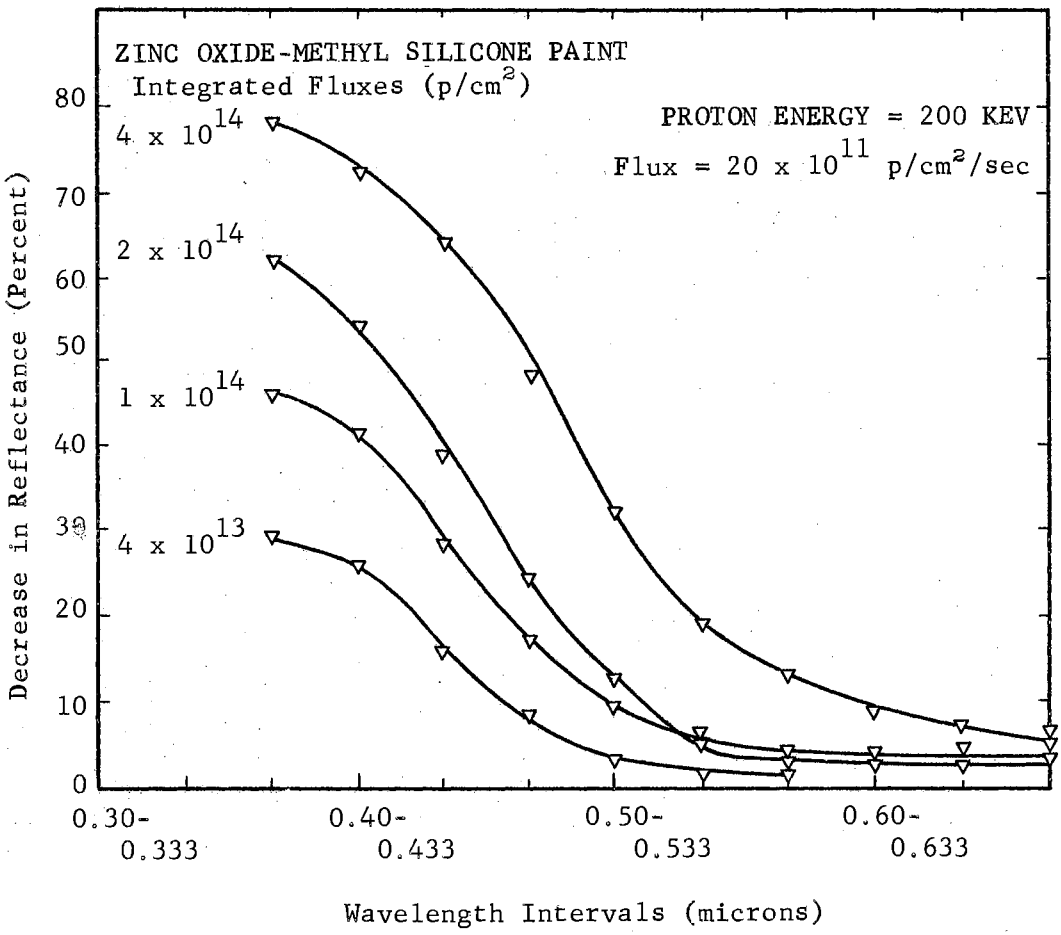


Figure 19. Effect of Proton Irradiation on Changes in Reflectance of Zinc Oxide-Methyl Silicone Paint (Ref. 32)

diameter). The thickness of the vapor-deposited aluminum film was approximately 1 micron and the estimated range of penetration of the 7.4 kev protons was approximately 0.2 micron. Electron photomicrographs of a cross section of a blistered surface indicated that the blister depth was no greater than 0.2 micron which was comparable to the proton penetration range (33).

Jorgenson (34) subjected several thermal-control surfaces to a simulated solar-wind bombardment in hydrogen and helium plasmas. The thermal-control materials tested were ZnO pigment with methyl silicone binder (S-13) and ZnO pigment with potassium silicate binder (Z-93). Results show that the thermal-control materials are vulnerable to damage by the bombardment of hydrogen (to simulate protons) and by helium (to simulate $\alpha$-particles). The experiments show that the binder is far more susceptible than the pigment to damage. Most of the damage caused by the bombardment appeared to be due to broken and rearranged bonds or some other similar structure change. The extent of the damage was related to the depth of penetration. Amount of damage to the thermal-control materials was energy dependent; the higher the energy of the bombarding ions, the greater the damage. Figure 20 shows the spectral change in absorptance for Z-93 thermal-control coating after bombardment by two doses of hydrogen ions.

Breuch, Doulgas and Vance (35) recently conducted a series of radiation effects tests on thermal-control materials. The materials were subjected to a combined environment of low density, ultraviolet radiation and high-energy electrons. Test materials were irradiated at various electron flux levels over specified temperature regions

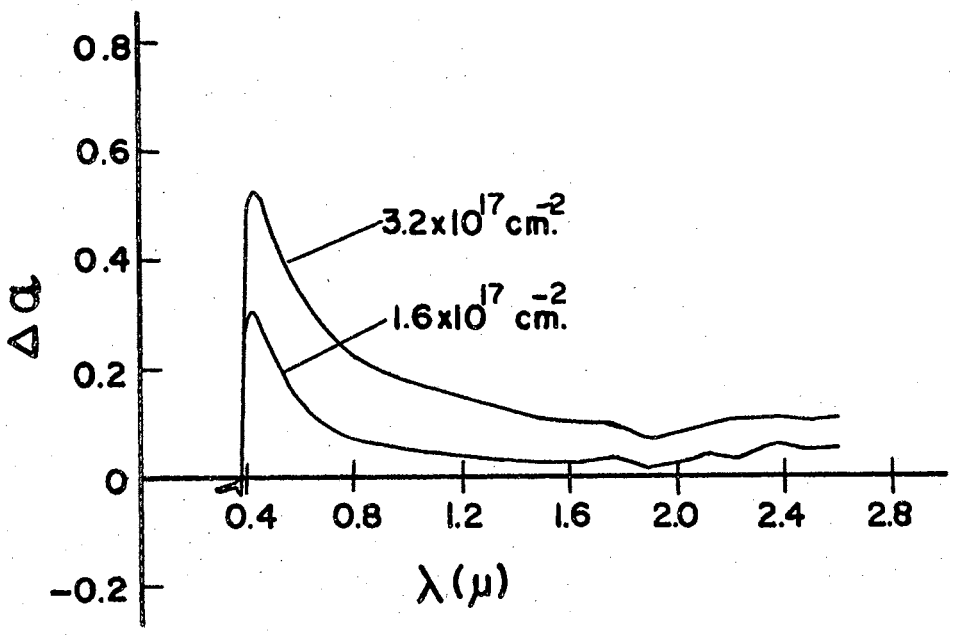


Figure 20. Spectral Change in Absorptance for Zinc Oxide-Potassium Silicate Paint after Bombardment of 500 ev Hydrogen Ions

with an incident electron energy of 0.80 Mev. The resulting optical damage (due to electrons only) was compared to similar data established by ultraviolet radiation exposure. For most of the materials tested, the spectral region of optical damage was different for the two environments. Electron irradiated materials showed an increase in absorption in the near-infrared and visible portion of the spectrum. The spectral curves for ultraviolet exposure showed an increase in the same regions and also indicated a shift to longer wavelengths of the apparent absorption band. Figure 21 shows the apparent absorption as a function of photon energy on White Kemacryl paint. Samples bombarded with electrons and then exposed to ultraviolet radiation differ in optical damage from

the superposition of damage induced by the separate environment. Figure 22 shows this relationship for White Kemacryl material.

From review of the literature one can conclude that the space environment, primarily the combination of low-density, temperature, electromagnetic radiation and particle radiation can produce property changes in space system materials that could be detrimental to the mission success. The photon and particle radiation environment will optically degrade thermal-control materials. The correlation of damage data presented in the literature is almost impossible because many of the test parameters are not well defined. Chapter VI will further discuss the correlation problem. A need exists for performing combined environmental testing with ultraviolet and particle radiation to evaluate synergistic and accelerated testing effects. Also, the fundamental degradation mechanism(s) as a function of radiation type, energy and flux should be thoroughly investigated.

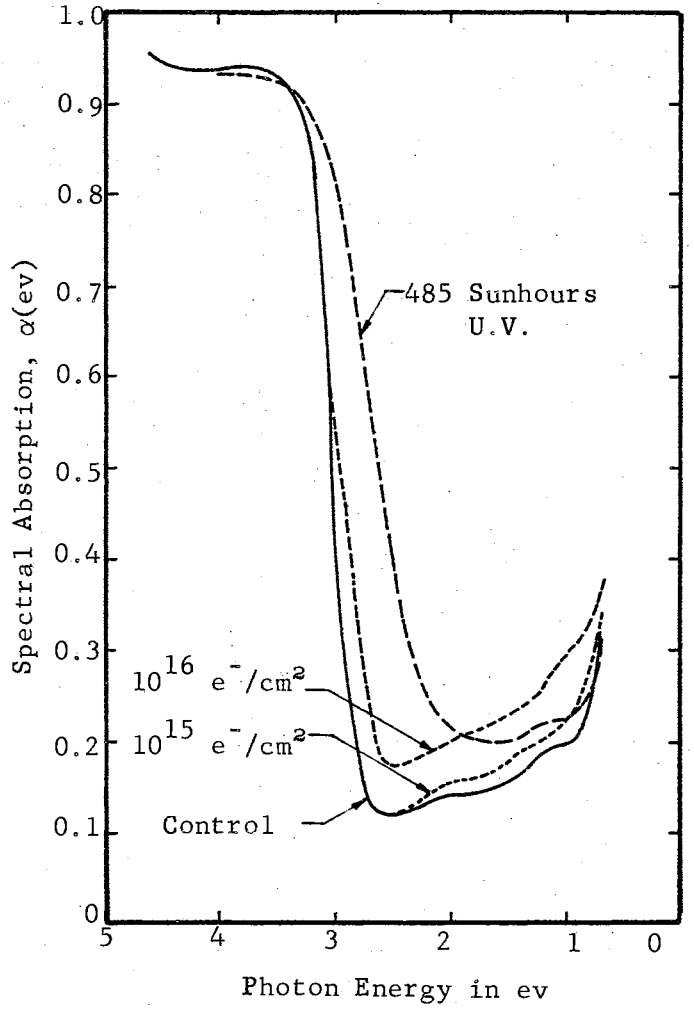


Figure 21. Spectral Curves for Electron-Only and Ultraviolet-Only Experiments on White Kemacryl Paint (Ref. 35)

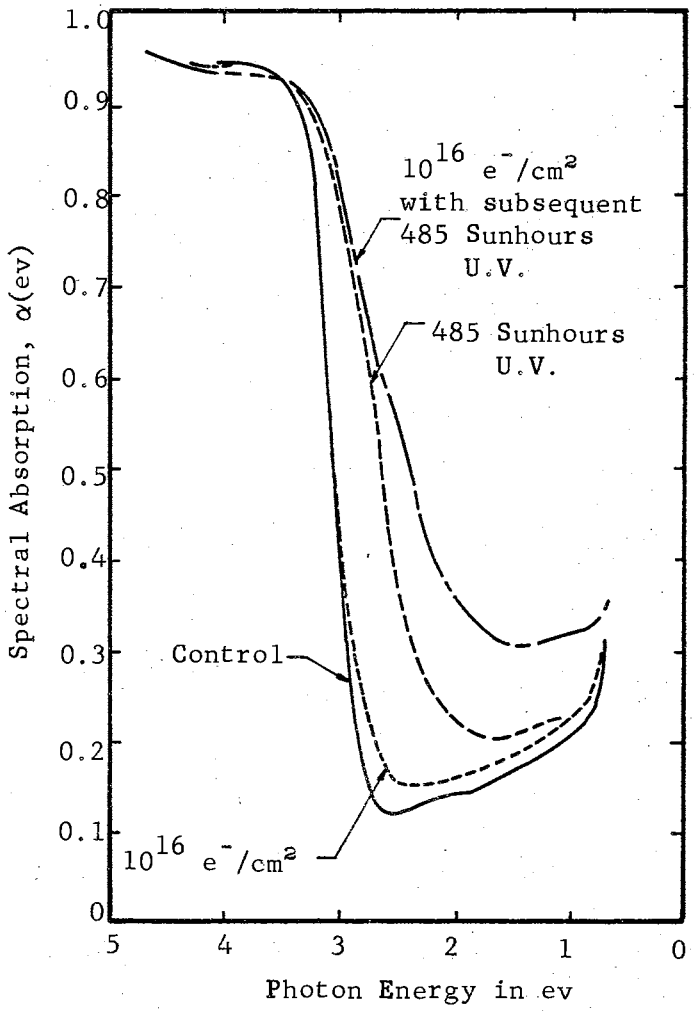


Figure 22. Spectral Curves of White Kemacryl Paint after Electron Bombardment with Subsequent Ultraviolet Radiation (Ref. 35)

# CHAPTER VI

## ANALYTICAL CONSIDERATIONS

The purpose of this chapter is to discuss briefly the problems associated with presenting quantitative data regarding the space-environment damage on materials. It will show why valid quantitative data on damage are not presently available and will indicate the need for experimental testing. The degree of simulation necessary for determining the damage threshold will be indicated where feasible, although the main interest in the research is directed toward the space environmental effects on thermal-control materials. The first part of the chapter will discuss the material problems in general. Particular emphasis will be directed toward thermal-control materials in the latter part of the chapter.

For the purpose of this chapter the space environmental parameters to be considered are low density, temperature and radiation. Although the discussion will consider each environment parameter separately, the synergistic parameter effects on the material properties will in most cases be different than the sum of property effects of individual parameters. An attempt will be made to point out this different where appropriate.

## Low Density

The low-density environment of space is usually specified in units of torr*. For space applications, the low density environment is considered as a region of free molecular flow, or Knudsen flow, where the mean free path of the gas becomes greater than the dimension of the system. The mean free path (D) of air at 300° K is approximately equal to (44):

$$D\ (cm) \cong \frac{5 \times 10^{-3}}{P\ (torr)} \qquad (6\text{-}1)$$

For example, if the pressure was $10^{-6}$ torr then D = 5000 cm (2000 inches).

In most cases the magnitude of the pressure (molecular density) associated with the low-density environment would be considered necessary for a particular environmental parameter to produce material damage. Thus, the degree and rate of damage could be enhanced by the magnitude of the molecular density.

Flux can be defined as the magnitude per unit of time per unit of area. The low-density environment of space most generally is not considered to be described in terms of flux. However, on the other hand, the flux of molecules (molecular flux) impinging on a surface is a function of the environment pressure. Molecular flux can be theoretically calculated by the use of distribution laws and kinetic theory. The kinetic theory expression for the number of

---

*Measurements of pressure are usually expressed in torr units in honor of Torricelli, who invented the barometer. One torr is the pressure exerted by a column of mercury one millimeter high at 0° C, 45° latitude at sea level.

molecules of a gas that strike a unit area per unit time, F, is (4):

$$F = 1/4\ (N\ V_a) \tag{6-2}$$

where $N$ is the number of molecules per unit volume of gas and $V_a$ is the average velocity of the molecules from kinetic theory. The definition of $N$ is:

$$N = 9.656 \times 10^{18}\ \frac{P}{T} \tag{6-3}$$

where $P$ is pressure in torr and $T$ is temperature ($^{\circ}K$). The definition of $V_a$ is:

$$V_a = \left(\frac{8\ R_o T}{\pi M}\right)^{\frac{1}{2}} \tag{6-4}$$

where $R_o$ is the universal gas constant and $M$ is the molecular weight. Substituting for $N$ and $V_a$ in the Meyer expression (equation 6-2) the flux, F, of molecules impinging on a surface becomes,

$$F = 3.513 \times 10^{22}\ \frac{P(\text{torr})}{\sqrt{MT}}\ \text{cm}^{-2}\ \text{sec}^{-1} \tag{6-5}$$

For example, for oxygen at $300^{\circ}$ K ($27^{\circ}$ C) and pressure of $10^{-6}$ torr, $F = 3.57 \times 10^{14}$ collisions per $cm^2$ per sec. If each oxygen molecule which hits the surface adhered to it, the surface would be covered with a monolayer of oxygen in about one second. Therefore, pressure, when defined in terms of density in molecular flow, can be considered in this light to be described in terms of flux. This could be very important when the mechanism for material damage depends on the surface interface.

The two most important effects of low density on materials are sublimation or evaporation and loss of surface film. These losses

can be calculated by using the Langmiur equation (39)

$$W = \frac{P}{17.14} \sqrt{\frac{M}{T}} \qquad (6\text{-}6)$$

W = rate of evaporation or sublimation, $gm/cm^2$-sec

P = P(T) = vapor pressure of the material, torr.

M = molecular weight of the material in the gas phase.

T = temperature, °K.

which dates back to 1913 and was developed through the use of the Maxwell-Boltzmann Distribution Laws and Meyer's expression for the rate of evaporation, or condensation, at equilibrium. For most elements of interest this type of loss rate can be calculated, since the vapor pressures and molecular weights are well established.

In the case of alloys, loss by evaporation is a complicated process, which involves the loss of the more volatile constituents through the solid alloy. The evaporation process includes diffusion of the volatile elements from the basic material, dissociation and diffusion through the oxide surface films and diffusion of the oxide films. Each process, diffusion and dissociation, is also a function of temperature (40).

The rate of loss calculations of inorganic compounds are very difficult, because the loss may occur by several mechanisms. Molecules of the compound may sublime. Sublimation vapor pressure data can usually be found in the literature or derived for a particular temperature from the Clausius-Clapyron equation of thermodynamics. With a known vapor pressure the loss rate can be calculated by equation (6-6). Many inorganic compounds decompose into more volatile compounds under a

low-density environment. The calculation of the rate of loss, which is enhanced by decomposition into elements or simpler compounds, can be accomplished by knowing the decomposition pressure (41). For example,

$$MoS_2 \text{ (solid)} \rightarrow Mo \text{ (solid)} + S_2 \text{ (gas)}$$

$$MgO \text{ (solid)} \rightarrow Mg \text{ (gas)} + 1/2\ O_2 \text{ (gas)},$$

the loss rate can be calculated from the equilibrium constant, K, for the reaction which can be expressed in terms of the partial pressures of the gaseous constituents. With a known K, the decomposition pressure can then be computed and the loss rate derived through equation (6-6). The equilibrium constant for many reactions can be obtained from the tabulated free energy values for the compound and its decomposition products by the free energy relation (42).

$$\Delta F = -RT \ln K \qquad (6\text{-}7)$$

$\Delta F$ = change in free energy

R = universal gas constant

T = temperature

K = equilibrium constant

## Temperature

Temperature is another environmental parameter that must be considered in evaluating material damage. Space systems are designed for operation within a specified temperature range. The specified temperature range depends on the materials of the individual components of the system. Again, the synergistic effects play an important role

in over-all damage mechanism. Therefore, even though the effects of temperature alone on material damage can realistically be determined, only a qualitative determination of damage can be made because of the functional inter-relationship of temperature and the other environmental parameters.

## Radiation

Theoretical calculations for estimating radiation damage become very difficult, even when the radiation mechanism that is causing the damage is known. Unfortunately, in most cases the particular mechanism is unknown. The mechanism by which electromagnetic radiation interacts with materials is a complex function of the energy of the radiation and the atomic number of the material. Material damage due to photon interaction is the result of three types: the photoelectric effect, the Compton process, and pair production. In the region of interest, from a few tenths Mev to several Mev, the Compton effect predominates in the energy-transfer mechanism.

Particle and electromagnetic radiation damage depends on the intensity, type and energy of the irradiating particles and the exposed material. Protons have a lower energy threshold for producing atomic displacement than do either electrons or photons. Electrons and photons have a lower energy threshold for producing ionization than protons. Therefore, protons will be more damaging in materials susceptible to atomic displacement (43).

The type of radiation will in general determine the mechanisms for material damage. However, this does not mean that ionization and

atomic displacement can not occur simultaneously. Even if the radiation damaging mechanism(s) is (are) known it becomes necessary to know the mass absorption coefficient, ionization energy, secondary damage mechanism and other characteristics of both the radiation process and the absorber. An accurate determination of damage requires the knowledge of the damage mechanism for the various types of radiation. In selected materials it is possible to compute qualitative estimates of damage for the various types of radiation.

In discussing intensity, both the magnitude and the flux of the radiation environmental parameter must be considered. For an example, particle radiation generally has energies of the order of a million electron volts which are very high compared to the bonding energies and excitation or ionization potentials of chemical systems (4 ev to 25 ev), but the average flux of these particles could be so small that the total energy flux (magnitude) is less than that of the electromagnetic ultraviolet radiation.

The magnitude of radiation exposure is generally expressed as the "dose". The "dose" is defined as the magnitude of the radiation energy to which the material was subjected. The "absorbed dose" is described in terms of energy actually absorbed in the material. The energy absorbed by the material depends on the type of the radiation field (photons, protons, electrons, or mixed) and the energy distribution of the field components. Although the equal energy-equal damage concept may hold reasonably well for selected materials, it does not hold for the majority of materials. In other words, some materials are damaged by any energy transfer from the radiation field;

other materials are permanently damaged only when the energy transfer mechanism involves the nuclei of the atoms of the material, as in displacement processes. Therefore, although the magnitude of the energy absorbed is known, it is not sufficient to convey all the information necessary to estimate the damage.

The radiation environmental parameter is most commonly described in terms of flux. The degree of damage to materials could be a function of the radiation energy flux. Most quantitative data reported in the literature does not consider the energy flux but only the total dosage required for material damage. However, for most materials there could exist a competing mechanism within the material that is directly related to the energy flux. It is possible, for selected radiation energy fluxes, that the material could possess a self-annealing or repairing property that would prevent any measurable degradation. To estimate the anticipated damage, the flux dependence of the material along with total expected dosage must be considered. Since, for most materials, this flux dependence is not known it is very difficult to make damage estimates.

Energy is a parameter of the radiation environment which refers to the energy of the electrons, protons, and photons. The mechanism of radiation interaction with the material is the most important influence in the over-all determination of degradation. There are two principal areas in which radiation exerts its influence. One is the area of threshold interaction and the other is the absorption characteristics of the material. Ionization and atomic displacement not only vary with the particle type but are also functions of the

energy level of the particle. The energy levels necessary for ionization are well known for most materials. The energy level required to cause atomic displacement in a particular material may be calculated explicitly (45). The problem in estimating material damage is that usually both ionization and atomic displacement can occur simultaneously and the amount of energy flux devoted to each is known only qualitatively.

Absorption characteristics of materials are functions of energy and the type of particle (45). Unfortunately, for many of the materials having space applications, the absorption characteristics are unknown for the various types of particles which make up the space environment and can be determined only by experimental testing. The necessary data required to estimate damage from the interaction thresholds and the absorption characteristics of the material are very limited. For most space applicable materials, the data are not available.

The most important factor influencing damage to materials is the material itself. As discussed in the preceding sections, radiation damage to materials occurs primarily by ionization and the atomic displacement processes. Average ionization energy, I, has been the subject of theoretical study by many investigators, but realistic values for most materials are always obtained from experiment. Baker and Segre (46, 47) measured the first four values in the table below and the other values were derived by extrapolation. The table shows a marked relationship between atomic number of the materials and the ionization energy.

TABLE VI

IONIZATION ENERGIES FOR MATERIALS

| MATERIAL | ATOMIC NO. | I(ev) |
|---|---|---|
| H | 1 | 15.6 |
| C | 6 | 76.5 |
| Al | 13 | 150.0 |
| Air | -- | 80.5 |
| N | 7 | 88.0 |
| O | 8 | 98.0 |
| $H_2O$ | -- | 68.0 |
| Fe | 26 | 400.0 |
| Pb | 82 | 1100.0 |

## Penetration Range

The penetration range for charged particles at various energy levels for aluminum are listed in the following table (49). For alpha particles, protons, and electrons the penetration range is that thickness required to reduce the intensity essentially to zero. For gamma rays and neutrons, the thickness is that required to reduce the intensity to half the incident value.

The penetrating power of particulate radiation is not theoretically understood. Although the physical basis of the penetrating phenomena has been well understood for a period of time (48), discrepancies between theory and experiment can be ascribed to the mathematical

TABLE VII

PENETRATING POWER OF CHARGED PARTICLES IN ALUMINUM

| RADIATION PARTICLES | ENERGY (Mev) | PENETRATING RANGE (inches) |
|---|---|---|
| Alpha | 1 | 0.001 |
| | 10 | 0.004 |
| | 100 | 0.14 |
| Proton | 1 | 0.005 |
| | 10 | 0.014 |
| | 100 | 0.75 |
| | 300 | 7.9 |
| Electrons | 1 | 0.06 |
| | 3 | 0.21 |
| Gamma Ray | 1 | 1.7 |
| | 5 | 3.7 |
| Neutrons | 2 | 3.5 |

problems involved in applying an accurate collision theory. If one assumes that charged particles, in passing through matter, will lose their kinetic energy predominantly through inelastic collisions with atomic electrons, which is considered appropriate for proton penetration, the energy loss per unit path length can be calculated from the following expression (48):

$$-\frac{dE}{dx} = \frac{4\pi e^4 z^2}{mv^2} N\left\{ Z\left[ \ln \frac{2mv^2}{I} - \ln (1 - \beta^2) - \beta^2 \right] - \sum C_1 \right\} \qquad (6\text{-}8)$$

E = particle energy

x = particle path length

$z$ = atomic number of the incident particle

$e$ = charge of the incident particle

$v$ = particle velocity

$m$ = particle rest mass

$N$ = number of stopping atoms per cubic centimeter of material

$Z$ = atomic number of the stopping material

$I$ = average excitation potential of an electron of the absorbing material

$\beta$ = relativistic correction term equal to the particle velocity/velocity of light (v/c)

$C_i$ = correction term for binding effects of the ith shell

The term (-dE/dx) is also known as the stopping power of the absorbing material. The mass stopping power can be expressed as (-dE/dx) x $(1/\rho)$ which is the energy loss per gram per $cm^2$ of absorbing material and will be denoted as $_m(-dE/dx)$. The reciprocal of the stopping power (RSP) is equal to the distance traveled per unit change of energy (-dx/dE). Integrating over the entire energy range gives the mean distance traveled by the particle before it comes to rest.

$$(RSP)_{mean} = \int_0^E {}_m\left(-\frac{dx}{dE}\right) dE \qquad (6\text{-}9)$$

Since (-dx/dE) tends to become infinite as E approaches zero, the usual practice is to integrate between limits.

To obtain range-energy relationship for materials, three approaches can be considered: (1) theoretical calculation of RSP, (2) experimental measurement of (- dE/dx) and calculation of RSP,

(3) direct measurement of range-energy relationship (49). Because of the lack of data pertinent to space materials and the lack of validity of the theoretical equations for low-energy levels due to inner electrons moving at high velocities compared to the incident particle, it is necessary to establish an empirical range-energy relationship. The procedure in this study was to use experimental range data for Al and $O_2$ and establish an empirical relationship for the materials of interest.

For nonrelativistic protons, the relative mass stopping power of two materials is given by the following ratio (49):

$$\frac{{}_m(-\,dE/dx)_1}{{}_m(-dE/dx)_2} = \frac{Z_1 A_2\,(\ln[2\,mv^2] - \ln I_1)}{Z_2 A_1\,(\ln[2\,mv^2] - \ln I_2)} \qquad (6\text{-}10)$$

where Z/A represent the number of electrons per gram in the absorbing material. The binding effects are neglected in this expression. In order to calculate the range-energy relationship in a compound, for example $TiO_2$, it is necessary to assume the energy loss of the compound was proportional to the fraction by weight of each element in the compound:

$${}_m(-\frac{dE}{dx})_{TiO_2} = (\%\ Ti)\ {}_m(-\frac{dE}{dx})_{Ti} + (\%\ O_2)\ {}_m(-\frac{dE}{dx})_{O_2} \qquad (6\text{-}11)$$

By the use of equations (6-10) and (6-11) and the availability of range data for Al and $O_2$ an estimated range-energy relationship can be computed for thermal-control materials. The stopping power for $TiO_2$ is shown in Table VIII. The mass experimental stopping powers for Al and $O_2$ were taken from Allison and Warshaw (50). The mass

TABLE VIII

STOPPING POWER FOR PROTONS IN MATERIALS

| Proton Energy (kev) | m(dE/dx) (kev-cm$^2$-mg$^{-1}$) | | | |
|---|---|---|---|---|
| | $Al$ (1) | Ti | $O_2$ (1) | $TiO_2$ |
| 20 | 405 | 339 | 420 | 405 |
| 40 | 412 | 349 | 572 | 511 |
| 60 | 435 | 371 | 636 | 563 |
| 80 | 434 | 372 | 644 | 569 |
| 100 | 416 | 358 | 646 | 566 |
| 150 | 366 | 317 | 612 | 531 |
| 200 | 334 | 289 | 552 | 479 |
| 250 | 314 | 273 | 498 | 437 |
| 300 | 293 | 255 | 450 | 396 |
| 350 | 279 | 243 | 414 | 367 |
| 400 | 268 | 234 | 384 | 342 |
| 450 | 258 | 225 | 356 | 320 |
| 500 | 250 | 219 | 332 | 301 |
| 550 | 241 | 212 | 316 | 287 |
| 600 | 233 | 204 | 298 | 272 |

(1) Experimental stopping powers, taken from Ref. 50

stopping power for Ti was calculated from equation (6-10) and the mass stopping powers for the compound, $TiO_2$, was calculated from equation (6-11).

Range-energy data for the compounds were calculated by plotting reciprocal values of $_m(-\ dE/dx)$ versus energy and then extrapolating the curve to zero energy, and integrating graphically. Reciprocal stopping power versus proton energy for $TiO_2$ is shown in Figure 23, with the range-energy data shown in Table IX.

## Sputtering

Throughout the discussion on radiation damage to materials, consideration has been given only to the particular high-energy particles that were absorbed by the material. In applications where the material surface characteristic is important the effect of physical sputtering must be considered. Sputtering is the removal of atoms and molecules from a surface by the bombardment of high velocity impinging particles. The momentum-transfer theory is well accepted as the means of ejection for all energies. This theory assumes that the impinging particle transfers sufficient momentum to a surface-bound particle for the impacted particle to escape from the surface. In this theory it is not necessary to know the mechanism of transfer nor the energy of the bound particle. The energy required is thought to be either the energy of sublimation ($\sim$ 4 ev, depending on the material and the location of the atom in the crystal structure) or the displacement energy in radiation damage theory ($\sim$ 25 ev for most substances).

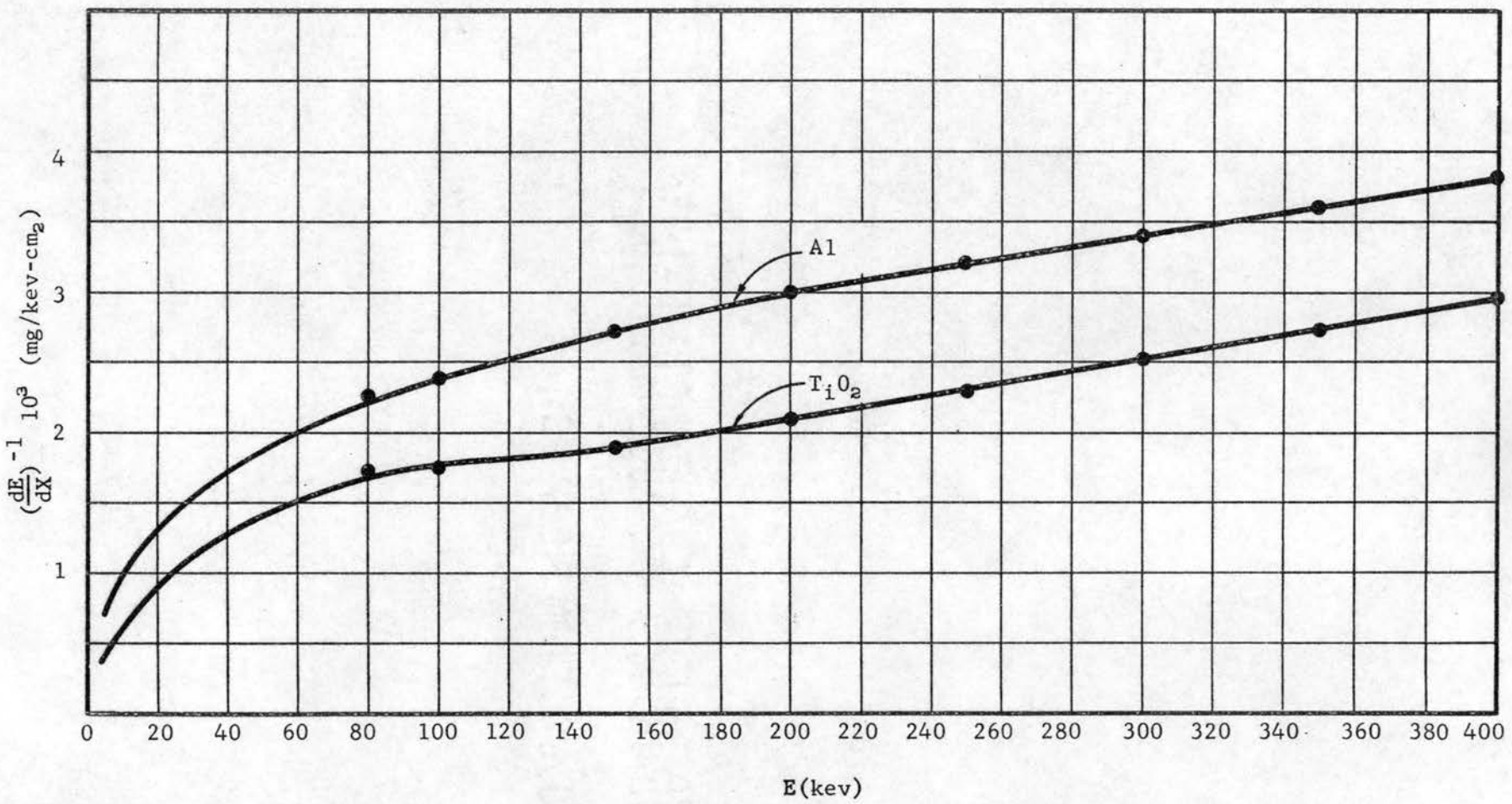


Figure 23. Reciprocal Stopping Power vs. Proton Energy

TABLE IX

RANGE-ENERGY DATA FOR PROTONS IN MATERIALS

| Proton Energy (kev) | R($mg/cm^2$) $TiO_2$ |
|---|---|
| 20 | .013* |
| 40 | .035* |
| 60 | .064* |
| 80 | .095 |
| 100 | .130 |
| 150 | .221 |
| 200 | .320 |
| 250 | .429 |
| 300 | .549 |
| 350 | .680 |
| 400 | .822 |
| 450 | .973 |
| 500 | 1.134 |
| 550 | 1.304 |
| 600 | 1.483 |

*Extrapolated Values

Several mechanisms have been proposed to explain the transfer of momentum from the ion (impinging particle) to the sputtered particle. None, however, can explain all observed facts. Redus (51) has analyzed many of these mechanisms and proposed the following properties for the yet to be found correct mechanism:

a. The scattering cross-section or the depth at which displacements result in sputtering must change drastically with energy and decrease beyond a specific range of energy. Sputtering yield (atoms out/ions in) varies greatly with energy, the minimum being less than $10^{-3}$ at a few tens of evs and the maximum being about 10 at approximately 10 kev.

b. The sputtering yield (atoms out/ions in) will depend on the lattice parameters. Preferential sputtering takes place in the direction of close-packed chains in single crystals.

c. The sputtering yield is a function of the angle of incidence of the ions, with minimum yield at normal incidence.

The validity of published data is often difficult to evaluate and it is often quite conflicting. Most of the published literature does not clearly define the true test conditions, thus leaving the reader only a choice of accepting or rejecting the data. Further experimental investigation is required to determine the effects of pressure, temperature and particle flux on sputtering yield.

Surface condition of the material, which is very important is a function of the environmental pressure. Contamination by absorption

and other surface films would tend to lower the yield. If the environmental pressure is high a large percentage of the sputtered atoms could return to the surface, lowering the yield.

High temperatures of the materials increase the rate of sublimation, which cannot be differentiated from sputtering. High temperatures would also assist in reducing the surface contamination.

The energy with which a particle strikes the space vehicle is given by half the product of the square of the relative velocity between the space vehicle and the particle and the mass of the particle. The thermal energy ($\pm$ 3/2 kT) is considered completely negligible since a particle at 2500° K has only a mean thermal energy of .321 ev. Assuming the threshold for low energy sputtering is based on the heat of sublimation and using the following empirical equation developed by Redus (51) from data by Baden, et al (52),

$$S = 10^{-4} (E - E_t)^2 \qquad (6\text{-}12)$$

S = sputtering yield (atoms out/ions in)

E = particle impact energy (ev)

$E_t$ = threshold energy (ev)

The sputtering yields for aluminum, $S_{Al}$, by oxygen and nitrogen bombardment are shown in Table X (values were doubled to account for angle of incidence).

The lower energy corresponds to orbital velocity and the higher energy value to escape velocity. If sputtering is caused by this type mechanism, then electrons would be expected to cause no sputtering yield. However, if sputtering is a form of radiation damage, or a

TABLE X

SPUTTERING YIELDS FOR ALUMINUM

| | E (ev) | $E_{t\ Al}$ (ev) | $S_{Al}$ |
|---|---|---|---|
| $O_2$ | 10.6 | 4.0 | $8.6 \times 10^{-3}$ |
| | 20.8 | 4.0 | $5.6 \times 10^{-2}$ |
| $N_2$ | 9.3 | 4.0 | $5.6 \times 10^{-3}$ |
| | 18.2 | 4.0 | $4.0 \times 10^{-2}$ |
| O | 5.3 | 4.3 | $2.2 \times 10^{-4}$ |
| | 10.4 | 4.3 | $7.5 \times 10^{-3}$ |
| N | 4.6 | 4.4 | $8.0 \times 10^{-6}$ |
| | 9.1 | 4.4 | $4.3 \times 10^{-3}$ |

similar mechanism, sputtering by electrons should start around 200 Kev. Sputtering yields from electrons were not available in the literature.

Sputtering rates from solar corpuscular radiation could cause serious problems because of the high densities and high energies of the ionized particles. For a quiet sun, we shall assume a density of 100 particles/$cm^3$ and a mean proton velocity of 500 km/sec; for an active sun, a density of $10^4$ particles/$cm^3$ and a velocity of 1500 km/sec, for a maximum period of $10^4$ sec. From this it can be computed that $2.5 \times 10^2$ and $3.9 \times 10^4$ Å of aluminum would be removed in a year by sputtering by solar corpuscular radiation.

From this discussion one can conclude that sputtering caused by particle bombardment should result in a damaging effect to most materials. The damage would be mostly that of surface roughness. For materials which are highly absorbent to the incoming particles, damage through

surface sputtering would be less pronounced. Highly penetrating particles should cause more damage through atomic displacement and ionization than by surface sputtering. High energy protons and heavier charged particles have sufficient mass to produce sputtering. Electrons, because of their small mass, should not cause any appreciable sputtering for energy levels less than 200 Kev.

The general conclusion that can be made regarding analytical consideration of damage estimates is that many assumptions are required in the analysis. Many of the assumptions are necessary to simplify the calculations in view of the complexities of the environment and the present state of the knowledge of the mechanisms of material damage. This is particularly true regarding compounds used as thermal-control materials. To obtain reliable damage estimates, simulation testing appears to be the only answer. The proper simulation of the environmental components on a real time scale would provide a method for accurately predicting the damage. Through the use of analytical techniques resulting from proper environmental testing of materials the over-all evaluation of material damage can be accomplished.

# CHAPTER VII

## EXPERIMENTAL APPARATUS AND EXPOSURE TECHNIQUES

The combined simulation of proton, ultraviolet and low density testing was performed in the AVCO Corporation Space Simulation Facility located in Tulsa, Oklahoma (Figure 24).

### Proton Source

A high voltage Van de Graff accelerator was used to generate protons over the energy range of interest. The proton energy range of the accelerator without an auxiliary power supply extends from a maximum of approximately 0.5 Mev to a minimum of 100 kev. Through the use of an auxiliary power supply, it was possible to provide an energy range of ions from 3 kev to 100 kev. The generator is also capable of accelerating electrons over the same range of energies as positive ions. An analyzing magnet system was provided for overall mass analysis of the ion beam.

### Solar Simulator

The solar spectrum covering the wavelength range from 0.2 to 4.0 microns was simulated by a single 5000 watt mercury-xenon lamp (Hanovia). The solar simulator was fabricated by Aerospace Corporation. Radiation from the lamp was collected by a large elliptical mirror

1. Sample Holder
2. Sample Entry Port
3. Ultra-High Vacuum Chamber
4. Solar Radiation Deflection Mirror
5. Solar Radiation Port
6. Solar Radiation Simulator
7. Particle Deflection Plates
8. Extreme UV Source
9. Bellows
10. Differentially Pumped Orifice
11. Differential Ion Boostivac Pump
12. Beam Monitor
13. Valve
14. Analyzer Magnet
15. Diffusion Pump and Battle
16. Acceleration Tube
17. Gas Source
18. Ion Source
19. Van de Graff Accelerator

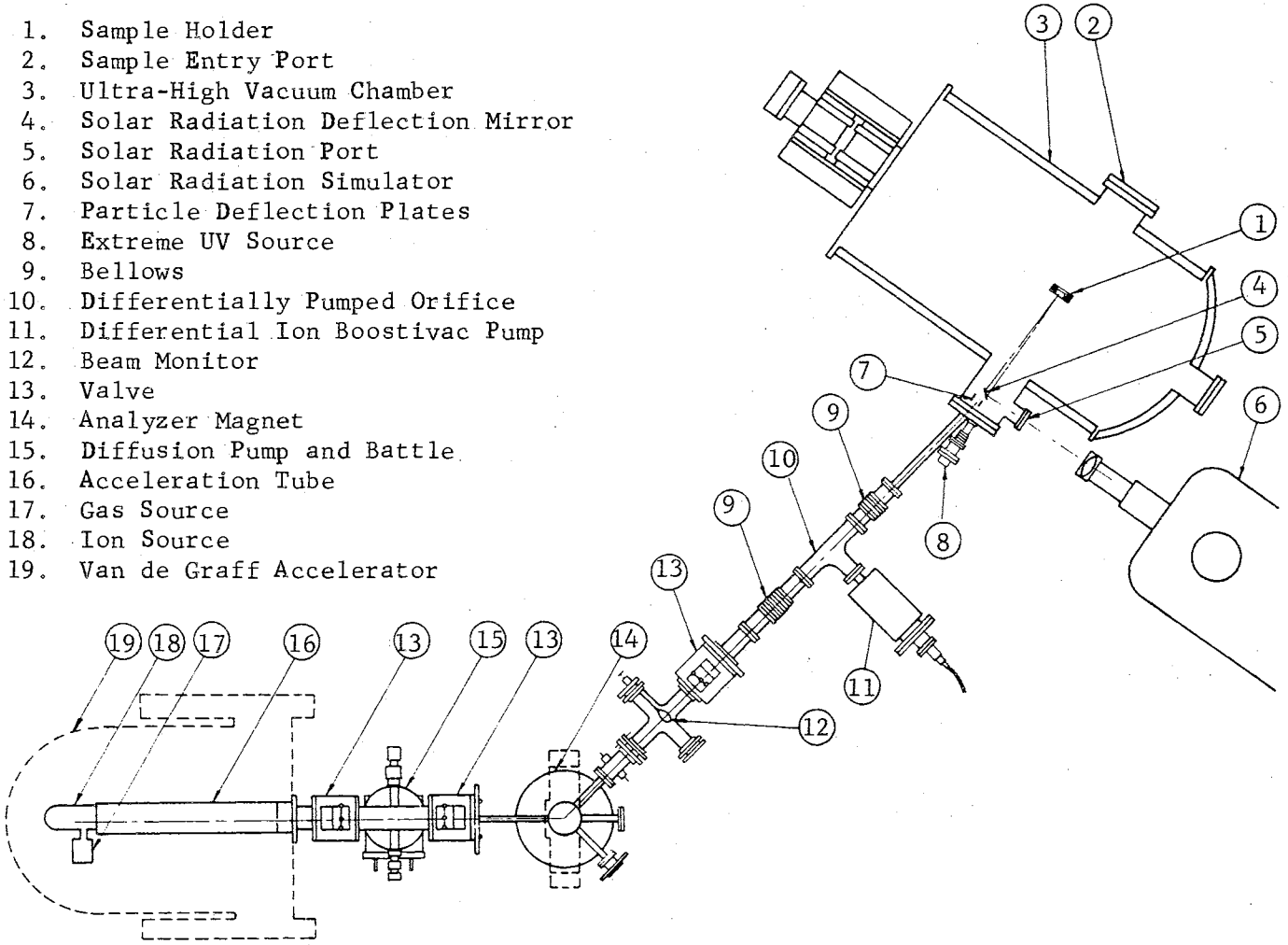


Figure 1. Schematic of Space Simulation Facility for Degradation Study

coated with a selective front face filter (Bausch and Lomb 90-8 reflective coating) in order to closely match the spectrum with that of the Johnson spectrum (Figure 2). A fused quartz optical system was provided to transmit the filtered radiation. The beam from the solar simulator was directed through a quartz entry port of the vacuum chamber onto the test specimen.

The solar simulator was calibrated with an Eppley Mark III filter radiometer, and a Hy Cal Engineering Pyrheliometer. The pyrheliometer had been calibrated against a National Bureau of Standards Lamp. Continuous monitoring of the intensity of the solar simulator was accomplished with a calibrated thermocouple radiometer located in the chamber. The solar simulator was calibrated in place by fabricating a pyrheliometer holder, similar to the sample holder, so that the detector, during calibration, was located in the same position as the sample in the chamber.

## Vacuum Chamber

The vacuum chamber was essentially a stainless steel cylinder with associated roughing, titanium sublimation, and sputter ion pumps (Figure 25). The chamber was 16 inches internal diameter and 30 inches long (inside). The double wall chamber was constructed of Type 304 stainless steel. It was capped at both ends with metal-to-metal type stainless steel high vacuum seal flanges. An annulus between the chamber walls served as a coolant passage for either water or liquid nitrogen.

Around the mid-periphery of the working area, 4 four-inch diameter ports spaced 90 degrees apart provided means of introducing test specimens,

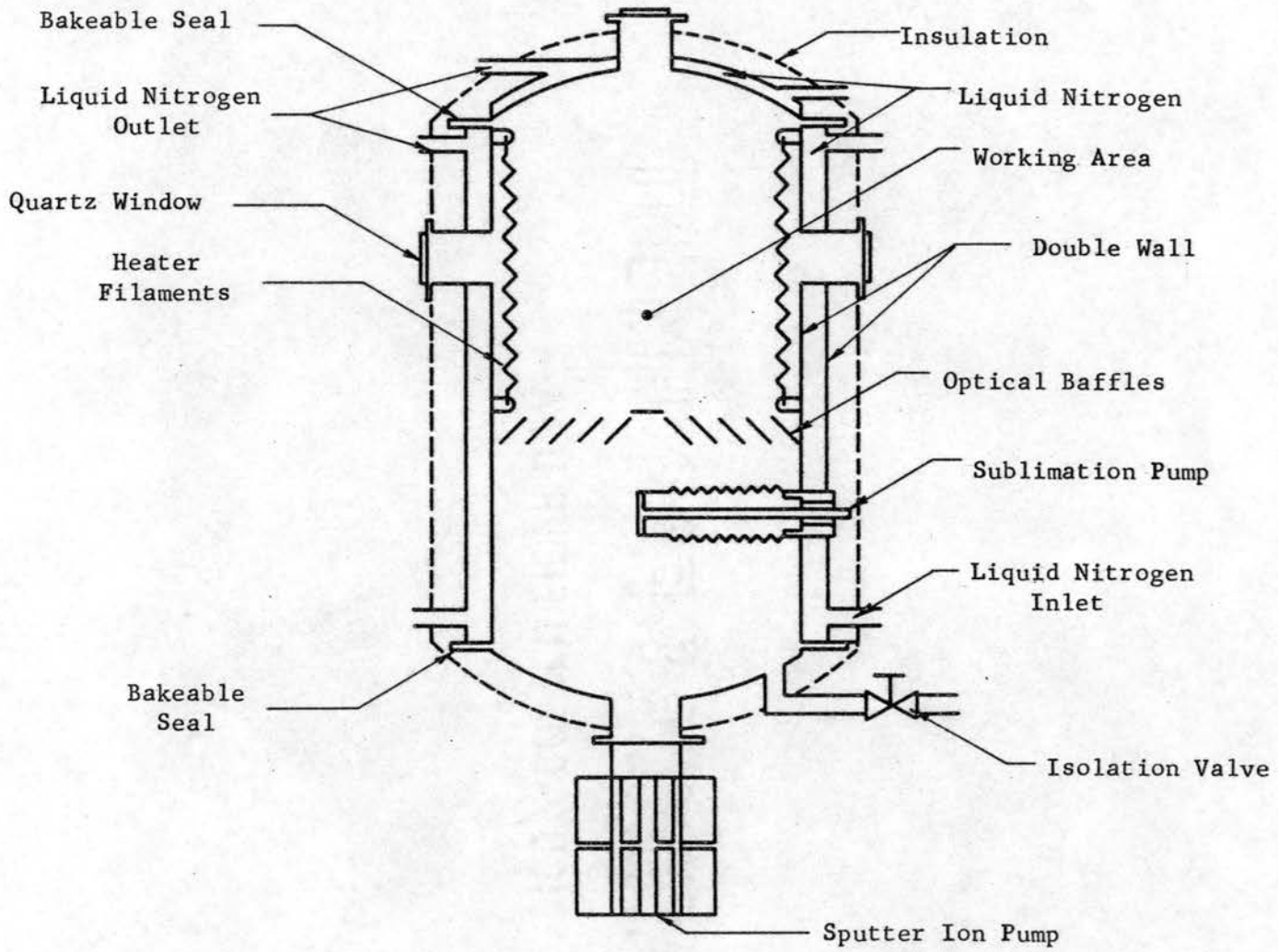


Figure 25. Schematic of Ultra-High Vacuum Chamber

radiation, measuring devices and other control apparatus into the test region. One of these ports provided visual observation of the experiments. Instrumentation feedthroughs were introduced into the working area in a region near the optical baffles. These feedthroughs provide power, fluids, and instrumentation to the chamber test area. Another four-inch port, identical with those on the walls, was located on the bulkhead of the test section end of the chamber.

An insulating jacket was provided for the chamber which curtailed the heat flux during bakeout and operation of the chamber. Tungsten heater elements were mounted on the inside walls of the test section which provide a capability of heating the chamber walls of the test section to a maximum temperature of approximately 700° F. A thermocouple to monitor the wall temperature was attached to the inside wall of the test section.

The pumping system of the chamber used a combination of metallic vapor deposition, sputter ion, cryogenic, and physical absoprtion processes, thus eliminating the vapor backstreaming and contamination problem associated with an oil diffusion pumping system.

The primary pump of the system is a titanium sublimation type located in one end of the chamber. An optical baffle, to prevent titanium vapor migration into the test section, was located between the pump and the test section. The pumping speed of this pump is approximately 5000 liters/second for nitrogen and approximately 10,000 liters/second for hydrogen. A sputter-ion pump with a pumping speed of 400 liters/second was attached to the bulkhead of the chamber.

Prior to operating the electronic pumps, the chamber was roughed to a vacuum of at least $10^{-2}$ torr by a mechanical pump. Hydrocarbons from the mechanical pump were isolated from the high vacuum side of the system by a molecular sieve type foreline trap. The roughing foreline was introduced into the high vacuum system at the base of the vapor pump bulkhead. An all-metal valve isolated the high vacuum system from the foreline. A thermocouple gauge was used to monitor the foreline pressure on the low vacuum side of the isolation valve.

The vacuum chamber was connected to the Van de Graff vacuum system through a differential-pumped pair of orifices. The differential vacuum pumping system was very similar to that used in the main chamber and consisted of a 25 liters/second sputter-ion pump in combination with a titanium sublimation pump which had a pumping speed of approximately 300 liters/second for hydrogen.

With the proton beam operating, the Van de Graff system, which was pumped with oil diffusion pumps, operates with a vacuum of approximately $10^{-5}$ torr. The differential-pumped orifice section maintained a vacuum of approximately $10^{-7}$ torr. The main chamber operated in a vacuum range of $10^{-9}$ torr to $10^{-10}$ torr.

## Sample Holder

The sample holder consisted of a square stainless steel or copper block having a hole with a shoulder for mounting the test sample, which was held in position by four spring-loaded clamps at the edge (Figure 26). The holder had channels for circulation of cooling fluid. Also, a heater element was mounted on the back of the sample

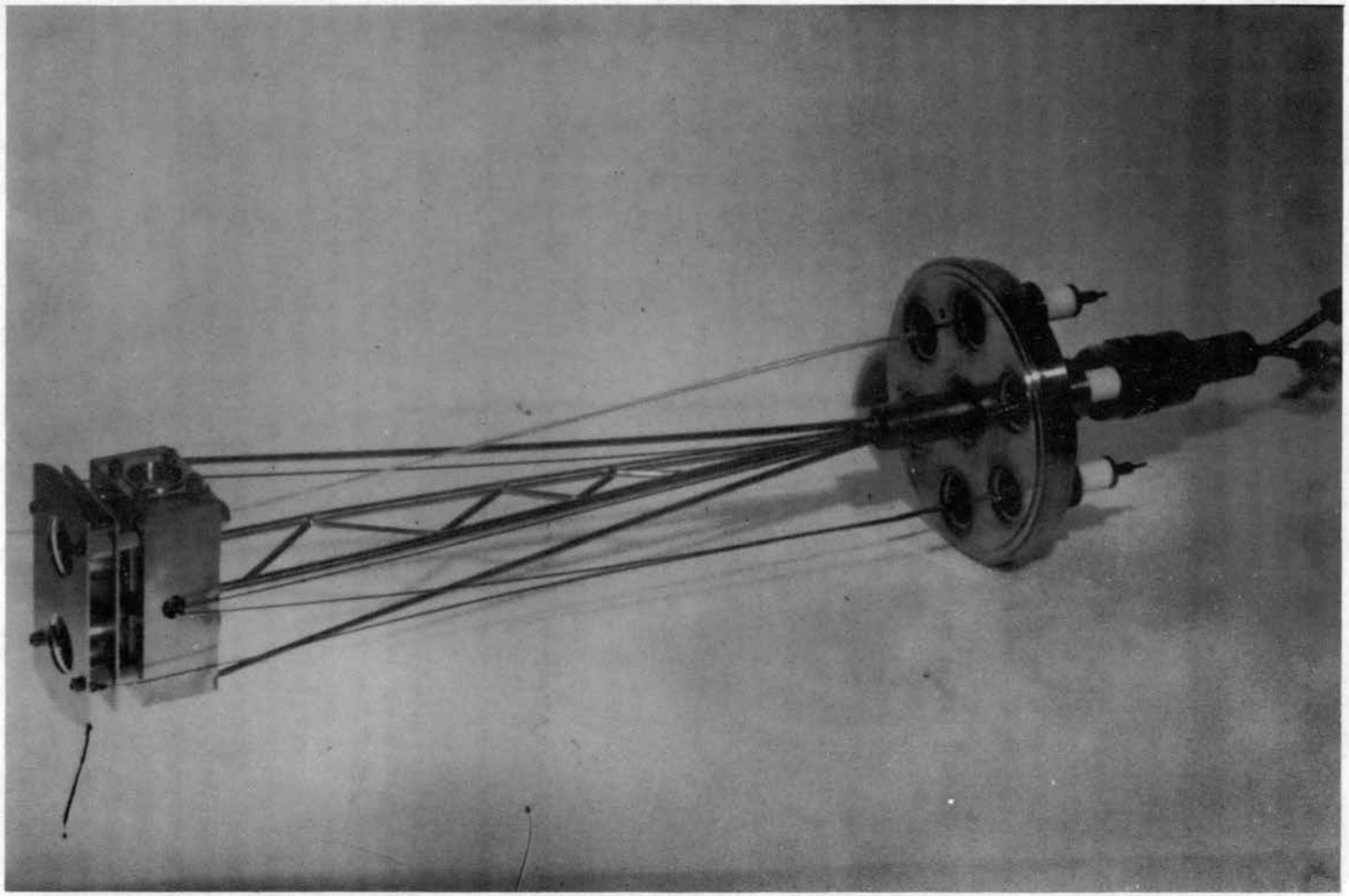

Figure 26. Schematic of Thermal-Control Material Sample Holder

holder for high-temperature sample testing. An automatic temperature control device maintained the sample temperature at the desired level. The temperature of the sample was measured with a thermocouple whose junction was silver brazed to a spring-loaded copper disc which pressed firmly against the back of the sample. The sample holder was physically supported in position near the center of the chamber by the tubes which carried the cooling fluid. The cooling tubes were supported by the flange through which they enter the chamber.

## Exposure Technique

The proton beam, after passing from the Van de Graff accelerator, was fed through and analyzing magnet that separated the protons from other hydrogen isotopes (or any other impurities which may be present in the hydrogen source). The beam then passed through the differentially pumped orifices into the vacuum chamber. The proton chamber entry port was so constructed as to introduce the beam via a tube directed at the sample, which was mounted on the sample holder located near the center of the chamber test section. After the proton beam passed through the orifices it emerges as a ribbon of particles, since the orifices are actually slits. The protons then passed between two electrostatic deflection plates to which was applied an oscillating voltage of saw-tooth waveform. This rastered the beam which scanned back and forth across the test sample. This technique was used to provide uniformity of exposure.

The proton beam current was measured by the use of an extremely fine tungsten screen held against the test sample. The screen was

attached to the end of an open metal cylinder which was mounted in the sample holder and insulated from the holder by a glass sleeve. The protons pass through the cylinder and screen before striking the test sample. The charge which builds upon the sample leaks to the screen and a wire connected to the cylinder conducts the current away for measurement. The shielding effect of the screen on the sample was considered negligible because its area was less than one percent of the exposed sample area.

When the protons strike the beam current pickup screen, some secondary electrons are ejected. If the ejected electrons were allowed to escape to the surroundings in the chamber, the beam current reading would have been erroneously high. To avoid this phenomena, a 90-volt battery was connected in series with the beam current meter so that the current pickup screen was biased positive, thus attracting the secondary electrons back to the screen. An insulated metal plate with a hole in it for the passage of the protons was mounted just ahead of the sample holder and was similarly biased 90-volts positive with respect to ground. Its purpose was to define efficiently the area over which the protons were delivered to the sample.

The special entry port which permitted the passage of the proton radiation also contains a quartz window through which the beam from the solar radiation entered the chamber and was directed onto the sample. The over-all design of the radiation (proton and solar) entry port provides a method of irradiating two samples with solar radiation and only one sample with proton radiation. Thus, providing

a combined environmental radiation (solar and proton) on one sample and solar-only radiation on the other test sample.

# CHAPTER VIII

## MEASUREMENT TECHNIQUES

### Optical Property Measuring Equipment

A Perkin-Elmer Model 112-U single-beam recording spectrophotometer with integrating sphere attachment and associated accessory light sources was used to obtain spectral reflectance data on the test samples over the wavelength range of 0.25 microns to 2.5 microns (Figure 27). The general theory on the use of the integrating sphere for spectral reflectance measurements is discussed in references 53 and 54. The monochromator was a Perkin-Elmer Model 99 Double Pass Monochromator with a $SiO_2$ prism. This type of prism is useful over a wavelength range of 0.2-4.0 microns. The objectionable first pass radiation was eliminated by masking corresponding halves of the entrance and exit slits of the monochromator.

The light sources used for optical measurements were xenon and tungsten lamps. The xenon lamp, because of its good ultraviolet characteristics, was used over the wavelength interval of 0.25-0.42 microns and the tungsten lamp for measurements over the wavelength interval of 0.42 to 2.5 microns.

A 1P 28 photomultiplier tube was used as a detector in the range of 0.25 to 0.70 microns and a lead sulfide cell for wavelengths greater than 0.70 microns. Linearity was established for each detector at

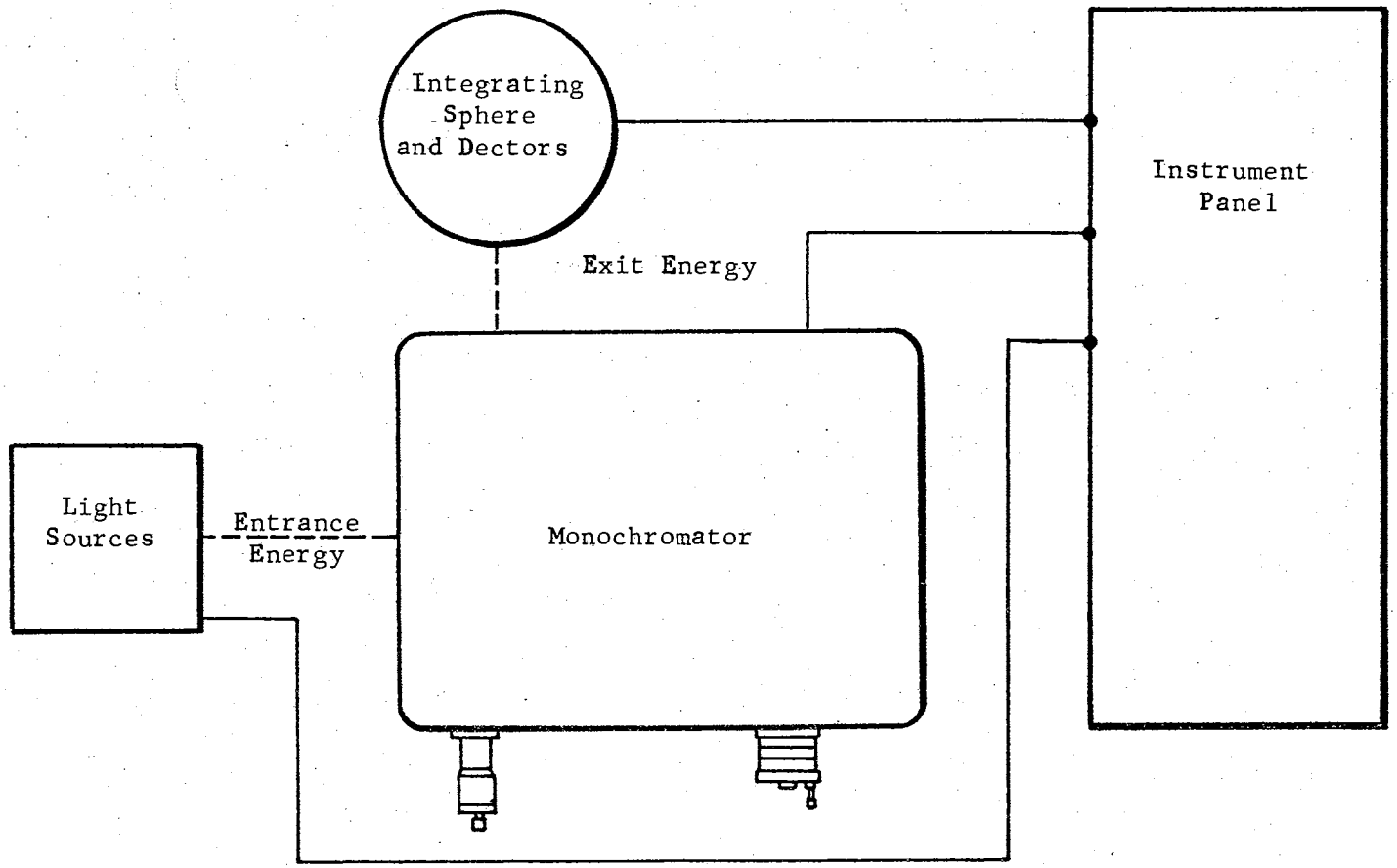


Figure 27. Optical Property Measuring Equipment

every desired wavelength setting for reflectance measurement over the wavelength interval of interest. This led to the establishment of a standard reflectance data sheet for all measurements. The data sheet specified the slit width as a function of wavelength.

The integrating sphere was uniformly coated with MgO. The sphere walls and sample holder were all smoked with approximately 2 (millimeters) of MgO deposit under 8000-v dc potential. For further information relating to MgO coating of spheres the reader is referred to references 54 and 55.

## Calibration of Prism

The method most used for calibrating spectrometers between 0.3 and 5 microns is that which employs the use of selected points from spectra data of a known source. Wavelengths of the bands calculated from the known spectra are then transferable directly to the spectrometer being calibrated. Spectra data usually requires the plotting of a calibration curve for that instrument. Many times these calibration curves do not lend themselves to precise interpolation because of the doubt in the curvature of the calibration curve between data points. McKinney and Friedel (56) developed an empirical equation which could be used to carry out the interpolation of the calibration curve for infrared prism spectrometers.

The empirical equation is based on the curve obtained from known spectral bands and by plotting for each band the wavelength drive turns, T versus $1/(\nu_2^2 - \nu^2)$, where $\nu$ is the corresponding frequency and $\nu_2$ is a Restrahlen frequency of the prism material. The calibration

curve then becomes a straight line for wavelengths greater than a certain value.

The prism used in measuring the optical properties of materials associated with this research study was $SiO_2$. The calibration of this prism followed the same procedure as outlined in the previous paragraphs. A selected group of spectral bands were established over the wavelength range of interest (.3 to 2.5 microns) using a mercury vapor lamp for obtaining experimental spectra data points as a function of wavelength drive turns (Table XI). By the use of the empirical equation from reference 56, and a Restrahlen wavelength of 8.3 microns for $SiO_2$ prism material (57), it was found the calibration curve for wavelengths greater than one micron became a straight line. Then by writing an equation for the straight line, $T = A + B\left[\lambda_2^2\lambda^2/(\lambda_2^2 - \lambda^2)\right]$ where A and B are constants and $\lambda_2$ is the Restrahlen wavelength, the necessary wavelength drum turns can be determined for any particular wavelength that falls within the wavelength interval of the straight line. For $SiO_2$ prism the calculations and the plotted data are shown in Table XI and Figure 28.

Upon further examination of the data in the lower wavelengths ($\lambda < 1$ micron), it was found that plotting T versus $(\lambda_2^2 - \lambda^2)/(\lambda_2^2\lambda^2)$, which is a reciprocal of that for $\lambda > 1$ micron, a linear relationship was again established for the spectra data. The straight line equation, the calculations and the plotting data are shown in Table XI and Figure 29.

These two empirical equations provide a method of precise interpolation of two linear equations for the calibration of a $SiO_2$ prism

TABLE XI

SPECTRAL DATA POINTS FOR $SiO_2$ PRISM

| Wavelength in Microns $\lambda$ | Screw Turns T | $\frac{\lambda_a^2 - \lambda^2}{\lambda_a^2 \lambda^2}$ | $\frac{\lambda_a^2 \lambda^2}{\lambda_a^2 - \lambda^2}$ |
|---|---|---|---|
| 0.2968 | 13.27 | 11.3491 | 0.0881 |
| 0.3023 | 13.02 | 10.9384 | 0.0914 |
| 0.3133 | 12.49 | 10.1791 | 0.0982 |
| 0.3342 | 11.63 | 8.9460 | 0.1117 |
| 0.3651 | 10.65 | 7.4930 | 0.1334 |
| 0.4048 | 9.76 | 6.0905 | 0.1641 |
| 0.4358 | 9.22 | 5.2514 | 0.1904 |
| 0.5460 | 8.02 | 3.3400 | 0.2993 |
| 0.5770 | 7.79 | 2.9893 | 0.3345 |
| 1.0140 | 6.25 | 0.9575 | 1.0442 |
| 1.1290 | 6.01 | 0.7700 | 1.2986 |
| 1.3680 | 5.53 | 0.5198 | 1.9236 |
| 1.5300 | 5.19 | 0.4126 | 2.4232 |
| 1.6930 | 4.83 | 0.3343 | 2.9906 |
| 1.7100 | 4.79 | 0.3274 | 3.0537 |
| 1.8140 | 4.53 | 0.2893 | 3.4556 |
| *2.0580 | 3.84 | 0.2215 | 4.5127 |

*Helium spectral data point

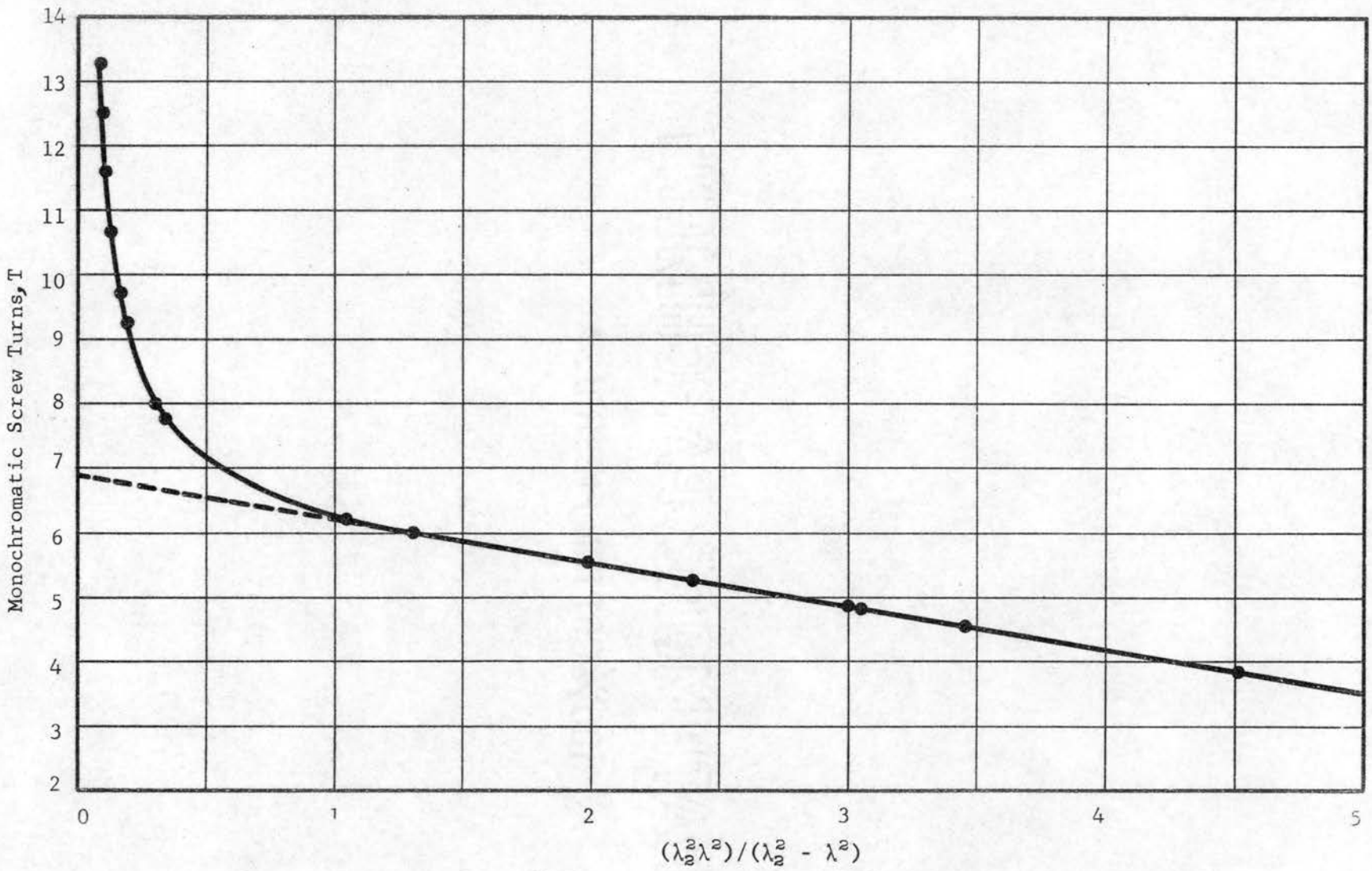


Figure 28. Relationship Between Monochromatic Screw Turns T and $(\lambda_2^2\lambda^2)/(\lambda_2^2 - \lambda^2)$ for $SiO^2$ Prism

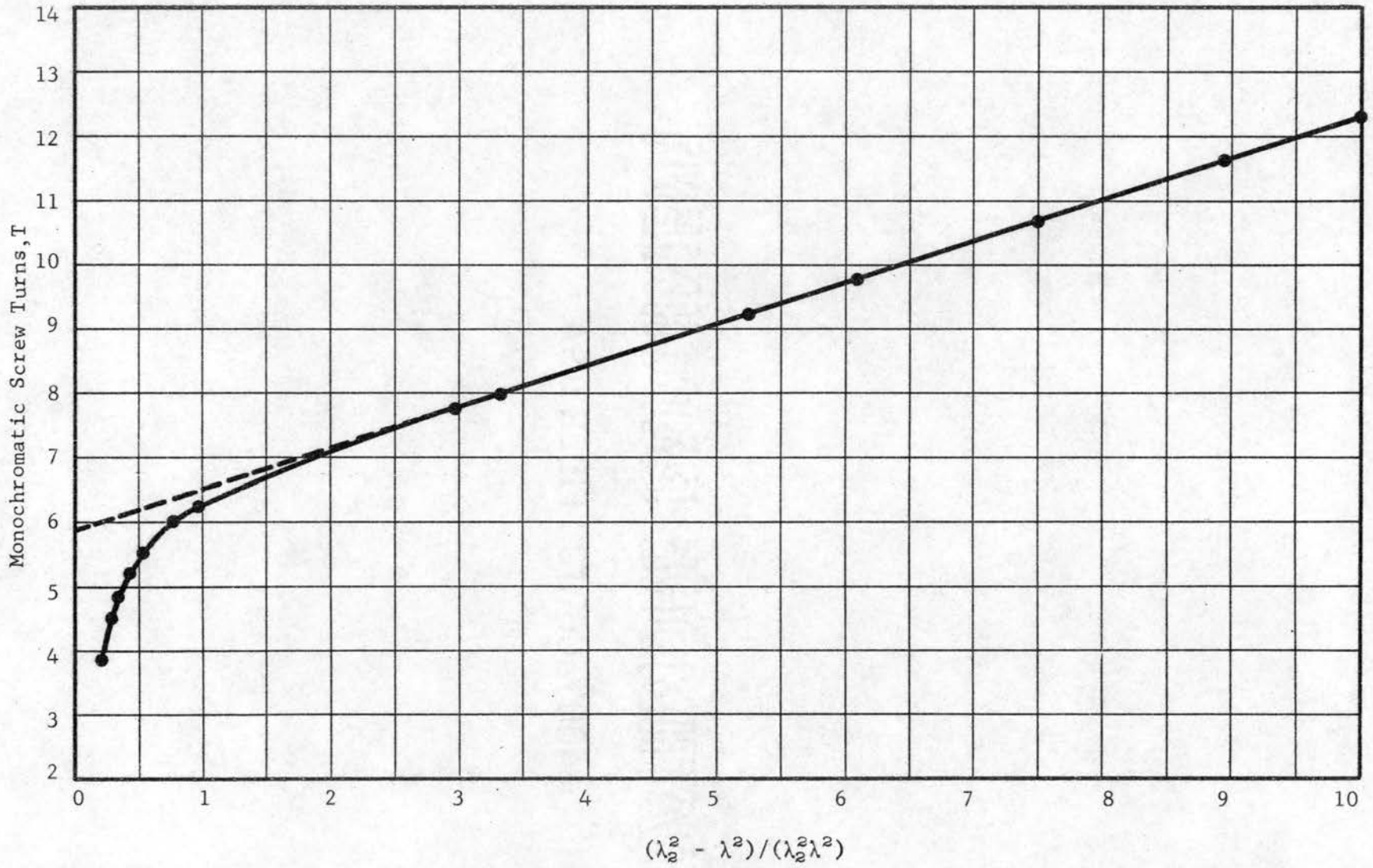


Figure 29. Relationship Between Monochromatic Screw Turns T and $(\lambda_2^2 - \lambda^2)/(\lambda_2^2\lambda^2)$ for $SiO_2$ Prism

over a wavelength interval of 0.3 to 2.5 microns, except in the non-linear region of one micron. In this particular region it was necessary to utilize the experimental spectra data points and plot an expanded calibration curve for more accurate interpolation.

## Evaluation of Calibration of Prisms by Theoretical Technique

The normal calibration of monochromators consists of using known frequencies of a number of absorption bands as standards. This procedure was discussed in detail in the preceding section. The over-all evaluation of the calibration can be developed theoretically through the known properties of the prism and the wavelength drive mechanism of the monochromator.

The evaluation requires the development of an expression for the wavelength, $\lambda$, as a function of the wavelength drive turns, T. The wavelength drive is related to the Littrow mirror of the monochromator by the drive arm length and the lead of the drive screw. The path followed by the radiant energy and component layout of the monochromator may be understood by referring to Figure 30. In normal operation the dispersed energy which has passed through the prism is scanned by the rotation of the Littrow mirror, which is controlled by the wavelength drive mechanism. The Littrow mirror returns the selected energy back through the prism to the other optical systems of the monochromator. By this technique the position of the Littrow mirror determines the wavelength or frequency isolated by the monochromator.

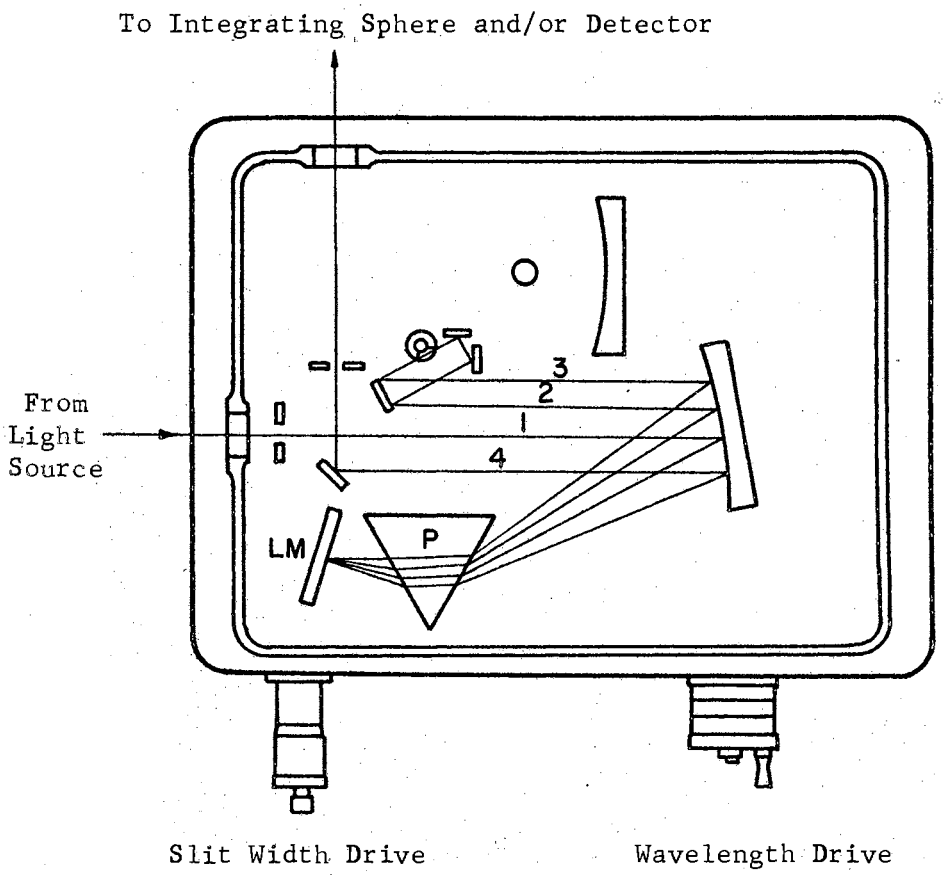


Figure 30. Optical Schematic of Monochromator. The numbers denote the beam path; P - Prism, LM - Littrow Mirror.

The Littrow mirror motion is controlled by the wavelength micrometer drum which is attached to the drive screw. The wavelength drum for the Perkin-Elmer Model 99 Double Pass Monochromator requires one turn for a Littrow mirror arc change of 1610 seconds. This relationship is also the same for the Model 98 Monochromator (58). Then in order to establish a theoretical expression for the wavelength, $\lambda$, as a function wavelength drive, it is necessary to express $\lambda$ as a function of $\theta$, where $\theta$ is the angular rotation of the Littrow mirror.

This may be obtained by the integration of $d\lambda/d\theta = f(\lambda)$. In this equation $d\lambda/d\theta$ can be obtained from

$$\frac{d\lambda}{d\theta} = \frac{d\lambda}{dN}\,\frac{dN}{d\theta} \tag{8-1}$$

where N is the index of refraction of the prism material. The index of refraction is given by the following equation (59)

$$N^2 = A + \sum_{I=1}^{I=1_{max}} B_I \lambda^{2I} + \sum_{J=1}^{J=J_{max}} \frac{C_J \lambda^2}{\lambda^2 - D_J} + \sum_{K=1}^{K=K_{max}} \frac{E_K}{\lambda^2 - F_K} \tag{8-2}$$

where $\lambda$ is in microns and the coefficients depend on the various prism materials. The index of refraction equation for $SiO_2$ is as follows

$$N^2 = 2.979864 + \frac{0.008777808}{\lambda^2 - 0.010609} + \frac{84.06224}{\lambda^2 - 96.000} \tag{8-3}$$

for $0.215 \leq 3.6$ microns. The derivative of the index of refraction with respect to wavelength is obtained by differentiation and the result is

$$\frac{dN}{d\lambda} = \frac{\sum_{I=1}^{I=I_{max}} I\, B_I \lambda^{2I-1} + \sum_{J=1}^{J=J_{max}} \frac{(\lambda^2 - D_J)(C_J\lambda) - C_J\lambda^3}{(\lambda^2 - D_J)^2} - \sum_{K=1}^{K=K_{max}} \frac{E_K\lambda}{(\lambda^2 - F_K)^2}}{N} \tag{8-4}$$

which becomes for $SiO_2$ prism

$$\frac{dN}{d\lambda} = - \frac{\frac{0.008777808}{(\lambda^2 - 0.010609)^2} + \frac{84.06224}{(\lambda^2 - 96.000)^2}}{N} \tag{8-5}$$

The relationship for $d\theta/dN$ is given by the following equation (60)

$$\frac{d\theta}{dN} = \frac{2 \sin \varphi}{(1 - N^2 \sin^2 \varphi)^{\frac{1}{2}}} \tag{8-6}$$

where $2\varphi$ is the apex angle of the prism.

By using the two equations for $dN/d\lambda$ and $d\theta/dN$, $d\lambda/d\theta$ can be obtained using point by point evaluation where

$$\frac{d\lambda}{d\theta} = f(\lambda) \tag{8-7}$$

then

$$\int_{\lambda_1}^{\lambda_2} \frac{d\lambda}{f(\lambda)} = \int_{\theta_1}^{\theta_2} d\theta \tag{8-8}$$

Using published data on prism materials and selected curves in reference 59, calculated results for an $SiO_2$ prism with apex angles of 50° and 60° are tabulated in Table XII. The table also shows the calibration data developed by the techniques described in the preceding section.

TABLE XII

THEORETICAL CALIBRATION DATA FOR $SiO_2$ PRISM

| Wavelength λ, Microns | 50° $S_iO_2$ Prism | | | 60° $S_iO_2$ Prism | | |
|---|---|---|---|---|---|---|
| | $f(\lambda)$[1] | Theor.[1] Turns | Calibrated[2] Turns | $f(\lambda)$[1] | Theor.[1] Turns | Calibrated[2] Turns |
| 0.3 | 0.3590 | 0 | 0 | 0.4933 | 0 | 0 |
| 0.4 | 0.1348 | 2.481 | 2.43 | 0.1842 | 3.050 | 3.08 |
| 0.5 | 0.0667 | 3.443 | 3.44 | 0.0909 | 4.398 | 4.50 |
| 0.6 | 0.0397 | 3.996 | 4.01 | 0.0541 | 5.152 | 5.28 |
| 0.7 | 0.0268 | 4.357 | 4.38 | 0.0364 | 5.645 | 5.74 |
| 0.8 | 0.0192 | 4.617 | 4.66 | 0.0261 | 5.998 | 6.05 |
| 0.9 | 0.0160 | 4.824 | 4.84 | 0.0218 | 6.282 | 6.36 |
| 1.0 | 0.0139 | 5.005 | 5.01 | 0.0188 | 6.527 | 6.67 |
| 1.1 | 0.0128 | 5.171 | 5.18 | 0.0174 | 6.753 | 6.93 |
| 1.2 | 0.0125 | 5.331 | 5.34 | 0.0169 | 6.970 | 7.08 |
| 1.3 | 0.0122 | 5.488 | 5.49 | 0.0166 | 7.185 | 7.33 |
| 1.4 | 0.0124 | 5.646 | 5.65 | 0.0169 | 7.401 | 7.52 |
| 1.5 | 0.0126 | 5.808 | 5.81 | 0.0171 | 7.621 | 7.72 |
| 1.6 | 0.0131 | 5.975 | 5.98 | 0.0177 | 7.849 | 7.94 |
| 1.7 | 0.0137 | 6.150 | 6.16 | 0.0186 | 8.087 | 8.17 |
| 1.8 | 0.0142 | 6.331 | 6.34 | 0.0193 | 8.334 | 8.42 |
| 1.9 | 0.0149 | 6.521 | 6.54 | 0.0201 | 8.592 | 8.69 |
| 2.0 | 0.0156 | 6.720 | 6.74 | 0.0211 | 8.863 | 8.98 |
| 2.1 | 0.0164 | 6.930 | 6.96 | 0.0223 | 9.148 | 9.28 |
| 2.2 | 0.0173 | 7.150 | 7.18 | 0.0234 | 9.447 | 9.60 |
| 2.3 | 0.0180 | 7.381 | 7.41 | 0.0244 | 9.776 | 9.94 |
| 2.4 | 0.0191 | 7.625 | 7.66 | 0.0258 | 10.090 | 10.31 |
| 2.5 | 0.0201 | 7.882 | 7.92 | 0.0272 | 10.438 | 10.69 |

(1) Theoretically calculated by equation (8-8).

(2) Calibration curves developed by empirical technique.

## Discussion on Calibration of Prisms

Two monochromators and associated integrating spheres were calibrated by using the techniques discussed in the two preceding sections. Both monochromators were Perkin-Elmer Model 99 Double Pass Monochromators with $SiO_2$ prisms (one with a 50 degree apex angle and the other a 60 degree apex angle). The 50 degree prism was used for measuring the optical degradation of all samples. Many of the optical property measurements were repeated with the 60 degree $SiO_2$ prism monochromator. Spectral measurements made with the two apparatus were within $\pm$ 0.5%, which was close to the reproducibility of the detector-amplifier system. Both monochromators were also calibrated relative to MgO standard as recommended in reference 61. Reflectance data was in agreement with that published for MgO by Middleton and Sanders (62).

The advantages of these calibration techniques are:

1. This is a theoretical method of checking the experimental spectra data.
2. The technique limits the spectral data to selection of the strong and sharp bands.
3. It is applicable to short wavelengths and long wavelengths.
4. The technique establishes confidence in the optical property measurements.

## Microscopic Analysis

Microscopic surface and cross-section analysis were accomplished through the use of a "Zetopan" Research Microscope produced by Reichert

Company of Austria. The microscope was equipped with a polarization interferometer and interference contrast equipment for examination of surface roughness and determining depth of cracks and other surface irregularities.

Cross-section analysis was accomplished by stripping the irradiated coating from the backing material and molding it into melted beeswax. After the beeswax was cooled, very thin slices of the coating were cut and examined under the microscope.

## Sample Reflectance Measurements

The reflectance measurements of the exposed samples were undertaken immediately upon removal from the space simulator. This procedure was established to minimize the possibility of atmospheric bleaching of the irradiated and vacuum-exposed samples. A standard reflectance measuring technique was utilized for all samples. A common monochromator slit width, light source power and photomultiplier power settings were established for each spectral point of interest between the wavelengths of 0.2 microns to 2.5 microns. A twenty degree angle of incidence for each sample was used for all reflectance measurements.

# CHAPTER IX

# DISCUSSION OF RESULTS

## Description of Thermal-Control Materials

The thermal-control materials selected for testing were considered to be the most highly developed coatings available today for space system applications. The thermal coatings were prepared by the Thermophysics Group of the Aerospace Sciences Laboratory at Lockheed Missiles and Space Company, Palo Alto, California. Initially three coatings (white, grey and black) were selected for testing. The white coating dominated the over-all test program because of its degradation characteristics and importance in the over-all design of an effective thermal-control system.

Dow Corning polymethyl siloxane was used as the vehicle for all three coatings. The white coating was one to one by weight, pigment to vehicle; pigment was rutile $TiO_2$ calcined (TITANOX R.A.N.C.). The thickness of the coating was approximately 0.006 inches. The black coating was one to five by weight, pigment to vehicle; pigment was carbon powder. The coating thickness was approximately 0.0015 inches. The grey coating was a mixture of the two paints, 30 parts black to 100 parts white.

The procedure for preparation was the same as the preparation of coatings for space system applications. Test samples for each coating were prepared from the same batch of paint and punches from large

coated panels. This procedure was established to eliminate the possibility of batch to batch variations and obtain a uniform thickness for each sample. All samples were 15/16 inches in diameter with 1/16 inch aluminum backing.

## Selection of the Test Environment

Considering the complexity of the actual space environment and the simulation capability of the experimental equipment, it was necessary to limit the simulated space parameters to a number consistent with the need for reaching meaningful conclusions. It would have been most desirable to undertake a test program which would have determined the degradation of the coatings as a function of many significant parameters. Such parameters as type of coatings, type of radiation, energy of radiation, flux of radiation, integrated flux of radiation, temperature of sample, and low density could each have been considered as a variable. To conduct synergestic type testing as a function of each environmental parameter would have required many tests to obtain the desired data necessary for determining the synergestic functional relationship.

After careful evaluation of the above difficulties, it became evident that the type of coating should be limited to the white and the type of radiation should be limited to proton and electromagnetic. Proton radiation was selected because of the existing operational mode of the accelerator and the anticipated long term missions of space systems in the intense proton radiation regions of the space environment. The values of proton energy and integrated fluxes were selected on the basis of exposure condition for an approximate one year mission in the

solar wind environment. A summary of the test data and the simulated parameters are shown in Table XIII.

## Calculation of Solar Absorptance ($\alpha_s$)

The solar absorptances were calculated from the spectral reflectance data. Absolute spectral reflectance was calculated for selected wavelength intervals over the wavelength region of interest. The wavelength intervals selected represented equal energy increments for the solar spectrum in space. The average spectral reflectances for the equal energy increments were then summed and divided by the number of increments to obtain an integrated solar reflectance ($\rho_s$). The solar absorptance ($\alpha_s$) was obtained from the solar reflectance.

$$\alpha_s = 1 - \rho_s \tag{9-1}$$

## Calculation of Total Energy Absorbed

The total energy absorbed per unit area of sample, $E_a$, was calculated from the proton energy exposure condition as follows:

$$E_a(\text{joules/cm}^2) = \frac{\text{Proton energy (ev) x Flux (P/cm}^2\text{-sec) x Time (sec)}}{6.28 \times 10^{18}}$$

This provides a method of comparing the degradation of the exposed samples as a function of energy absorbed for various proton energies, fluxes and exposure doses (integrated flux).

## Results

The results of the tests conducted as summarized in Table XIII will be discussed relative to the optical degradation of the exposed

# TABLE XIII

## SUMMARY OF TESTS

| Test No. | Proton Energy (kev) | Flux ($10^{-11}$) ($p/cm^2$-sec) | Integrated Flux ($10^{-15}$) ($p/cm^2$) | Pressure (torr) | Sample Temperature (°F) | Ultraviolet (Solar Suns) | Total Ultraviolet (ESH) | Total Proton Energy (Joules/$cm^2$) | Solar Absorptance ($\alpha_s$) | $\Delta\alpha_s$ |
|---|---|---|---|---|---|---|---|---|---|---|
| | | | | | WHITE COATING | | | | | |
| 1 | - | - | - | $10^{-9}$ | - | - | - | - | 16.5 | 0 |
| 2 | 10 | 5.50 | 1.0 | $10^{-9}$ | 65 | - | - | 1.6 | 17.6 | 1.1 |
| 3 | 10 | 5.50 | 10.0 | $10^{-9}$ | 65 | - | - | 16.0 | 29.1 | 12.6 |
| 4 | 10 | 5.50 | 50.0 | $10^{-9}$ | 65 | - | - | 80.0 | 58.8 | 42.3 |
| 5 | 10 | 5.50 | 10.0 | $10^{-8}$ | 70 | 10 | 190 | 16.0 | 34.5 | 18.0 |
| 6 | 10 | 5.50 | 50.0 | $10^{-8}$ | 70 | 10 | 190 | 80.0 | 62.1 | 45.6 |
| 7 | 10 | 5.50 | 3.0 | $10^{-8}$ | 70 | 10 | 190 | 4.8 | 22.3 | 5.8 |
| 8 | - | - | - | - | 70 | 10 | 190 | - | 18.0 | 1.5 |
| 9 | - | - | - | - | 70 | 10 | 190 | - | 18.2 | 1.7 |
| 10 | 10 | 2.80 | 5.0 | $10^{-9}$ | 65 | - | - | 8.0 | 22.6 | 6.1 |
| 11 | 10 | 1.40 | 2.5 | $10^{-9}$ | 65 | - | - | 4.0 | 18.9 | 2.4 |
| 12 | 50 | 5.50 | 10.0 | $10^{-8}$ | 65 | - | - | 80.0 | 59.3 | 32.8 |
| 13 | 50 | 5.50 | 2.0 | $10^{-8}$ | 65 | - | - | 16.0 | 26.6 | 10.1 |
| 14 | 50 | 5.50 | 1.0 | $10^{-8}$ | 65 | - | - | 8.0 | 21.3 | 4.8 |
| 15 | 50 | 5.50 | 5.0 | 10-8 | 65 | - | - | 40.0 | 37.8 | 21.3 |
| 16 | 100 | 0.11 | 1.0 | $10^{-8}$ | 65 | - | - | 16.0 | 23.5 | 7.0 |
| 17 | 100 | 5.50 | 1.0 | $10^{-8}$ | 65 | - | - | 16.0 | 23.4 | 6.9 |
| 18 | 100 | 11.00 | 1.0 | $10^{-8}$ | 65 | - | - | 16.0 | 23.4 | 6.9 |
| 19 | 100 | 5.50 | 5.0 | $10^{-8}$ | 65 | - | - | 80.0 | 33.8 | 17.3 |
| 20 | 100 | 5.50 | 0.5 | $10^{-8}$ | 65 | - | - | 8.0 | 19.7 | 3.2 |
| 21 | 100 | 5.50 | 5.0 | $10^{-8}$ | -300 | - | - | 80.0 | 32.3 | 15.8 |
| 22 | 100 | 5.50 | 5.0 | $10^{-8}$ | 100 | - | - | 80.0 | 35.8 | 19.3 |
| 23 | 100 | 5.50 | 5.0 | $10^{-8}$ | 200 | - | - | 80.0 | 37.1 | 20.6 |
| 24 | 100 | 5.50 | 5.0 | $10^{-8}$ | 300 | - | - | 80.0 | 39.8 | 23.3 |
| 25* | - | - | - | $10^{-6}$ | 65 | - | - | - | 17.3 | 0.8 |
| 26 | - | - | - | $10^{-6}$ | 55 | 8 | 560 | - | 23.5 | 5.7 |
| 27 | - | - | - | $10^{-7}$ | 155 | 8 | 560 | - | 25.1 | 6.5 |
| 28 | - | - | - | $10^{-7}$ | 215 | 8 | 560 | - | 26.9 | 7.3 |
| | | | | | GREY COATING | | | | | |
| 29* | - | - | - | $10^{-6}$ | 65 | - | - | - | 67.6 | 0.4 |
| 30 | - | - | - | $10^{-8}$ | 70 | 10 | 190 | - | 68.4 | 0.8 |
| 31 | - | - | - | $10^{-6}$ | 55 | 6 | 420 | - | 71.0 | 1.0 |
| 32 | - | - | - | $10^{-7}$ | 155 | 6 | 420 | - | 71.3 | 1.4 |
| 33 | - | - | - | $10^{-7}$ | 215 | 6 | 420 | - | 71.7 | 1.7 |
| | | | | | BLACK COATING | | | | | |
| 34* | - | - | - | $10^{-6}$ | 65 | - | - | - | 95.7 | 0.0 |
| 35 | - | - | - | $10^{-8}$ | 70 | 10 | 190 | - | 95.8 | 0.0 |
| 36 | - | - | - | $10^{-6}$ | 55 | 6 | 420 | - | 96.4 | <1.0 |
| 37 | - | - | - | $10^{-7}$ | 155 | 6 | 420 | - | 96.7 | <1.0 |
| 38 | - | - | - | $10^{-7}$ | 215 | 6 | 420 | - | 96.3 | <1.0 |

*After 650 hours

ESH - equivalent solar sun hours

samples. Optical degradation is defined as an increase in spectral absorptance or as a decrease in spectral reflectance in the solar region of electromagnetic radiation.

Low Density Effects

The white, grey and black coatings were exposed to a low density environment of apprxoimately $10^{-6}$ torr for a period of 650 hours. Each coating experienced a measurable weight loss: white--0.17%, grey--0.19%, black--0.16%. The increase in the solar absorptance for the white and grey coatings when exposed to the low density environment alone was less than one percent. The black coating showed no measurable optical degradation for the vacuum-only exposure.

Proton Energy Effect

The $TiO_2$ white coating was irradiated with protons of energies of 10 kev, 50 kev, and 100 kev. The proton bombardment induced optical damage of the coatings in all cases. The optical degradation as measured by spectral reflectance is shown in Figures 31, 32, 33, 34, and 35. It should be noted that the greatest decrease in reflectance occurs in the region of approximately 0.5 microns, which is the region of high solar energy. Figure 31 shows the change in spectral reflectance produced by 10 kev protons at various integrated fluxes. The change in solar absorptance for an integrated flux of $1 \times 10^{15}$ p/cm$^2$ was found to be very small ($\Delta\alpha_s = 1.1\%$). At an integrated flux of $5 \times 10^{16}$ p/cm$^2$ the change in solar absorptance was 42.3%. Figure 32 shows the effect of 10 kev proton bombardment for a constant time of five hours at three different

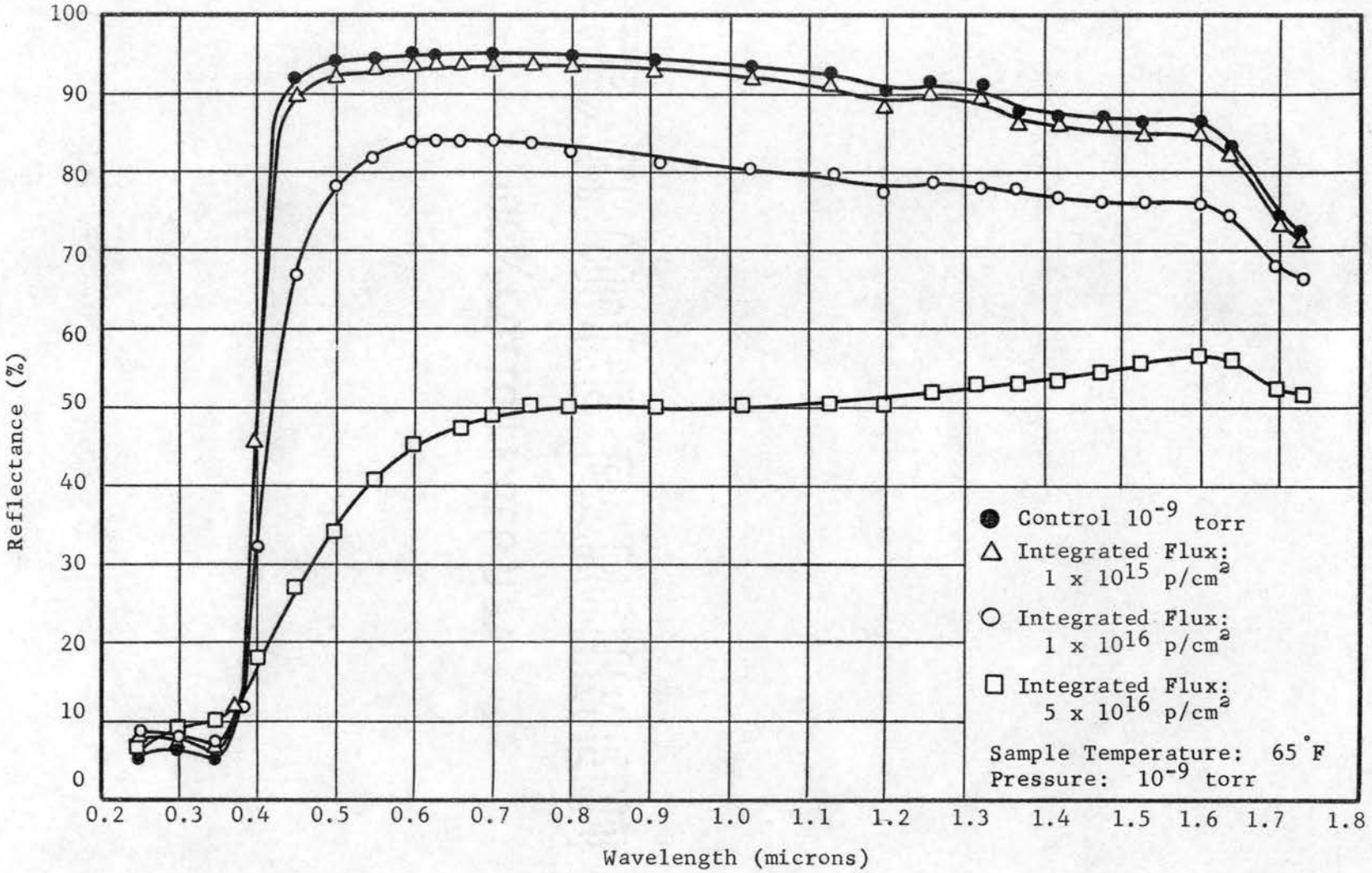


Figure 31. Optical Degradation of $TiO_2$ Coating for 10 kev Proton Irradiation of a Constant Flux ($5.5 \times 10^{11}$ p/cm$^2$-sec) for Various Integrated Fluxes

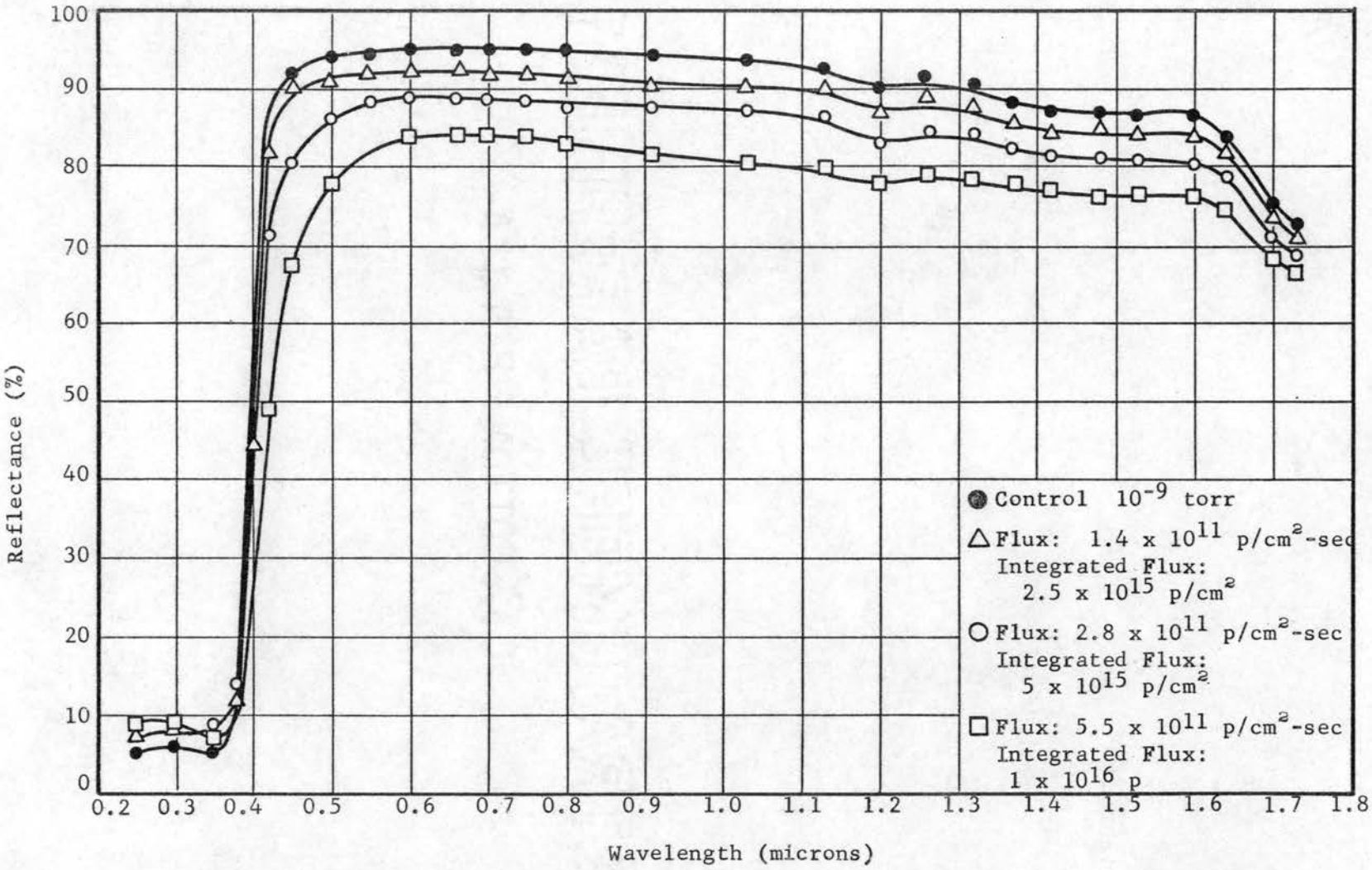


Figure 32. Optical Degradation of $TiO_2$ Coating For Five Hours of Irradiation With 10 kev Protons for Various Integrated Fluxes at a Sample Temperature of 65°F and a Pressure of $10^{-9}$ torr.

integrated fluxes. Both the flux and integrated fluxes were varied to achieve two times the integrated flux of the preceding test. The change in solar absorptance was 2.4% for an integrated flux of $2.4 \times 10^{15}$ p/cm$^2$, 6.1% for an integrated flux of $5 \times 10^{15}$ p/cm$^2$ and 18.0% for an integrated flux of $1 \times 10^{16}$ p/cm$^2$.

The effect of 50 kev proton irradiation of the $TiO_2$ white coating at a constant flux, for four integrated fluxes, is shown in Figure 33. Again, the maximum change occurs in a region of approximately 0.5 microns and the shape of the reflectance curves are similar to those for 10 kev proton irradiation. The change in solar absorptance varied from 5.0% for an integrated flux of $1 \times 10^{15}$ p/cm$^2$ to 37.8% for an integrated flux of $1 \times 10^{16}$ p/cm$^2$.

The effect of 100 kev proton irradiation of the white coating is shown in Figure 34. The optical degradation curves are similar to the 10 kev and 50 kev degradation curves. The comparison of optical degradation for 10 kev, 50 kev and 100 kev proton irradiation for an integrated flux of $1 \times 10^{15}$ p/cm$^2$ at a flux of $5.5 \times 10^{11}$ p/cm$^2$-sec is shown in Figure 35. An equivalent integrated flux of a more energetic particle produces a proportionately greater degradation. The induced damage by the 10 kev, 50 kev and 100 kev proton irradiation for an integrated flux of $1 \times 10^{15}$ p/cm$^2$ resulted in a change of solar absorptance of 1.1%, 5.0%, and 6.8% respectively.

Comparison of the optical damage produced per equivalent amount of energy absorbed (joules/cm$^2$) for proton energies of 10 kev, 50 kev and 100 kev is shown in Figure 36. The increase in solar absorptance is much greater for the 10 kev proton irradiation. The curves show that

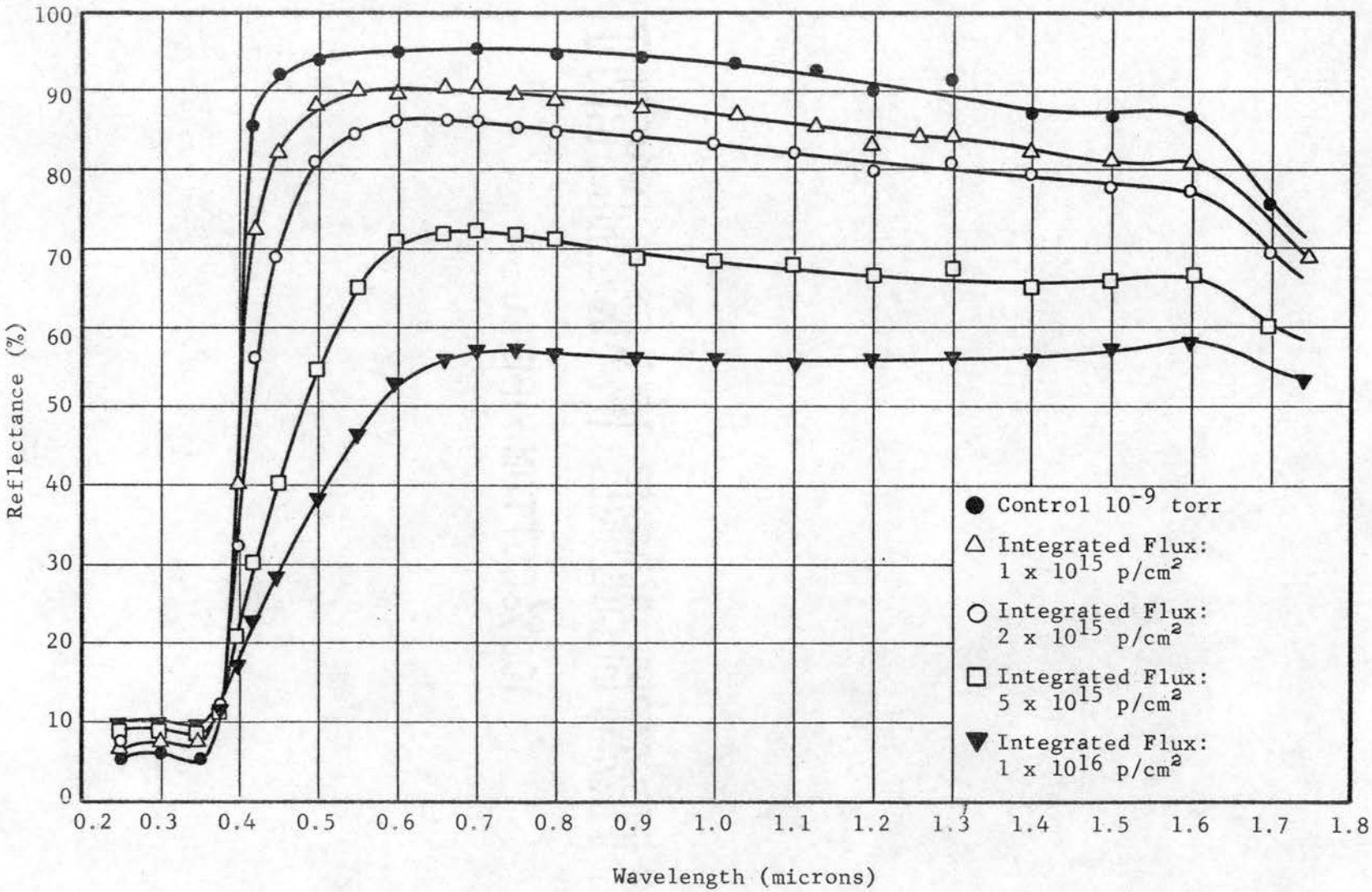


Figure 33. Optical Degradation of $TiO_2$ Coating After 50 kev Proton Irradiation at a Flux Level of 5.5 x $10^{11}$ p/cm$^2$-sec, a Sample Temperature of 65 °F, and a Pressure of 10-9 torr

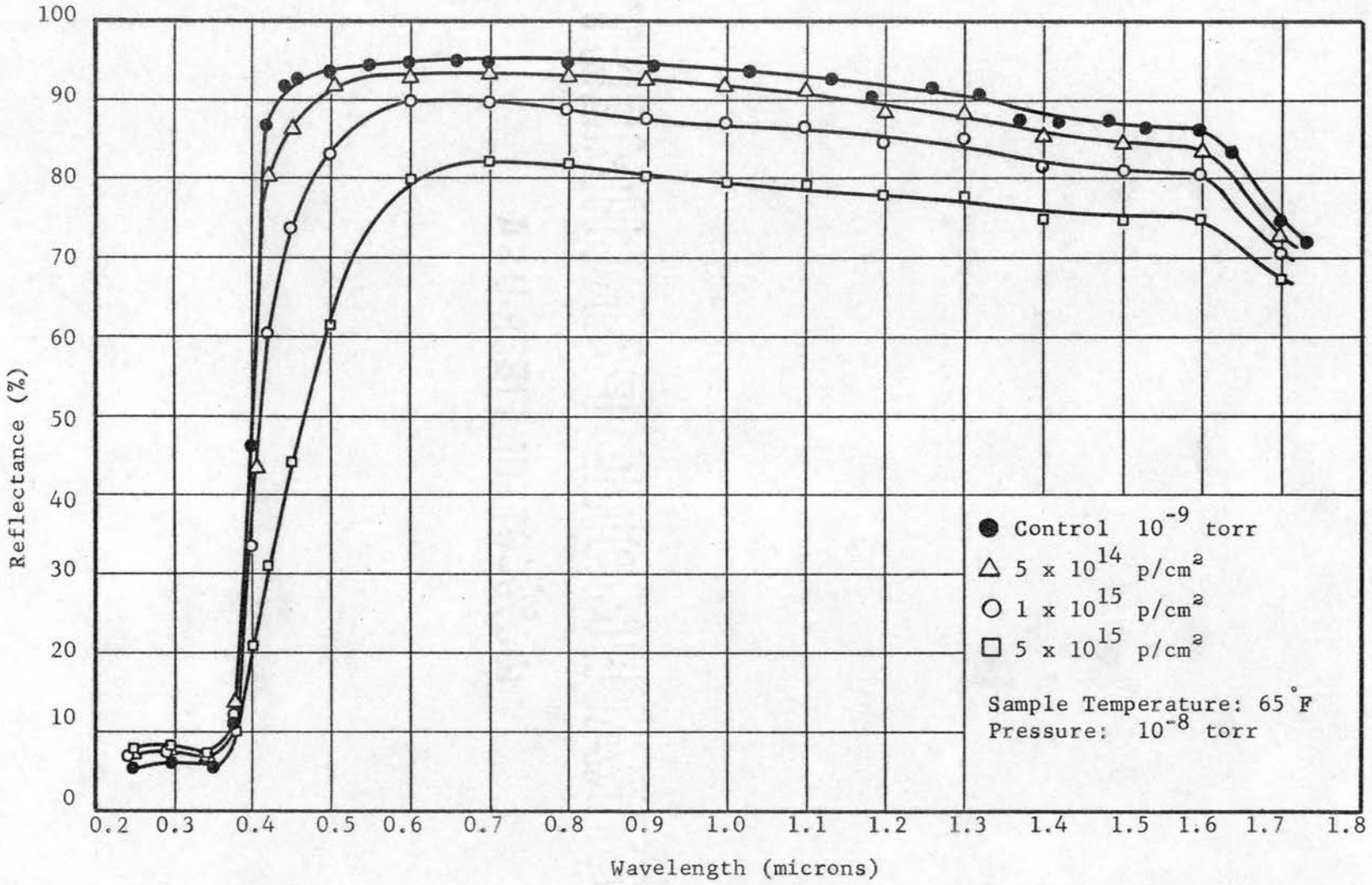


Figure 34. Optical Degradation of $TiO_2$ Coating After 100 kev Proton Irradiation at a Flux of $5.5 \times 10^{11}$ p/cm$^2$-sec

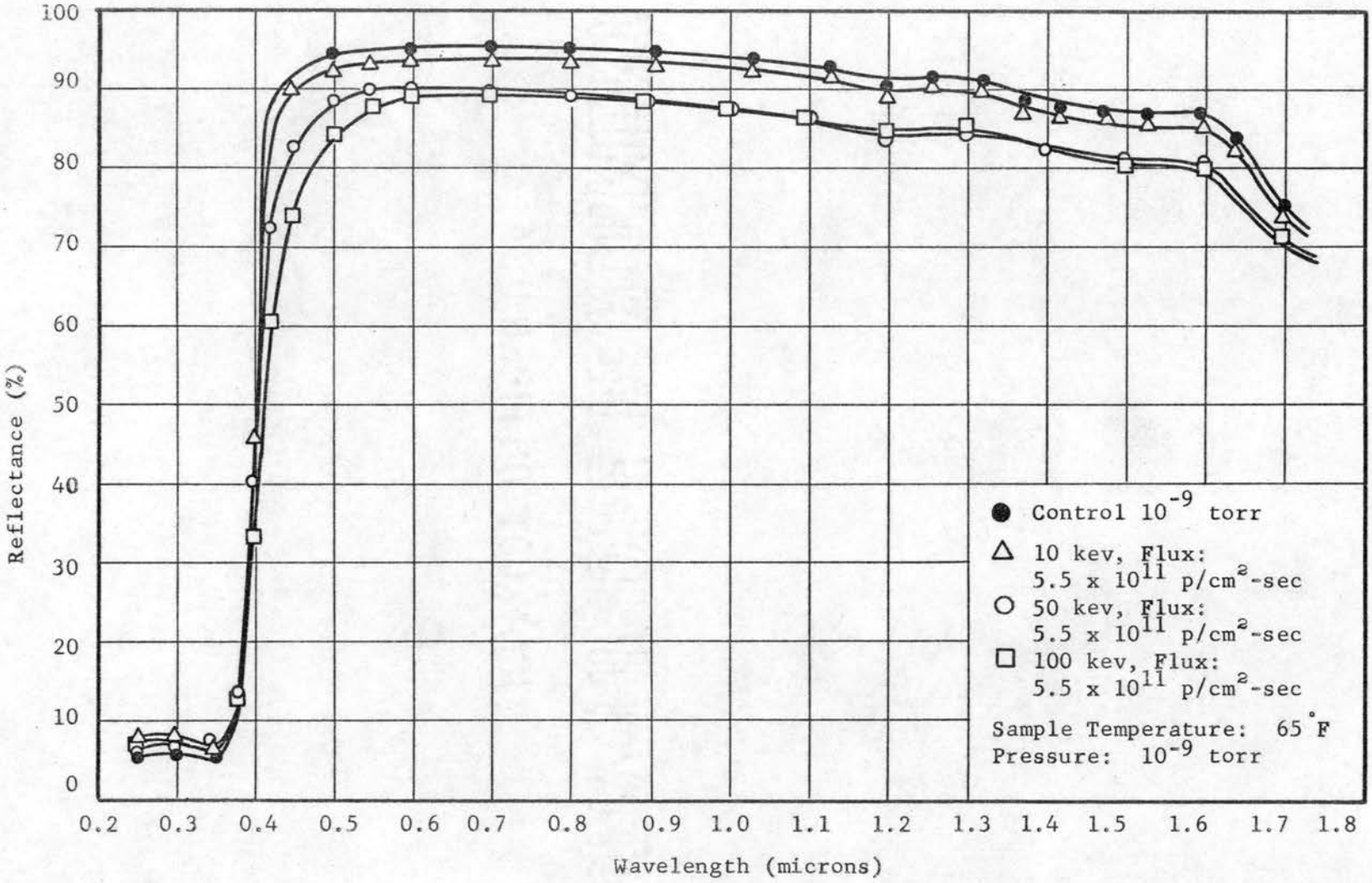


Figure 35. Optical Degradation of $TiO_2$ Coating After 10 kev, 50 kev and 100 kev Proton Irradiation at a Total Integrated Flux of $1 \times 10^{15}$ p/cm$^2$

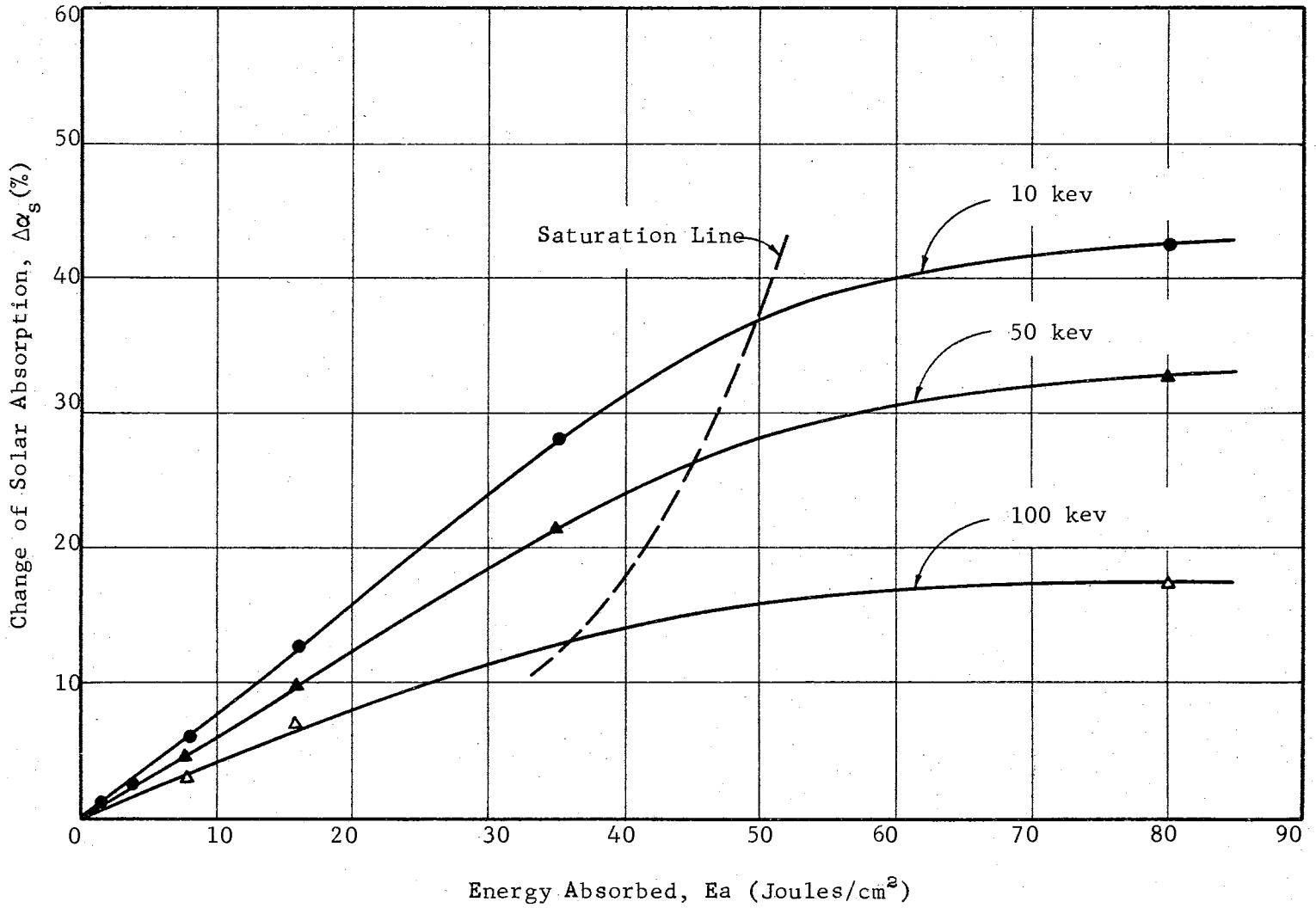


Figure 11. Optical Degradation of $TiO_2$ Coating Produced by 10 kev, 50 kev and 100 kev Proton Irradiation as a Function of Energy Absorbed

the optical degradation expressed as a change in solar absorptance is close to a linear relation for low energy absorption. Each curve reflects a saturation type relationship as a function of absorbed energy. The saturation energy for 10 kev, 50 kev and 100 kev proton irradiation is approximately 50 joules/cm$^2$, 45 joules/cm$^2$ and 35 joules/cm$^2$ respectively. Only a small increase in solar absorptance is experienced for absorbed energies greater than these values. The net changes in solar absorption as a function of absorbed energy below the saturation point and above the saturation point is as follows:

| Proton Energy (kev) | $E_a$ (Joules/cm$^2$) | $\Delta \alpha_s$ (%) |
|---|---|---|
| 10 | 0-50 | 37.0 |
| | 50-80 | 5.3 |
| 50 | 0-45 | 26.5 |
| | 45-80 | 6.3 |
| 100 | 0-50 | 13.0 |
| | 50-80 | 4.3 |

The change of solar absorptance as a function of integrated flux for 10 kev and 50 kev irradiation is depicted in Figure 37. The figure shows that a higher integrated flux of the lower energetic proton is required to cause equal optical damage of that experienced by the higher energy proton. As an example, an integrated flux of $3.3 \times 10^{16}$ p/cm$^2$ for the 10 kev proton irradiation would be required to cause the same degree of degradation ($\Delta \alpha_s = 32.8\%$) as that experienced by an integrated flux of $1 \times 10^{16}$ p/cm$^2$ for 50 kev proton irradiation.

The spectral reflectance changes as a function of energy absorbed, $E_a$, are shown in Figures 38 and 39. The main point of interest of this

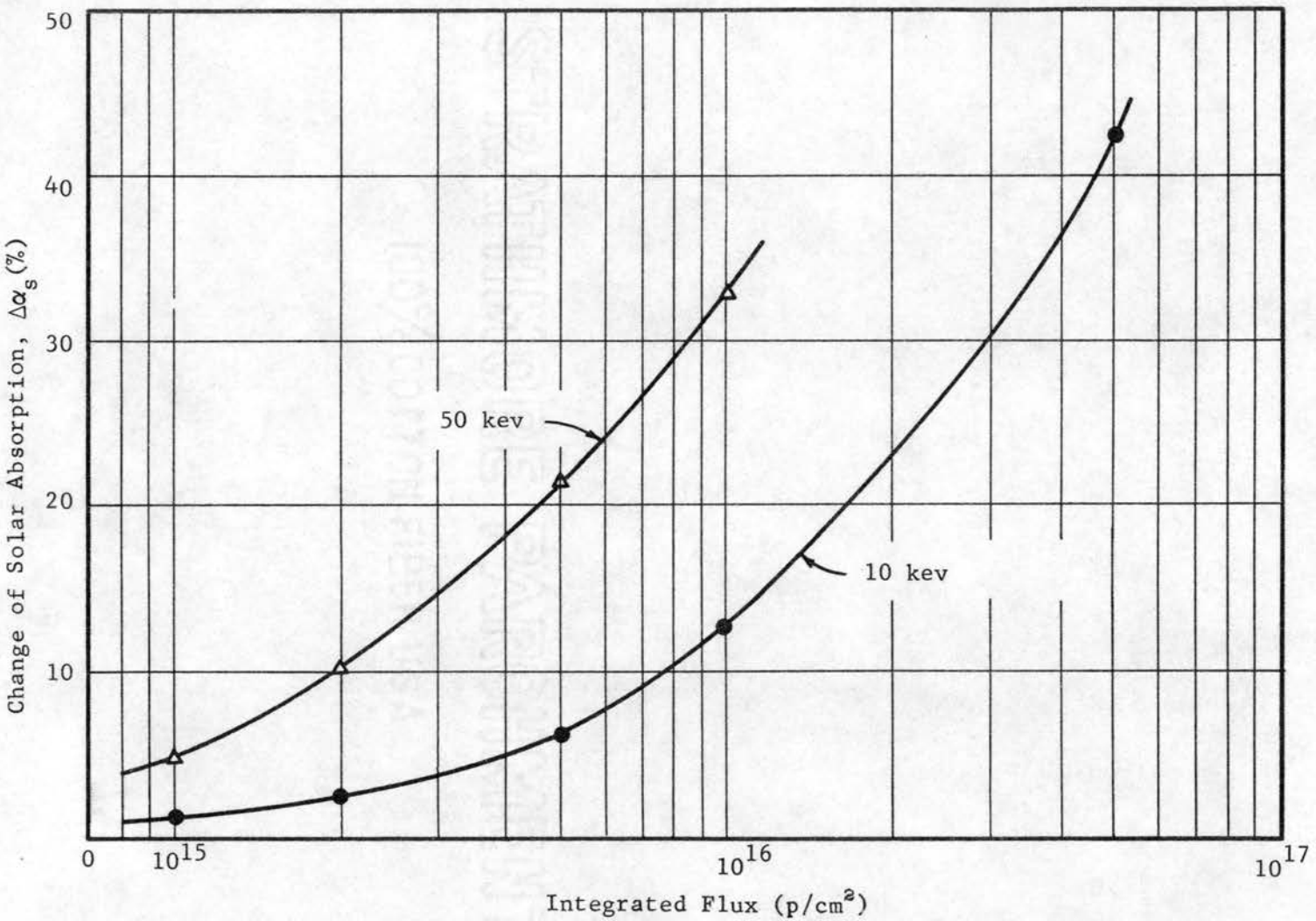


Figure 12. Change in Solar Absorptance as a Function of Integrated Fluxes for 10 kev and 50 kev Irradiation of $TiO_2$ Coating

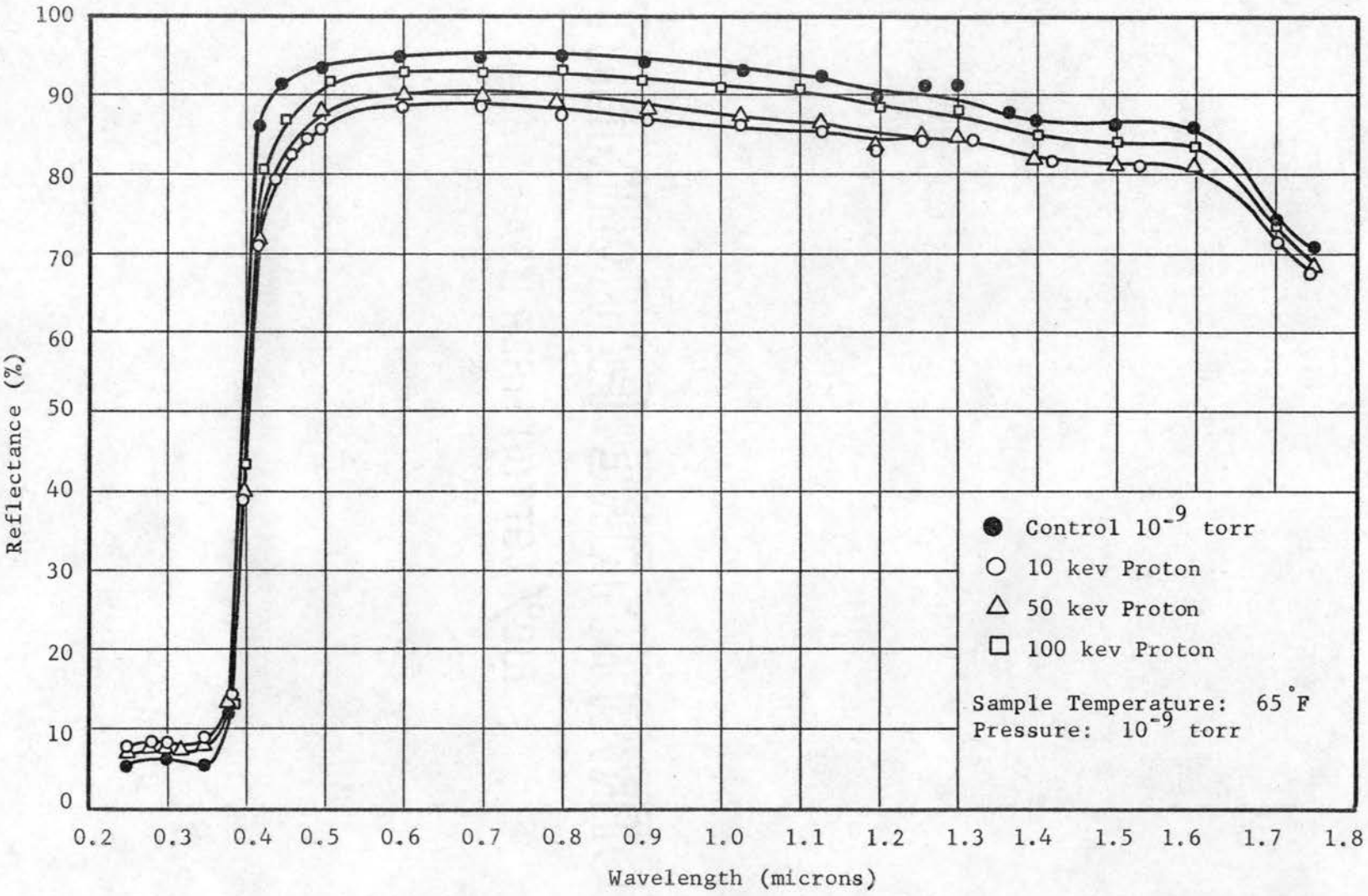


Figure 38. Optical Degradation of $TiO_2$ Coating After Irradiation with 10 kev, 50 kev and 100 kev Protons for 8 joules/$cm^2$ of Energy Absorbed

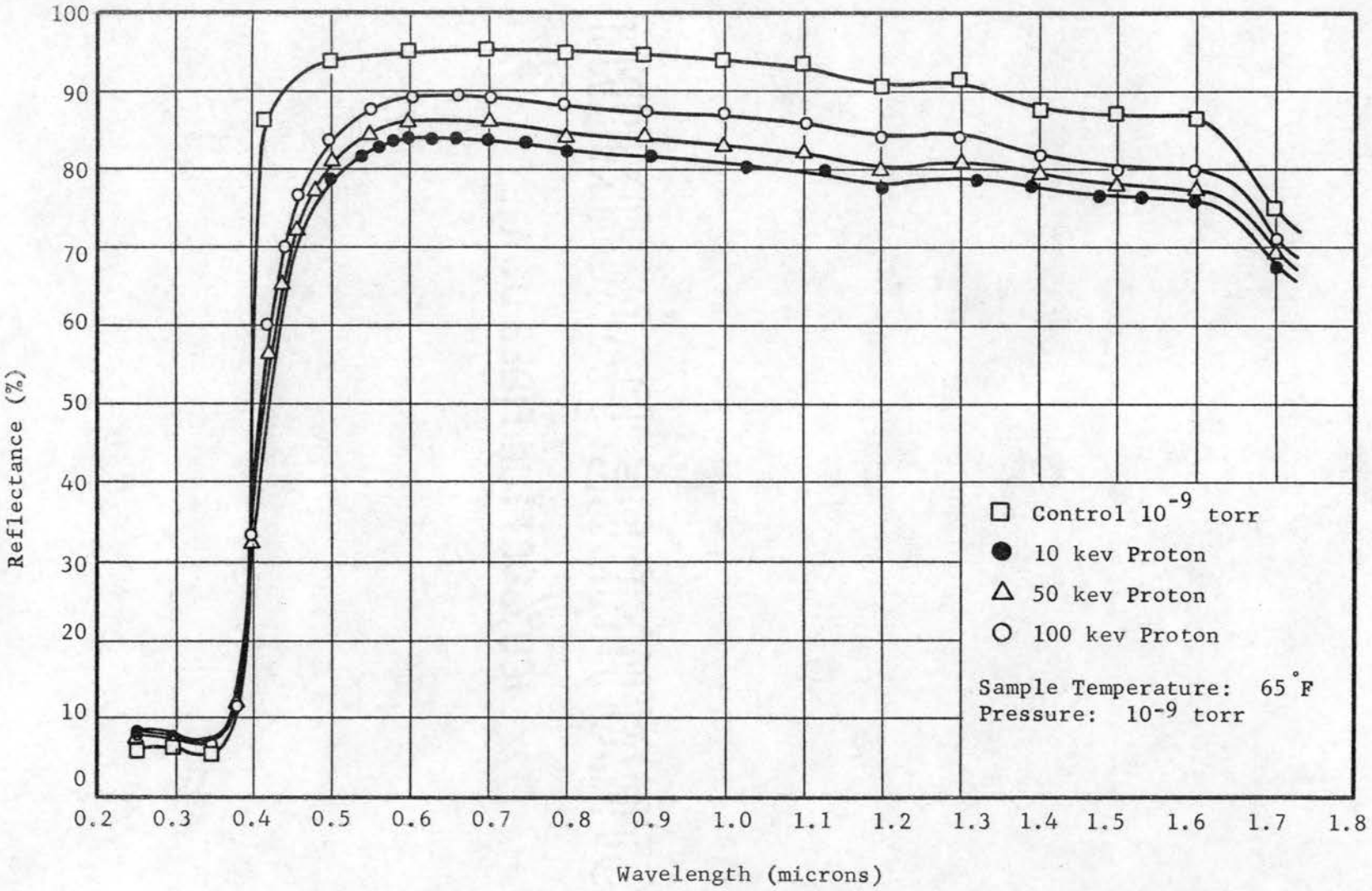


Figure 39. Spectral Reflectance Data of $TiO_2$ Coating After 10 kev, 50 kev and 100 kev Proton Irradiation for 16 joules/cm$^2$ of Energy Absorbed

data is that the low energy proton imposes a greater degradation in spectral reflectance than the higher energy proton when compared on the basis of energy absorbed in joules/$cm^2$.

Rate Effect

A series of samples (white) were tested for rate dependence. The tests were conducted at a proton energy of 100 kev and an integrated flux of $1 \times 10^{15}$ $p/cm^2$. Flux rates of $1.1 \times 10^{10}$ $p/cm^2$-sec, $5.5 \times 10^{11}$ $p/cm^2$-sec, and $1.1 \times 10^{12}$ $p/cm^2$-sec, combined with radiation times of $9.1 \times 10^4$ sec, $1.82 \times 10^4$ sec, and $9.1 \times 10^3$ sec, resulted in an integrated flux of $10^{15}$ $p/cm^2$ for each test. The following results were obtained:

Test I. Proton Energy - 100 kev
Flux - $1.1 \times 10^{10}$ $p/cm^2$-sec
Integrated Flux - $1 \times 10^{15}$ $p/cm^2$
$\alpha_s$ - 23.5%

Test II. Proton Energy - 100 kev
Flux - $5.5 \times 10^{11}$ $p/cm^2$-sec
Integrated Flux - $1 \times 10^{15}$ $p/cm^2$
$\alpha_s$ = 23.4%

Test III. Proton Energy - 100 kev
Flux - $1.1 \times 10^{12}$ $p/cm^2$-sec
Integrated Flux - $1 \times 10^{15}$ $p/cm^2$
$\alpha_s$ = 23.4%

It can be concluded from the results of these tests, along with analysis of the test data for 10 kev and 50 kev proton bombardment,

that the optical degradation of this material is independent of flux for the range of fluxes studied.

Synergestic Effects

Combined environmental simulation with protons, ultraviolet, temperature and low density was conducted on three samples of $TiO_2$ white coatings to determine the synergestic effects. Figure 40 shows the optical degradation of the three samples when irradiated with 10 kev protons and 190 equivalent sun hours (10 solar constants* of radiation for 19 hours) of ultraviolet radiation. Figures 41 and 42 show the synergestic effects of the combined environment in comparison to the proton-only and ultraviolet-only radiation degradation of the samples. The combined environmental degradation for the samples was more than the algebraic addition of the degradation effect caused by the two separate environments. For a combined environment of 10 kev protons at an integrated flux of $1 \times 10^{16}$ $p/cm^2$ and 190 hours of ultraviolet radiation the change in solar absorptance was 18.0% and the algebraic addition of the changes in solar absorptances caused by the two separate parameters, proton-only and ultraviolet-only, was 13.4%. Also, there seems to exist an annealing effect within the coating that caused less synergestic degradation in the longer wavelengths (infrared region) than that experienced in the proton-only radiation test. This is depicted by the crossover of the reflectance curves at approximately

*Solar constant is defined for this study as the flux density of extraterrestrial ultraviolet radiation in the wavelength region from 0.2 to 0.4 microns, intercepting a flat plate which is perpendicular to the solar vector at one astronomical unit from the sun.

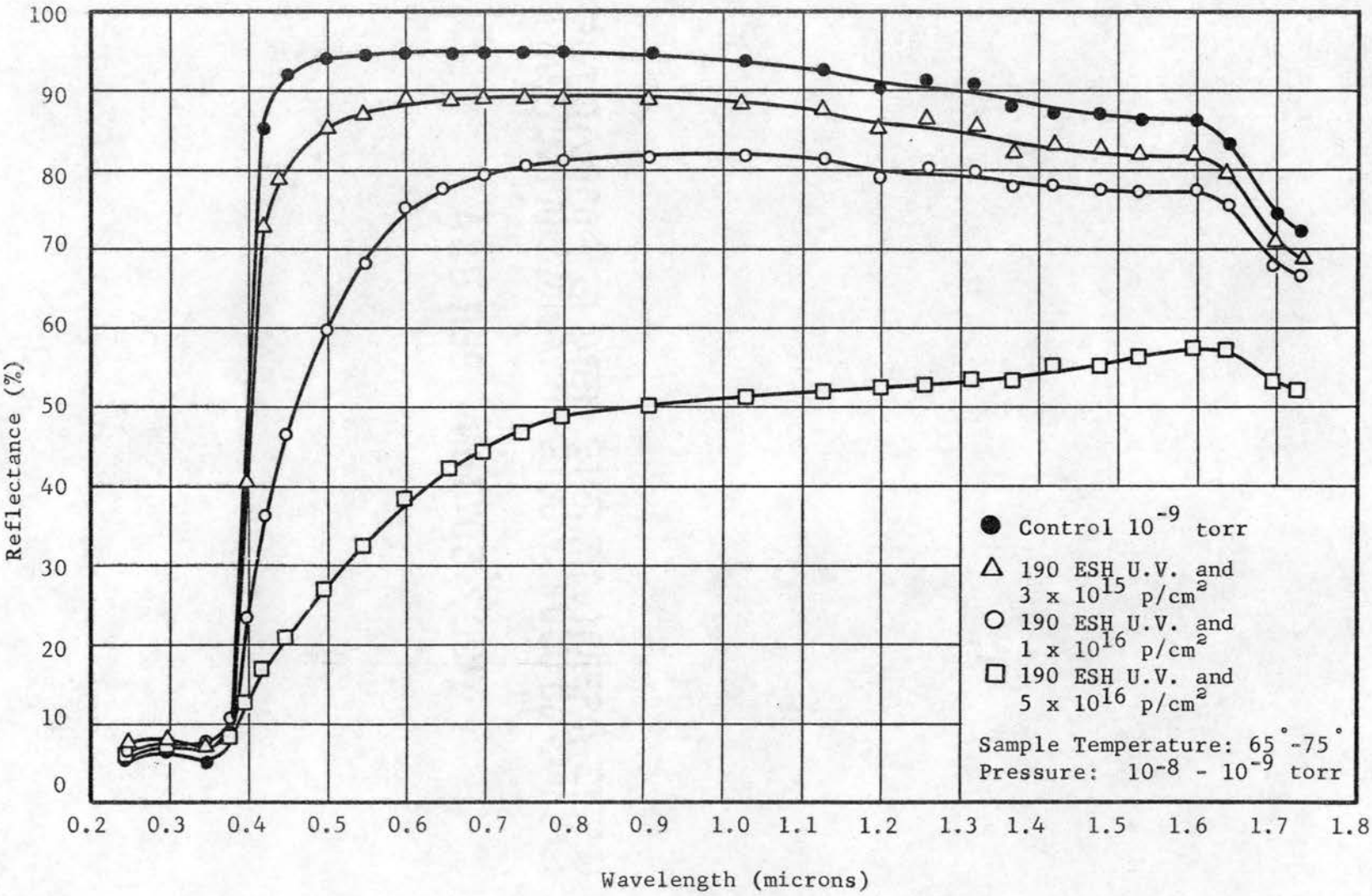


Figure 40. Optical Degradation of $TiO_2$ Coating for Combined Environment of Low Density, Ultraviolet and 10 kev Proton Irradiation

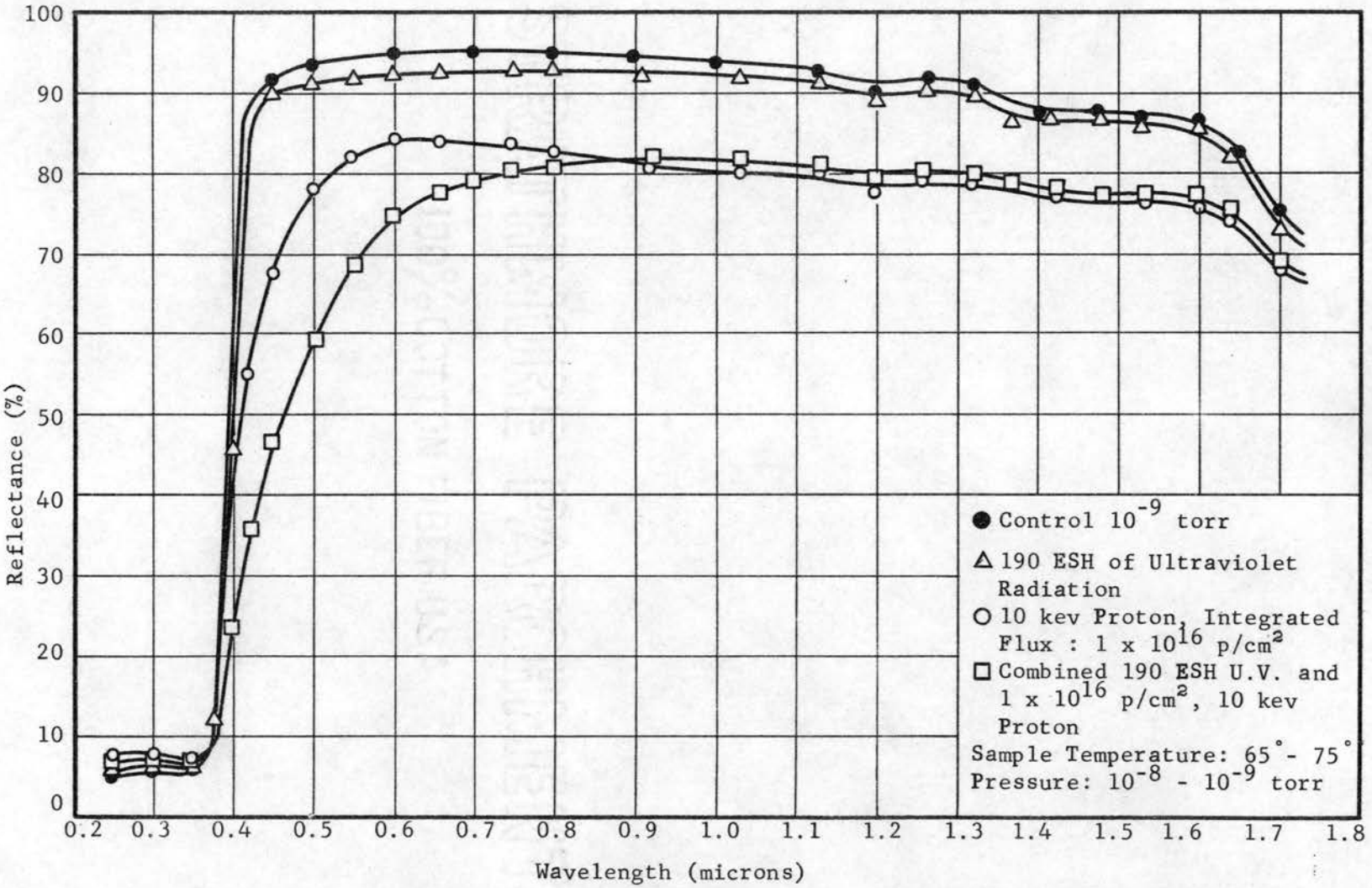


Figure 41. Optical Degradation of $TiO_2$ Coating Showing Synergistic Effects of Low Density, Ultraviolet and 10 kev Proton Irradiation for an Integrated Flux of 1 x $10^{16}$ p/cm$^2$

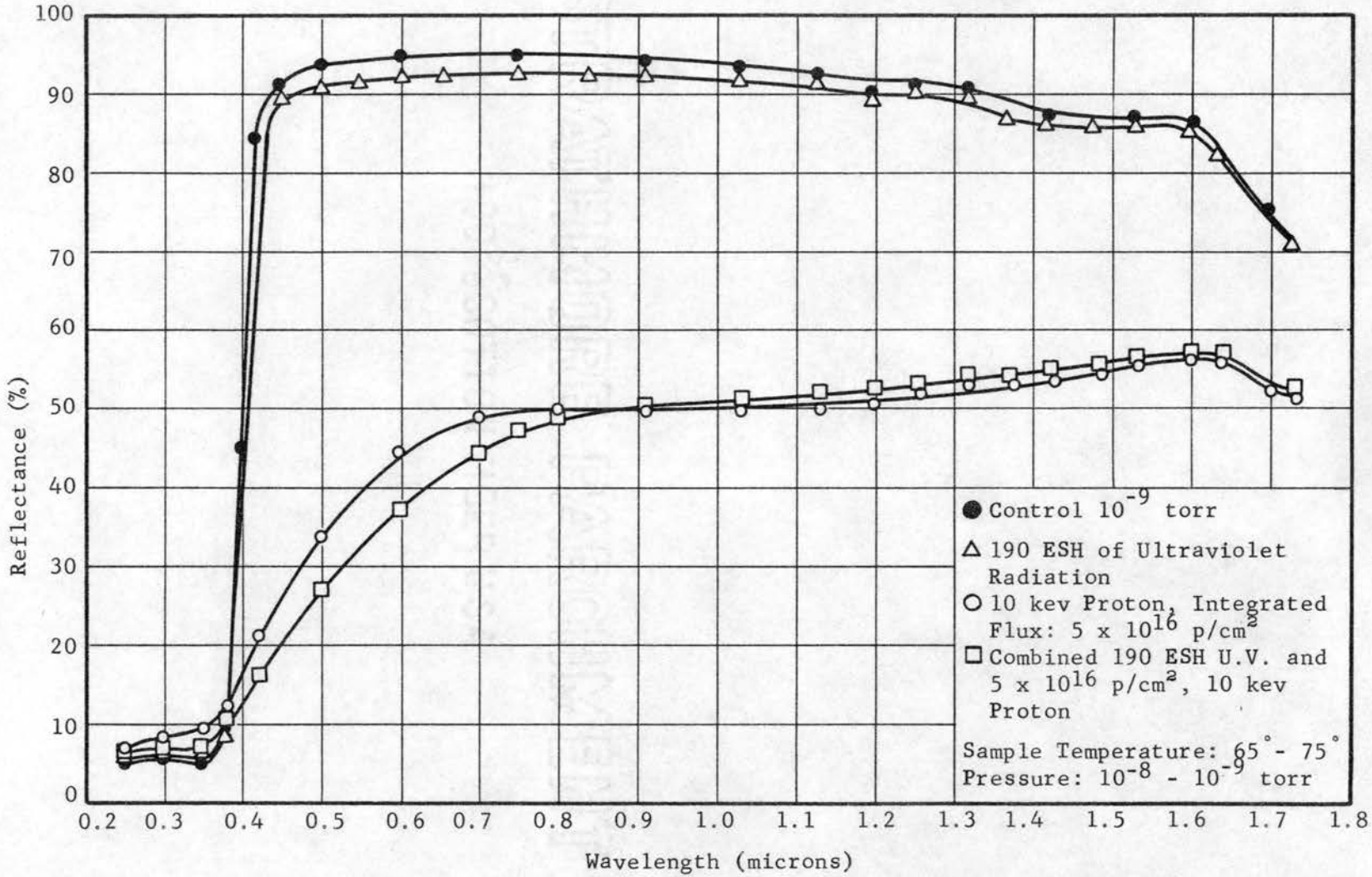


Figure 42. Optical Degradation of $TiO_2$ Coating Showing Synergistic Effects of Low Density Ultraviolet and 10 kev Proton Irradiation for an Integrated Flux of $5 \times 10^{16}$ p/cm$^2$

0.85 microns in Figure 40 and 41. Results of these tests clearly indicate the need for combined environmental testing of thermal-control materials.

Sample Temperature Relationship

A series of tests were conducted on $TiO_2$ white coating to determine the degradation as a function of temperature. Samples were irradiated with 100 kev protons at a flux of $5.5 \times 10^{11}$ p/cm$^2$ for an integrated flux of $5 \times 10^{15}$ p/cm$^2$ with sample temperatures at -300°F, 65°F, 100°F, 200°F, and 300°F. Optical degradation results of these tests are shown in Figure 43. The spectral reflectance curves show a shift in the absorption edge with increasing temperature and a greater decrease in spectral reflectance with lower temperature in the longer wavelengths. The crossover of the spectral reflectance curves occurs at approximately 0.75 microns. The over-all change in solar absorption from that of the control sample (low density only) for the various sample temperatures are as follows:

| Sample Temperature (°F) | $\Delta\alpha_s$ (%) |
|---|---|
| -300 | 15.8 |
| 65 | 17.3 |
| 100 | 19.3 |
| 200 | 20.6 |
| 300 | 23.3 |

Results of these tests indicate that degradation of thermal-control materials is a function of temperature. However, a certain degree of uncertainty exists in the values of the optical damage because the

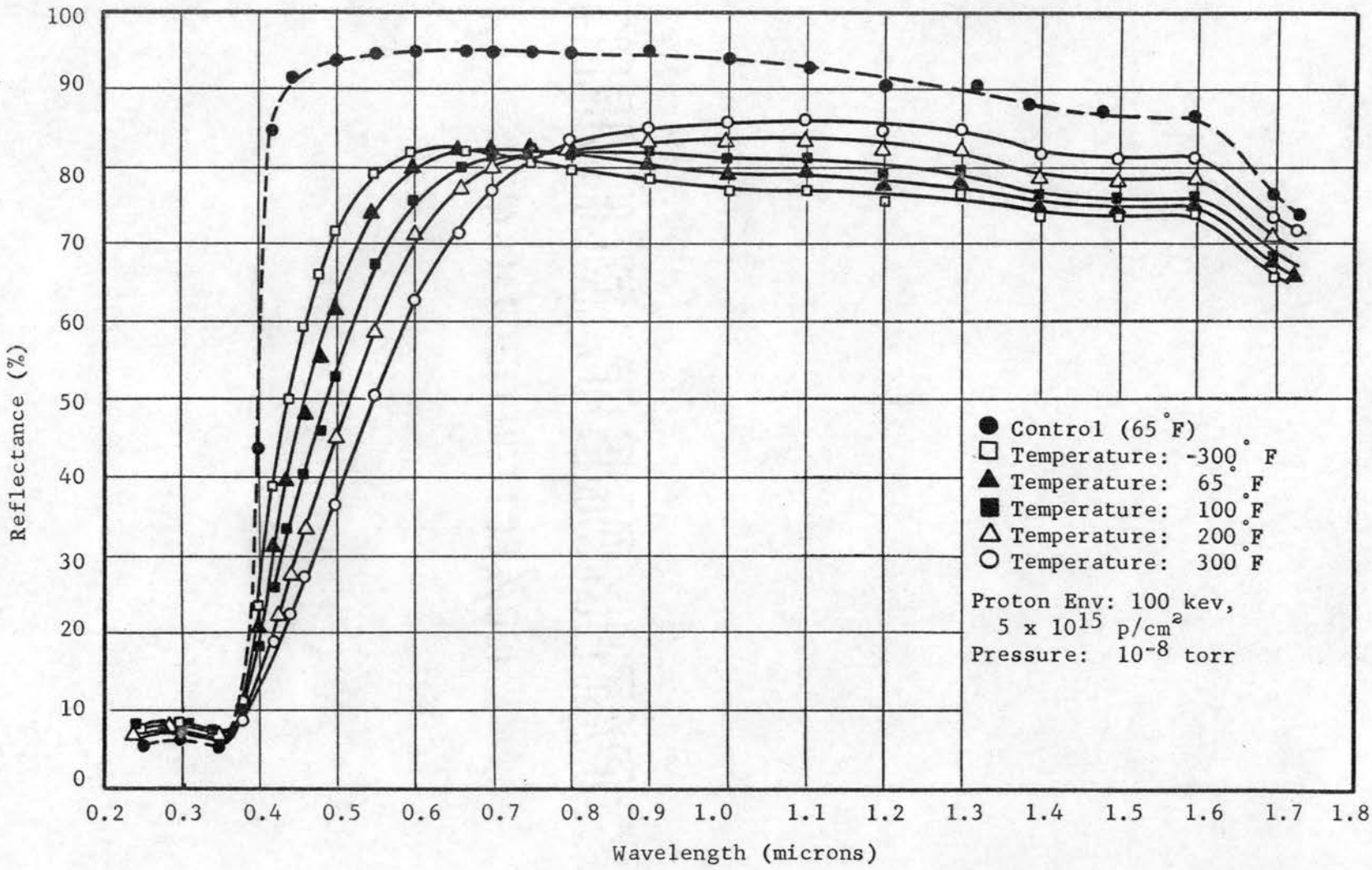


Figure 43. Optical Degradation of $TiO_2$ Coating After 100 kev Proton Irradiation As a Function of Sample Temperature

reflectance measurements of the irradiated samples were accomplished at room temperature.

Microscopic Analysis

Microscopic analysis of the proton irradiated samples was undertaken to obtain a better understanding of the surface damage as related to the optical degradation and proton irradiation of the samples. The surface appearance for $TiO_2$ coatings before and after 10 kev proton irradiation at integrated fluxes of $1 \times 10^{15}$ p/cm$^2$, $5 \times 10^{15}$ p/cm$^2$, and $1 \times 10^{16}$ p/cm$^2$ are shown in Figure 44. The nonirradiated sample shows an extremely smooth surface. The irradiated samples indicate an increase of roughness with an increase of integrated flux. Of particular interest is the noticeable increase in the seemingly damaged area for the samples as the total proton exposure increases. Also, the higher the integrated flux, the greater the roughness and larger the cracks in the surface. Microscopic surface texture as a function of proton energy is shown in Figure 45. The irradiated samples indicate a surface damaging effect related to proton energy. The higher the proton energy the larger and deeper the cracks in the coating and greater is the change in absorptance. This phenomena can be better observed in the microscopic cross-sectional photomicrographs of the irradiated samples presented in Figure 46. The proton irradiated samples show a very distinct roughness in the exposed surface with no apparent microscopic roughness in the unexposed sample. The degradation depth of the 10 kev proton irradiated sample appears to be limited to a very narrow region close to the surface. The higher energy proton irradiation shows a correlation of degradation depth and

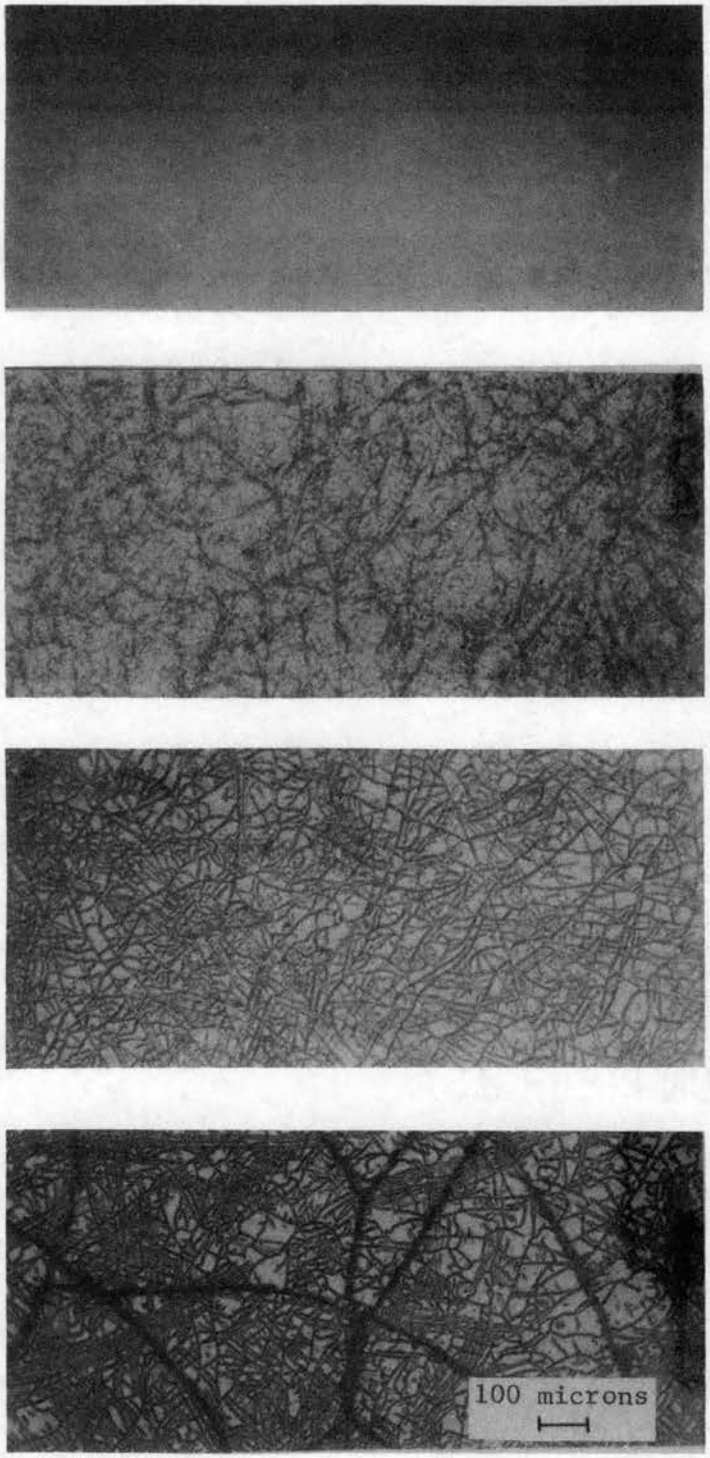


Nonradiated Sample

Integrated Flux: $1 \times 10^{15}$ p/cm$^2$
$\Delta\alpha_s = 1.1\%$

Integrated Flux: $5 \times 10^{15}$ p/cm$^2$
$\Delta\alpha_s = 6.1\%$

Integrated Flux: $1 \times 10^{16}$ p/cm$^2$
$\Delta\alpha_s = 18.0\%$

**Figure 44. Photomicrographs of $TiO_2$ Coating After 10 kev Irradiation**

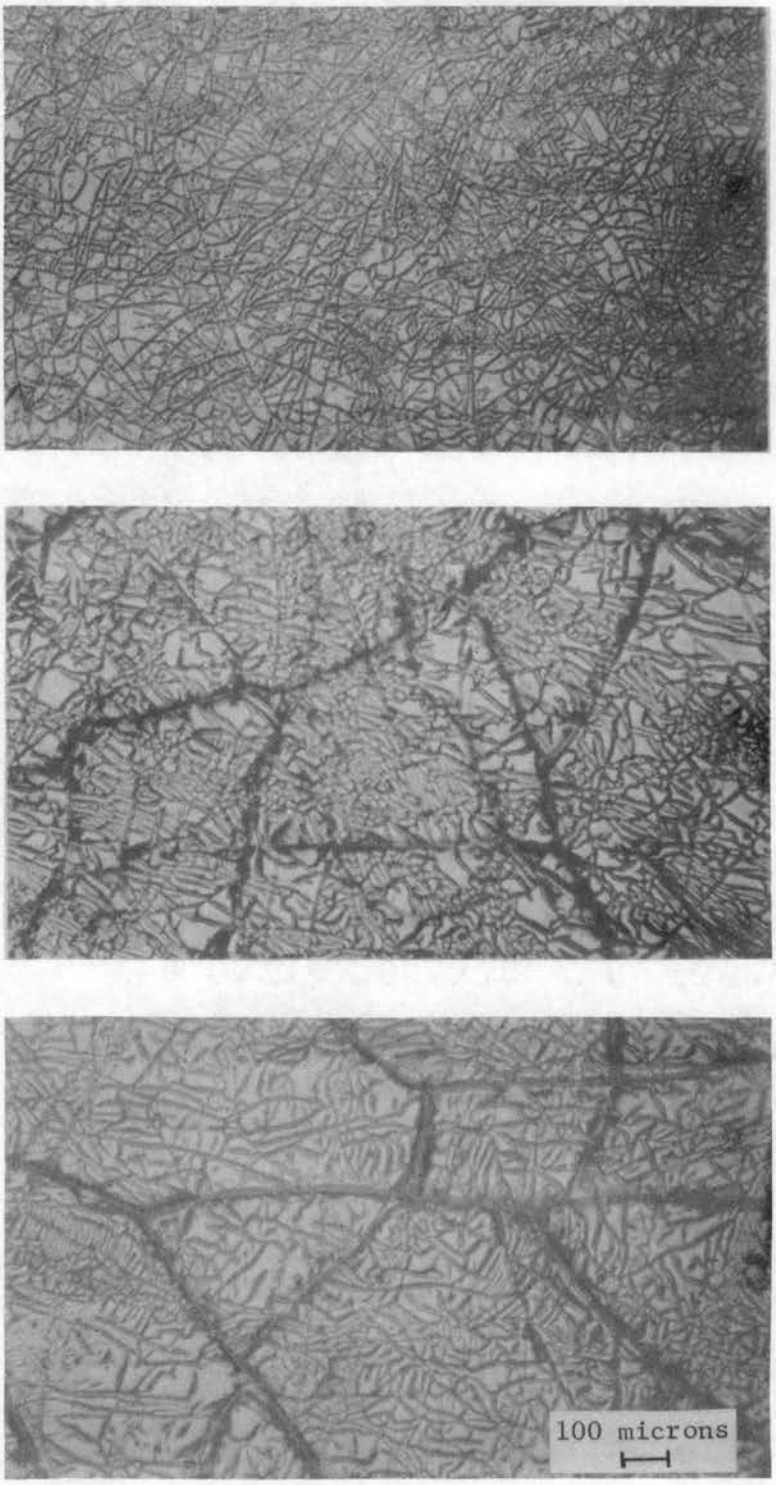


Figure 45. Photomicrographs of $TiO_2$ Coating After 10 kev, 50 kev and 100 kev Irradiation For an Integrated Flux of $5 \times 10^{15}$ p/cm$^2$

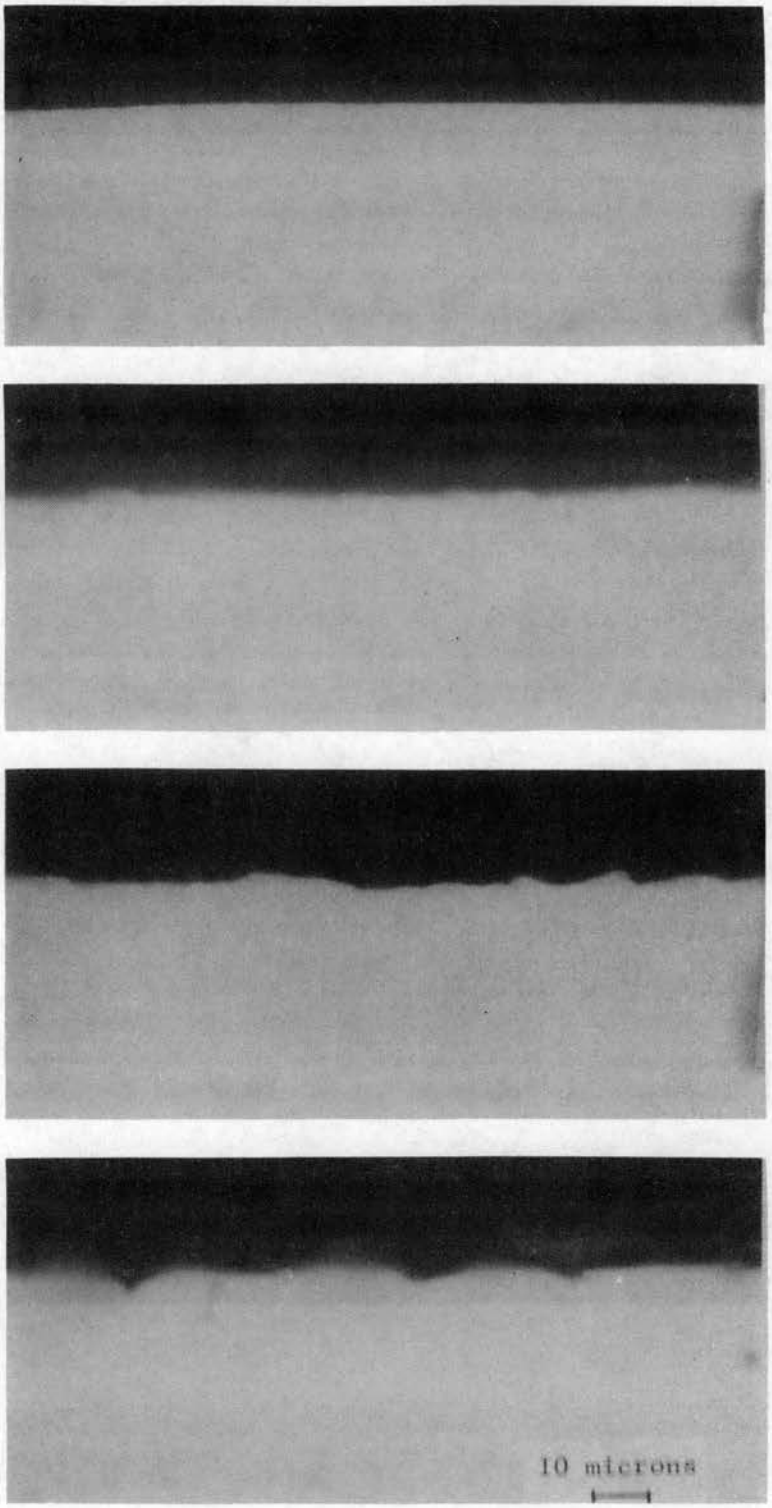


Figure 46. Cross Section Analysis of $TiO_2$ Coating After 10 kev, 50 kev, and 100 kev Proton Irradiation

the calculated penetration ranges (Table XIV). It appears that the change in solar absorptance is related to the depth of the damage layer and therefore to the penetration range of the proton.

The penetration ranges for $TiO_2$ were calculated from the data presented in Table IX of Chapter VI. The average weight of the $TiO_2$ samples was 0.1066 grams and the exposed area of samples was 4.45 $cm^2$. Using this information and the data from Table IX the calculated penetration range as a function of proton energy is presented in Table XIV.

TABLE XIV

CALCULATED PROTON PENETRATION RANGE OF $TiO_2$ COATING

| Proton Energy (kev) | Penetration Range (Microns) |
|---|---|
| 10 | 0.067 |
| 50 | 0.335 |
| 100 | 0.871 |
| 500 | 7.583 |
| 600 | 9.908 |

From the analysis of the photomicrographs, the optical degradation is a function of the surface roughness which is directly related to the proton energy. The damage mechanism could be due to a sputtering process and the chemical reaction associated with the bombarding hydrogen ions reacting with certain elements in the thermal-control material.

Bleaching

The ultraviolet-only irradiated samples showed a bleaching and/or annealing effect when exposed to the atmospheric environment for a period of time. Reflectance measurements for all samples were accomplished immediately after their removal from the space simulator to partially eliminate this phenomena. In selected samples the light yellow color caused by the ultraviolet irradiation of the white coatings had completely disappeared after a 12-hour period of atmospheric exposure. To curtail this bleaching effect, the reflectance measurements of the ultraviolet-only irradiated samples were conducted in an inert atmosphere. Figure 47 shows the spectral reflectance of $TiO_2$ white coating after 560 equivalent solar sun hours of irradiation. The figure also depicts the degradation recovery after 2 and 12 hours of atmospheric exposure.

The reflectance measurements conducted in an inert atmosphere showed an optical degradation in solar absorptance of 6.5% ($\Delta\alpha_s = 6.5\%$). After two hours of atmospheric exposure the degradation had decreased to $\Delta\alpha_s = 2.9\%$, which was a 55 per cent recovery in the total degradation measured in the inert atmosphere. After 12 hours of atmosphere exposure the degradation had decreased to $\Delta\alpha_s = 1.9\%$.

The atmospheric bleaching or annealing phenomena was less pronounced for the combined proton and ultraviolet irradiation and was not detectable with the proton-only irradiated samples.

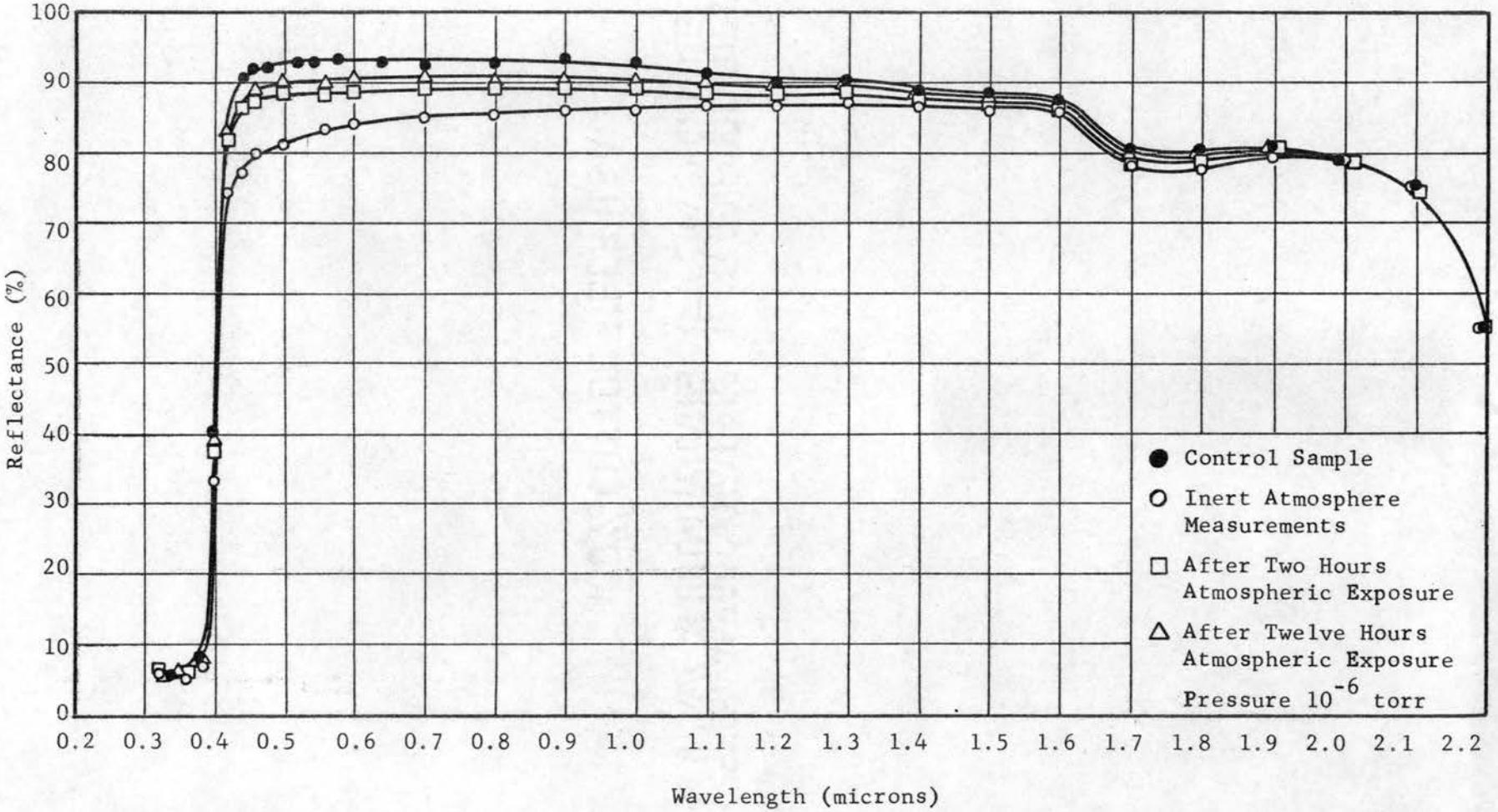


Figure 47. Optical Degradation of $TiO_2$ White Coating After 560 ESH of Ultraviolet Irradiation For Various Periods of Atmospheric Exposure

# CHAPTER X

## CONCLUSION AND RECOMMENDATIONS

The basic objective of this study has been achieved by limiting the testing program to mostly that of $TiO_2$ white thermal-control material and the particle radiation to protons. Results of the study indicate that this type of thermal-control material is susceptible to absorptance degradation by simulation of the low density, temperature, proton radiation and electromagnetic radiation of the space environment. The damaging mechanism is associated with decomposition, evaporation, chemical reaction and physical sputtering of the material.

Results of the investigation can be summarized as follows:

1. Synergestic effects of engineering significance are produced when the material is exposed to the combined environment. The combined environmental degradation for the material is more than the algebraic addition of the degradation caused by the individual environmental parameters. Combined environmental testing of thermal-control materials is necessary for proper evaluation of degradation.

2. The degree of optical damage is largely independent of the proton flux. Results of accelerated flux testing may be utilized to predict degradation of materials for lower fluxes.

3. Optical degradation of thermal-control materials is a function of proton energy. The more energetic particle produces a proportionately

2. The degree of optical damage is largely independent of the proton flux. Results of accelerated flux testing may be utilized to predict degradation of materials for lower fluxes.

3. Optical degradation of thermal-control materials is a function of proton energy. The more energetic particle produces a proportionately greater damage. For over-all evaluation of the expected space environmental degradation it is important to consider not only the integrated fluxes of the proton environment but also their individual energies.

4. Degradation is a function of temperature; the higher the temperature, the greater the optical degradation. For simulation testing of thermal-control materials, temperature control of the sample is necessary for proper evaluation of degradation.

5. Atmospheric bleaching and annealing effect is very pronounced for the ultraviolet irradiated materials.

6. Initially, materials degrade very rapidly when subjected to a radiation-type environment and then appear to reach a saturation point.

7. Detailed calibration of spectrometer equipment is required for absolute measurement of spectral reflectance.

In summary, the results of this study have clearly indicated the need for combined environmental testing of thermal-control materials and the requirement for in situ-type measurements for the proper evaluation of optical degradation of thermal-control materials. In order to explain the basic causes of degradation it is necessary to understand the mechanism of radiation interaction with the material and the basic properties of the material that control the degradation process.

The following recommendations are submitted for consideration:

1. Similar tests, including electron irradiation, should be conducted on other space materials.

2. The $TiO_2$ coating should be subjected to electron particle irradiation to establish the dependence of optical damage on particle energy, flux, and integrated flux and to determine the synergistic effects associated with electron-type combined environmental testing.

3. Accelerated ultraviolet testing should be investigated for the purpose of determining the rate effect.

4. In situ reflectance measurement techniques should be developed for the purpose of determining the optical degradation of the sample under a low density environment at the sample test temperature.

5. Standard techniques should be established for the calibration of spectrometers used in the measurement of optical degradation of thermal-control materials.

6. Published results of degradation studies should include the degree of simulation for all parameters and the methods and techniques used in simulating and measuring the parameters. This data is necessary in order to correlate all the published data related to a particular material.

## A SELECTED BIBLIOGRAPHY


1. Hoss, G., Drummeter, L. F., Jr., and Schach. "Temperature Stabilization of Highly-Reflecting Spherical Satellites." Journal of the Optical Society of America, Vol. 49, 1959, pp. 918-924.

2. Heller, G. "Thermal Control of the Explorer Satellites." Journal of American Rocket Society, Vol. 30, 1960, pp. 344-352.

3. Camack, W. G., and Edwards, D. K. "Effect of Surface Thermal-Radiation Characteristics on the Temperature Control Problem in Satellites." Surface Effects on Spacecraft Materials. Edited by F. J. Clauss, New York: Wiley and Sons, 1960, pp. 55-88.

4. Johnson, F. S. "The Solar Constant." J. Meteor, Vol. II.

5. Johnson, F. X., Malitson, H. H., Purcell, J. D., and Tousey, R. "Emission Lines in the Extreme Ultraviolet Spectrum of the Sun." Journal of Applied Physics, Vol. 127, 1958.

6. Johnson, F. S., Purcell, J. D., Toussey, R., and Wilson, N. "The Ultraviolet Spectrum and the Sun." Rocket Exploration of the Upper Atmosphere. Edited by Boyd and Seaton, London: Permagon Press, 1954.

7. Byram, E. T., Chubb, T., and Friedman. "The Study of Extreme Ultraviolet Radiation from the Sun with Rocketborne Photon Counters." Rocket Exploration of the Upper Atmosphere. Edited by Boyd and Seaton, London: Permagon Press, 1954.

8. Camack, W. G. "Albedo and Earth Radiation." Space Materials Handbook. Chapter 6. Edited by Goetzel, Rittenhouse and Singletary, ML-TDR-64-40, January 1965.

9. Hanson, W. B. "Structure of the Ionosphere." Satellite Environment Handbook. Edited by Johnson, F. S., Standard Press, 1961.

10. Andrew, A., Crowther, D. L., Harless, W. H., Jr., Newell, D. M., and Gomez, M. "Penetrating Radiation." Space Materials Handbook. Chapter 7. Edited by Goefzel, Rittenhouse and Singletary, ML-TDR-64-50, January 1965.

11. Freden, S. C., and White, R. S. "Particle Fluxes in the Inner Radiation Belt." Journal of Geophysical Research, Vol. 65, No. 5, May 1960.

12. Ruthwell, P., and McIlwain, C. E. "Magnetic Storms and the Van Allen Radiation Belts." Journal of Geophysical Research. Vol. 65, No. 3, March 1960, p. 799.

13. Scarsi, L. "Cosmic Radiation." American Journal of Physics, Vol. 28, No. 3, Marhc 1960, p. 213.

14. Gold, T. "Cosmic Rays and Interplanetary Medium." Astronautics, Vol. 7, No. 8, August 1962, p. 43.

15. Lockwood, J. A. "Decrease of Cosmic Ray Intensity." Journal of Geophysical Research, Vol. 65, No. 1, January 1960, p. 27.

16. Winckler, J. R. "Observations of Low-Energy Cosmic Rays from the Flare of 22 August 1958." Journal of Geophysical Research, Vol. 64, 1959, p. 1133.

17. Roberts, W. T. "Space Radiations; A Compilation and Detail Discussion." NASA Technical Documentary Report, No. TMX-5470, January 1964.

18. McDonald, Frank B. "Solar Proton Manual." NASA Technical Documentary Report, No. SP-50, December 1963.

19. Bailey, D. K. "Time Variations of the Energy Spectrum of Solar Cosmic Rays in Relation to the Radiation Hazard in Space." Journal of Geophysical Research, Vol. 67, 1962, pp. 391-396.

20. Madey, R. "Shielding Against Space Radiation." Nucleonics, May 1963.

21. Evans, R. D. The Atomic Nucleus. New York: McGraw-Hill Book Co., Inc., 1955.

22. Linus, P. The Nature of the Chemical Bond. 2nd Edition, Cornell University Press, 1960.

23. Kircher, J. F., and Bowman, R. E. Effects of Radiation on Materials and Components. New York: Reinhold Publishing Corp., 1964.

24. Burrill, E. A. "Simulating Space Radiation." Space/Aeronautics, Vol. 41, No. 5, May 1964.

25. Gilligan, J. E., and Caren, R. P. "Some Fundamental Aspects of Nuclear Radiation Effects in Spacecraft Thermal-Control Materials." Presented at the Symposium on Thermal Radiation of Solids, March 1964.

26. Pezdirtz, G. F. and Jewell, R. A. "A Study of the Photo-Degradation of Selected Thermal-Control Surface." Presented at the Fifth Symposium on Thermal Radiation of Solids, March 1964.

27. Zerlaut, G. A., and Kaye, B. H. "Development of Space-Stable Thermal-Control Coatings." IITRI-C6014-4, 8, 13, 18, 21, NASA Contract No. NAS8-5379, 1964-65.

28. Zerlaut, G. A., and Harada, Y. "Stable White Coatings." IITRI-C207-25, Contract No. 95001 for Jet Propulsion Laboratory, August 1963.

29. Zerlaut, G. A., Harada, Y., and Baldridge, J. H. "Stable White Coatings." IITRI-C6027-7, Semiannual Report to Jet Propulsion Laboratory Contract No. 950746, August 1964.

30. Zerlaut, G. A., Harada, Y., and Tompkins, E. H. "Ultraviolet Irradiation in Vacuum of White Spacecraft Coatings." Symposium on Thermal Radiation of Solids, March 1964.

31. Plunkett, J. D. "NASA Contributions to the Technology of Inorganic Coatings." NASA SP-5014, November 1964.

32. Miller, R. A., and Campbell, F. J. "Effects of Low-Energy Protons on Thermal Coatings." AIAA Thermophysics Specialist Conference, September 1965.

33. Gillette, R. B., Brown, R. R., Seiler, R. F., and Sheldon, W. R. "Effects of Protons and Alpha Particles on Thermal Properties of Spacecraft and Solar Concentrator Coatings." Presented at AIAA Thermophysics Specialist Conference, September 1965.

34. Jorgenson, G. V. "Effects of Simulated Solar-Wind Bombardment Spacecraft Thermal-Control Surfaces." Presented at AIAA Thermophysics Specialist Conference, September 1965.

35. Breuch, R. A., Douglas, N. J., and Vance, D. "The Effects of Electron Bombardment on the Optical Properties of Spacecraft Temperature Control Coatings." Presented at Second AIAA Aerospace Sciences Meeting, January 1965.

36. Clauss, F. J., Mauri, R. E., Smith, E. C., and Drake, S. "Evaluating the Behavior of Materials Under Space Conditions." Lockheed Aircraft Corp., Missiles and Space Division, Sunnyvale, Calif.

37. Pinson, J. D., Schmidheiser, C. A., and Zumwalt, G. W. "Space Environment Effects on Materials: A State-of-the-Art Survey." AEDC Technical Documentary Report, December 1965.

38. Roberts, R. W., and Vanderslice, T. A. Ultrahigh Vacuum and Its Applications. New Jersey: Prentice-Hall, 1963.

39. Dusham, S. Vacuum Technique. New York: John Wiley and Sons, 1955.

40. Ham, J. L. "Mechanisms of Surface Removal from Metals in Space." Aerospace Engineering, Vol. 20, No. 5, May 1961.

41. Jaffe, L. D., and Rittenhouse, J. B. "Behavior of Materials in Space Environments." Jet Propulsion Laboratory Technical Report, No. 32-150, November 1961.

42. Obert, E. F. Concepts of Thermodynamics. New York: McGraw-Hill Book Co., Inc., 1960.

43. Redmond, R. F. "Space Radiation and its Effects on Materials." Battelle Memorial Institute, AD 261277, June 1961.

44. Roberts, R. W. "An Outline of Vacuum Technology." General Electric Research Laboratory Report, No. 64-RL-3394 C, September 1964.

45. Seitz, F., and Koehler, J. S. Solid State Physics. New York: Academic Press, 1956, Vol. 2, pp. 207-448.

46. Baker, C. J., and Segre, E. Physics Review. 811, 489, 1951.

47. Lapp, R. E., and Andrews, H. L. Nuclear Radiation Physics. Englewood Cliffs, New Jersey: Prentice-Hall, Inc., 1963.

48. Bethe, H. A., and Ashkin, J. A. Experimental Nuclear Physics. 1954.

49. Linnenbom, V. J. "Range-Energy Relations for Protons and Electrons in Al, Si, and $SiO_2$." NRL Report, 5828, September 1962.

50. Allison, S. K., and Warshaw, S. D. "Passage of Heavy Particles Through Matter." Reviews of Modern Physics, Vol. 25, October 1953.

51. Redus, J. R. "Sputtering of a Vehicle's Surface in a Space Environment." NASA TN D-1113, June 1962.

52. Baden, M., Witteborn, F. C., and Snouse, T. W. "Sputtering of Metals by Mass-Analyzed $N_2^+$ and $N^+$, NASA TR R-105, 1961.

53. Jacque, J. A., and Kuppenheim, H. F. "Theory of the Integrating Sphere." Journal of the Optical Society of America, Vol. 45, 1954, pp. 460.

54. Edwards, D. K., Gier, J. T., Nelson, K. E., and Roddick, R. D. "Integrating Sphere for Imperfectly Diffuse Samples." Journal of the Optical Society of America, Vol. 51, 1960, pp. 1279.

55. Tellex, P. A., and Waldron. "Reflectance of Magnesium Oxide." Journal of the Optical Society of America, Vol. 45, 1955, pp. 19.

56. McKinney, D. S., and Friedel, R. A. "A Calibration Method for Infra-Red Prism Spectrometers." Journal of the Optical Society of America, Vol. 38, March 1948, pp. 222.

57. _____. International Critical Tables of Numerical Data. New York: McGraw-Hill Book Co., Inc., 1929, Vol. VI.

58. _____. Instruction Manual for Infrared Equipment, Norwalk, Conn.: The Perkin-Elmer Corp., Vol. 3A.

59. Streiff, M. L., and Ferriso, C. C. "Spectral Slit Width of a Small Prism Monochromator." General Dynamics Astronautics, GDA-DBE64-054, August 1964.

60. Strong, John. Concepts of Classical Optics. W. H. Freeman and Co., 1958.

61. _____. "Proposed Recommended Practices for Preparation of Reference White Reflectance Standards." Prepared by American Society for Testing and Materials Committee, E-12, March 1965.

62. Middleton, W. E., and Sanders, C. L. "The Absolute Spectral Diffuse Reflectance of Magnesium Oxide." Journal of the Optical Society of America, Vol. 41, June 1951, pp. 419.

VITA

Jay D. Pinson

Candidate for the Degree of

Doctor of Philosophy

Thesis: SYNERGISTIC AND ACCELERATED TESTING EFFECTS ON SPACE THERMAL-CONTROL MATERIALS

Major Field: Mechanical Engineering

Biographical:

Personal Data: Born near Portsmouth, Ohio, June 23, 1929, the son of Earnest and Hester Pinson.

Education: Received the Bachelor of Science Degree in Mechanical Engineering from Ohio University, Athens, Ohio in 1950; received the Master of Science Degree in Mechanical Engineering from Oklahoma State University, Stillwater, Oklahoma in 1965; completed requirements for the Doctor of Philosophy Degree at Oklahoma State University in May, 1966.

Professional Experience: Presently a Major in the United States Air Force; prior to entering the USAF was employed as a research engineer for Reynolds Metals Company; served in the science and engineering field of the USAF; prior to returning to graduate school was assigned to Arnold Engineering Development Center, USAF, and conducted research studies related to space environments and simulation techniques; authored and/or coauthored several publications related to space technology; most recent publications: "Space Environment Effects on Materials: A State-of-the-Art Survey," (coauthored); AEDC Technical Documentary Report, December, 1965.

Professional Organizations: Served on the Advisory Group for Aeronautical Research and Developments (AGARD-NATO); served as Vice Chairman of the American Society for Testing and Materials Committee on Space Simulation, Committee E-21; registered professional engineer in the State of Ohio; member of the American Society for Testing and Materials, American Institute of Aeronautics and Astronautics and American Military Engineers.